`

An Integrated Compensation System Based on Empirical Mode Decomposition for Robust Non-invasive Blood Pressure Estimation

By
Huthaifa N. Abderahman

Thesis submitted to the
Faculty of Graduate and Postdoctoral Studies in partial fulfillment of the requirements
for the Ph.D. degree in
Electrical and Computer Engineering
School of Electrical Engineering and Computer Science
Faculty of Engineering
University of Ottawa

`

ABSTRACT

When it comes to monitoring human health, accuracy is not a choice. Accuracy in blood pressure (BP) estimation is essential for proper diagnosis and management of hypertension. An error of 5 mmHg is so serious, it can be responsible for doubling or halving number of patients diagnosed with hypertension. Motion artifacts are external sources of inaccuracy and can be due to sudden arm motion, muscle tremor, shivering, and transport vehicle vibration. Medium term drift, due to changing environmental factors, such as ambient temperature, can also contribute to the inaccuracy. Long term drift (ageing), can reach 9 mmHg during the first three months of usage.

In this thesis, a new stage is added to current cuff based BP devices. This stage is responsible for adjusting the pressure reading before displaying it to end users. The proposed stage is provided with a 3-axis accelerometer, which makes the detection of motion artifacts during measurement possible. Moreover, it monitors changes in the ambient temperature and sensor ageing, so that it will adaptively compensate for these inaccuracies. These sources of inaccuracy are suppressed using algorithms based on Empirical Mode Decomposition (EMD), which has the feature of removing unwanted noise components little effect on the phase or the frequency distribution of the measured signal.

With motion artifacts, measurements show that the proposed algorithms considerably improved the accuracy of the blood pressure estimates in comparison with the commonly-used conventional oscillometric algorithm that does not include a stage for artifact suppression, and allowed the estimates to consistent with the international ANSI/AAMI/ISO standard. Moreover, simulations based on experimental results show that the system is able to compensate for drift due to temperature changes and ageing with excellent performance. Results show promise towards building a robust BP monitor, with very low errors due to motion artifacts, environmental changes, and ageing.

`

ACKNOWLEDGEMENTS

I would like to express my special appreciation and thanks to my advisor Prof. Hilmi R. Dajani. You have been a great mentor and support for me. I would like to thank you for believing in my ideas, encouraging my research and for allowing me to grow as a research scientist. Thanks for all the time you gave me, all the discussions we had and the patience you showed. I am happy I had this opportunity to work with such a great professor.

Besides my advisor, I would also like to thank Prof. Voicu Z. Groza and Prof. Miodrag Bolic for their brilliant comments and suggestions. Thanks for being an inspiration in many ways.

Many appreciations to Prof. Rafik A. Goubran for his insightful comments and suggestions to improve my dissertation. Your words of encouragements are still ringing in my ears. Special thanks to Dr. Saif Ahmad for the blood pressure monitor he designed and for his availability to support me when I needed.

I wish to also thank all members in our research group including: Dr. Izmail Batkin, Dr. Mohamad Forouzanfar, Dr. Mohamed Mabrouk, and Azadeh Dastmalchi, for all the encouragements and support. I would never forget all the discussions and chats we had together in the past few years.

Many thanks and appreciations to my beloved father Prof. Dr. Nabil S Abderahman and my mother. Words cannot describe the happiness I have. Finally, I can make you both proud! Of-course I would like to send my love to my brothers and my sisters: Mohammed Saif, Majd, Sama, Dhikra, and Shouaa. Without you my life has no taste.

I would like to thank my dearest friend, Ahmed Al-Eter. I greatly value your friendship and support.

I do acknowledge the outstanding service I received from the University of Ottawa's academic, administrative, and technical staff.

I like to end with Carl Sagan's quote:

"Somewhere, something incredible is waiting to be known."

Huthaifa N. Abderahman

`

TABLE OF CONTENTS

`

`

LIST OF FIGURES

`

`

`

`

`

`

`

LIST OF TABLES

`

LIST OF ABBREVIATIONS

ADC	Analog to Digital Converter
BP	Blood Pressure
BPF	Band Pass Filter
CP	Cuff Pressure
DAQ	Data Acquisition system
DBP	Diastolic Blood Pressure
DTW	Dynamic Time Warping
EMD	Empirical Mode Decomposition
ECG	Electrocardiogram
FDA	Food and Drug Administration
HPF	High Pass Filter
IMF	Intrinsic Mode Function
IMFSA	Intrinsic Mode Functions Selective Analyzer
IMFC	Intrinsic Mode Functions Collector
LPF	Low Pass Filter
LOA	Limits Of Agreements
LUT	Look Up Table
MU	Microcontroller Unit
ME	Mean Error
MAE	Mean absolute Error
mmHg	Millimeters of Mercury

`

MAP	Mean Arterial Pressure
MCU	Microcontroller Unit
NN	Neural Networks
OMW	Oscillometric Waveform
OMWE	Oscillometric Waveform Envelope
PTT	Pulse Transient Time
PPG	Photoplethysmograph
PWM	Pulse Wave Modulation
PIC	Peripheral integrated Circuit
RWTT	Reflected Wave Transit Time
RSS	Root Sum-Squares
SD	Secure Digital
SSA	Singular Spectrum Analysis
S/N ratio	Signal to Noise ratio
SDE	Standard Deviation of Error
SBP	Systolic Blood Pressure
STFT	Short-time Fourier transform
TCR	Temperature Coefficient of Resistance
TF	Transfer Function
TCGF	Temperature Coefficient of Gauge Factor

`

LIST OF SYMBOLES

ρ: Resistivity

ε: Strain

σ: Conductivity

μ: Mobility

Π: Piezocoeficient

A: Cross-section

E: Young's modulus

G: Gauge factor

K_b : Boltzmann's constant

L: Length

N: Doping concentration

R: Resistance

T: Temperature

P: Pressure

t: time

V: Voltage

`

CHAPTER 1: INTRODUCTION

1.1 Problem background

Automated non-invasive blood pressure measurements are widely used in our daily life, and as such devices are more user friendly, safer, and more economic than invasive measurements. In non-invasive blood pressure measurement techniques, the term "enhancing the accuracy" is used very often (e.g. Klinkenberg and Renz 1998; Gama and Castillo 2006). However, a few questions need to be asked: What degree of trust do we have in our home blood pressure devices? Are we trained enough to use them? How often do we need to calibrate them?

Although these questions are important, many studies show that even trained health workers do not take these issues fully into account (Leng et al. 2014). There is generally a lack of awareness of blood pressure measurement quality problems (Amoore 2012; Ando 2014).

It is possible to divide the issue of signal quality in blood pressure measurement into three main categories: short term, medium term, and long term. In the long term, drift in the sensor behaviour affects the measured signal. On the other hand, in the medium term, the measurement quality can be affected by environmental factors (Weisz and Francis 2011; Martel et al. 2013), while in the short term it can be affected by artifacts and other noise sources that corrupt the signal (Settels, 2014). Notable among these are artifacts due to sudden arm and body movements, and noise due to vibrations in a moving vehicle or resulting from tremor. The challenge in motion artifacts is that the system will often be facing non-stationary, and/or aperiodic noise sources.

One solution to counter long term drift is to monitor the changes in the system response and try to deal with them when they become substantial (± 3 mmHg according to international standards) (EN 1060-1:1996). Another standard that supports the need of such accuracy is the ANSI/AAMI SP10:2002 standard for electronic/automated sphygmomanometers, which recommends a standard deviation of error (SDE) of 8 mmHg and a mean error (ME) of ± 5 mmHg (ANSI/AAMI SP10:2002).

`

1.2 Motivation

Clinically validated blood pressure (BP) monitors can be divided into three main categories: Mercury, aneroid, and automated monitors. Even though the mercury blood pressure monitor is the oldest monitor among these three categories, it is still in use. In this type of monitor, the blood pressure estimation is based on Korotkoff sounds. On the other hand, aneroid monitors are mechanically-based due to their dial composition. Consequently, they require constant calibration. Finally, automatic monitors are electronic devices, so that the user can perform a full estimation by pushing one button (Medicines and Healthcare Products Regulatory Agency 2012).

Most of the currently available BP monitoring devices lack a calibration function which is either automatic or activated by the user. Consequently, these devices should be sent back to the factory once in a while to be readjusted to the factory setting. Calibrating blood pressure monitoring devices generally requires using a reference pressure monitor, which is connected to a T-shape tube (James et al. 1988; Mattu et al. 2001). The process requires the user to pass through different pressure cycles - high, zero, and low - to generate a few reference set points. Again, the issue here is not limited to time and cost, but it is rather a problem of how aware and knowledgeable the users of common blood pressure monitors are about the importance of regular calibration.

`

A study based on three-month old blood pressure monitoring devices in a hospital showed that there was a 25% failure in meeting the international calibration standard of ±3 mmHg (EN 1060-1:1996) among a total of 127 devices (18 mercury, 62 aneroid and 47 automated ones). Moreover, the respective failure rates were 6% for mercury, 31% for aneroid, and 26% for automated devices (de Greeff et al. 2010), as shown in Table 1.1 below.

Table 1.1 Calibration errors measured on various types of blood pressure monitors (adapted with permission from de Greeff et al. 2010)

Type	**Manufacturer**	**n**	**Calibration error [mmHg]**			
			0-3	3-5	5-10	>10
Aneroid	Accoson	10	7	2	1	0
	Hiene	11	7	4	0	0
	Speidel and Keller	2	1	1	0	0
	Welch	39	28	8	1	2
Automated	Criticare	3	3	0	0	0
	Datascope	25	15	5	5	0
	Dinamap	2	1	0	0	1
	Omron	1	1	0	0	0
	Welch Allyn	16	15	1	0	0
Mercury	Accoson	16	16	0	0	0
	Yamasu	2	1	0	0	1

`

In another study, a total of 501 blood pressure devices were tested, among them 50.3% were being used in teaching hospitals while 48.5% were mercury manometers (Ahmad et al. 2012). Most of the instruments had been purchased six months earlier and they were in use at that time. Results showed that 30.1% of overall instruments in use violated the ±3 mmHg standard (EN 1060-1:1996). Within the devices tested, 45.73% of aneroid type devices and 13.58% of mercury type devices violated the standard. Results from such studies show how serious the problem is. Note also that these studies were conducted in a professional clinical setting. Imagine conducting this study on home blood pressure monitors.

Hypertension affects approximately one billion individuals worldwide (Iyalomhe and Iyalomhe 2010). It is estimated to be responsible for 7.1 million premature deaths and 4.5% of disease burden. Overestimating or underestimating blood pressure measurement by even as little as 5 mmHg can result in over 20 million persons appearing to have normal blood pressure rather than hypertension. However, estimation of BP can be effected by either long term drift, medium term drift, or short term degradation of the measured signal, as described earlier. The problem with current BP monitors is that they are validated only in a clinical setting under controlled conditions (Parati et al. 2010). Another approach for validation that has been proposed includes multi-channel hardware for testing oscillometric blood pressure monitors (Postolache et al. 2013). Three measurements took place: the evolution of the cuff pressure during the BP estimation, cuff deflation dynamic mechanical stress measurement, and measurement of the blood pressure variation. The conducted experiment showed positive results towards an objective evaluation of oscillometric blood pressure monitors (Postolache et al. 2013). However, such tests do not accurately represent the device performance when operating under challenging operational conditions. Surprisingly, to date, there is no standard for validating the performance of a BP device under normal but challenging operating conditions, such as one that takes into account the effect of any sort of motion artifact.

The low number of published papers dealing with such problems makes this a fertile area of research. Among available publications, the most studied factor is the effect of temperature on the patient rather than the monitoring device (e.g. Hozawa et al. 2011; Halonen et al. 2011; Miersch et al. 2013). Furthermore, research regarding motion artifacts is mostly related to the effect of vehicle vibration, and has rarely addressed sudden movements in patients (Koo et al. 2007).

`

1.3 Contributions

The proposed work aims to develop a robust blood pressure monitoring system that adaptively compensates for short term disturbances in the measured signal due to motion artifacts, medium term drift due to environmental changes, and long term drift due to sensor ageing. There will be no need for any manual calibration, as the system will calibrate itself automatically against the above disturbances and drifts.

The proposed system makes novel use of Empirical Mode Decomposition (EMD) in a new developed algorithm, named Intrinsic Mode Function Selective Analyzer (IMFSA), to suppress transient motion artifacts, and it suppresses vibration motion artifacts using another algorithm named Intrinsic Mode Function Collector (IMFC). The novelty of the proposed algorithms comes from the fact that they both clean the signal without the need for a conventional filter.

With motion artifacts, transients or vibrations, there is no need to either store a database of artifacts or predict them. The system will deal with each measured pressure signal as a new case, and identify the motion artifact components using feedback from an integrated accelerometer sensor. Using this approach, the frequency content of the target blood pressure signal will be preserved (Seifedine 2012), which would not be the case if conventional filters were to be used.

With drift due to temperature changes and sensor ageing, a low level model based on semiconductor theory was derived to show the relation between the sensor's resistance and both temperature and ageing. A system was proposed which includes a stage to detect signals from the pressure sensor, and monitor its function using another EMD stage. This stage accumulates data read over time and translates it to an ageing trend, which is used later for system compensation. A temperature compensator stage is also provided to adjust the system for any temperature changes.

The long term drift problem in blood pressure monitors requires following a regular calibration schedule, which would add more pressure on home users as well as clinics. The sources of long term drift in blood pressure monitors can be in almost all stages of the device. However, the rate of this drift depends mainly on the components in each specific stage. In this thesis, the interest is to study the effect of ageing on the performance of piezoresistive sensors in non-invasive blood pressure measurement, an area in which there has been little previous work.

`

The approach taken in this thesis, to provide automated integrated compensation for short term disturbances (motion artifacts), medium term drift (environmental effects), and long term drift (sensor ageing) in blood pressure measurements, has not been attempted before. Moreover, the use of EMD for this application is completely novel. Overall, the proposed approach promises to help achieve non-invasive automated blood pressure measurements that are much more reliable than currently possible.

The following is a list of the current related publications and submitted manuscripts:

- H. N. Abderahman, H. R. Dajani, M. Bolic, V. Z. Groza,"An integrated system to improve robustness of non-invasive blood pressure estimation with motion artifacts", Proceedings of the IEEE Engineering in Medicine and Biology Conference(EMBC'15), Milan, Italy, August 25-29, 2015.

  Link: http://emb.citengine.com/event/embc-2015/paper-details?pdID=6202
- H. N. Abderahman, H. R. Dajani, M. Bolic, V. Z. Groza, "An integrated system to compensate for temperature drift and ageing in non-invasive blood pressure measurement", IEEE International Symposium on Medical Measurement and Applications (MeMeA16), Italy, May 15-18, 2016.

  Link: http://ieeexplore.ieee.org/document/7533751/?reload=true
- H. N. Abderahman, H. R. Dajani, M. Bolic, V. Z. Groza, "An integrated blood pressure measurement system for suppression of motion artifacts", journal paper under review
- An invention disclosure related to the methods for suppression of motion artifacts has been submitted.
- Other publications are in preparation.

`

1.3.1 Approach

The proposed work is carried out in the following stages:

- An IMFSA stage based on EMD is designed and built. It works in conjunction with a 3 axis accelerometer that will be integrated into the system. This stage is responsible for monitoring any transient movement that occurs during the blood pressure measurement, and acts accordingly to mitigate the effects of this motion.
- An IMFC stage based on the EMD algorithm is designed and built. This stage is responsible for monitoring and suppressing vibration movements with the help of measurements from a three axis accelerometer.
- A subsystem is implemented to monitor medium term drifts, temperature changes, and the respective changes in the pressure sensor's resistance. This subsystem is responsible later for monitoring and compensating the effects of temperature changes.
- A subsystem to monitor long term drift (ageing) is implemented. This stage is responsible for keeping track of any change in sensor's resistance over time. The compensation here takes place after the passage of a certain amount of time.
- Tests to examine the accuracy and the validity of the proposed approach have been carried out. The results demonstrate the behaviour of the proposed system under different challenging operating conditions.

  The obtained blood pressure estimates are compared with the corresponding estimates obtained by conventional approaches that do not include

1.4 Thesis Organization

This thesis is organized as follows. In Chapter 1, the focus is to introduce the problem dimensions and the expected contributions of this research. Chapter 2 discusses the problem background, and different approaches used in related studies in the literature. In Chapter 3, compensation for the effects of short term disturbances in the signal, with both types of motion artifacts, transient and vibrations, are discussed. Chapter 4 deals with medium drift due to changes in environmental conditions, while long term drift due to ageing is investigated in Chapter5. Finally, conclusions and suggestions for further work are presented in Chapter 6.

`

CHAPTER 2: BACKGROUND

2.1 Blood pressure estimation

Blood pressure estimation is a common medical measurement performed regularly by millions of people around the world. It helps in providing essential information about the state of health of an individual. It is estimated that one third of adults in the US have hypertension. However, around 33% of these estimated patients are unaware of their high blood pressure (Cutler et al. 2008).

In any blood pressure estimation, the result is provided in the form of two values: systolic and diastolic blood pressure (SBP and DBP). SBP is produced by the push of blood flow in the arteries near the beginning of a cardiac cycle, and corresponds to the maximum value of pressure in the arteries. DBP occurs at the opposite end of the cardiac cycle, as the heart is relaxing, and corresponds to the minimum pressure in the arteries (Geddes et al. 1982).

Methods for blood pressure estimation can be separated into two main categories: invasive and non-invasive methods. Invasive methods, also referred to as intra-arterial, are considered the most accurate (Myers and Valdivieso 2012). However, they require insertion of sensors in the arteries, and so are associated with significant risks. On the other hand, non-invasive methods, like the oscillometric method, palpation, or auscultation are more commonly used in general settings and are considered user friendly (Advanced Anesthesia Specialists, 2013).

The oscillometric method for blood pressure estimation, which was first developed by Marey in 1876, is the most popular approach used in automated non-invasive blood pressure devices. This approach requires a cuff wrapped around a subject's upper arm or sometimes around wrist, through which pressure pulsations are sensed (Figure 2.1).

`

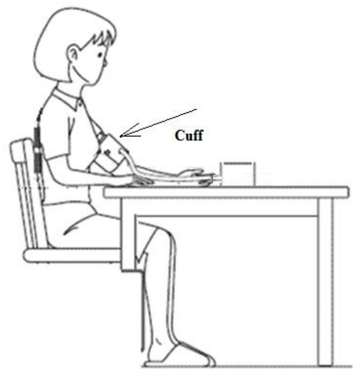

Figure 2.1: Cuff placement while taking a blood pressure estimation using the Oscillometric method.

The process of oscillometric blood pressure estimation requires several steps. First, the cuff is inflated to a pressure above systolic blood pressure and then it is deflated to a pressure below diastolic pressure, with a typical deflation rate of 2-3 mmHg/s (Yong et al. 1987). The measured cuff pressure is shown in Figure 2.2 below. It should be noted that the cuff pressure signal is composed of two components, a slow trend that reflects the deflation and small pulsatile oscillations due to changes in the intraterial pressure.

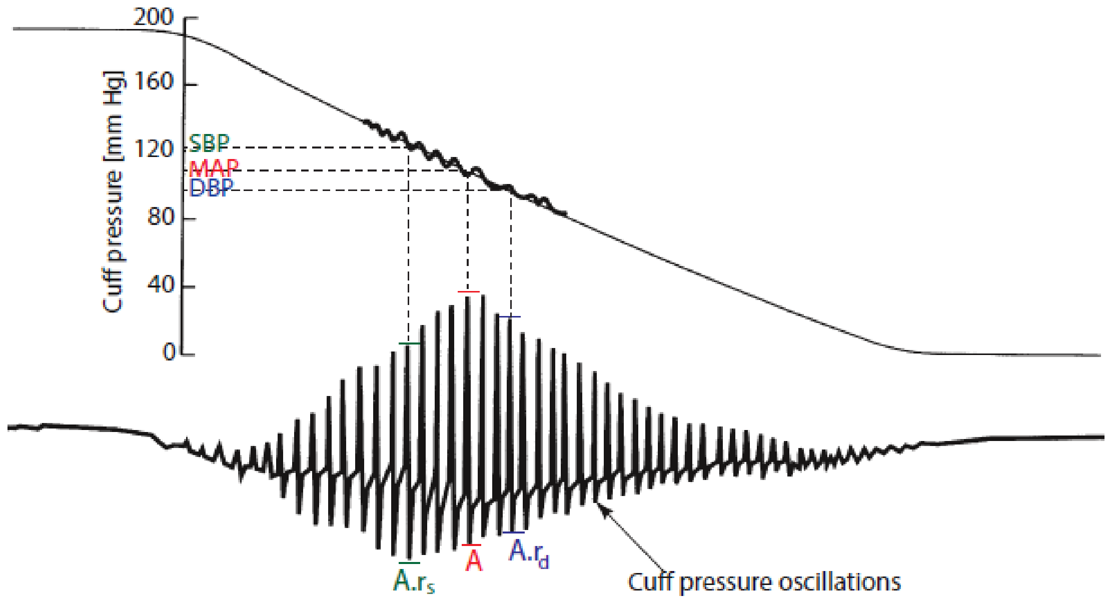

Figure 2.2: Oscillometric method for blood pressure estimation. Top: the deflation curve, bottom: the Oscillometric waveform. (Adapted with permission from Forouzanfar, 2014).

`

As shown in the figure above, the mean arterial pressure (MAP), marked as Ā, occurs at the peak in the OMW envelope. From Ā, both the systolic blood pressure and the diastolic blood pressure can be estimated using the so-called systolic and diastolic characteristic ratios r_s and r_d.

The next step involves extracting the oscillometric pulse waveform (OMW) using a band pass filter (BPF) (Sorvoja et al. 2005; S. Ahmad et al. 2012) or a high pass filter (HPF) (Jazbinsek et al. 2005). Alternatively, detrending can be used to extract the oscillometric waveform (Jazbinsek et al. 2005; Amoore 2006).

Different algorithms are used for peak detection in the OMW and these include amplitude threshold methods based on the Hilbert transform (Benitez et al. 2001), differentiation (Holsinger et al. 1971), adaptive amplitude thresholding (Shin et al. 2009), and zero crossing (Kohler et al. 2003).

To help locate the peaks, Ahmad et al. (2012) developed a blood pressure measurement device that simultaneously records the electrocardiogram (ECG) signal using two electrodes, one embedded in the cuff and another placed on the blood pressure monitor device that the user touches (Figure 2.3). This allows the recording of a single lead ECG signal, and the concept for detecting pressure pulses in this technique is based on the fact that, except in some uncommon pathological conditions, there is one pressure pulse peak located after each ECG beat. Figure 2.4 explains peak identification using this approach.

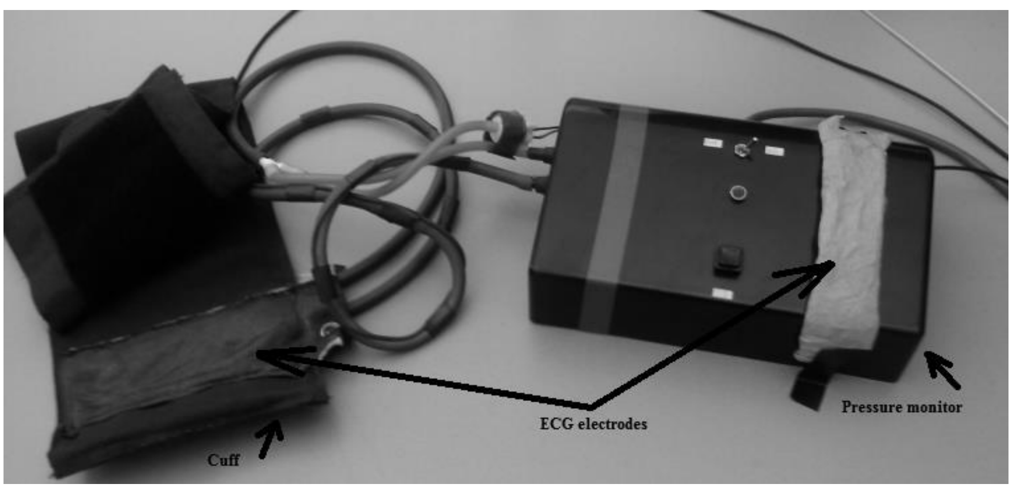

Figure 2.3: An Oscillometric blood pressure monitor with the feature of having two ECG electrodes embedded in it, as designed by S. Ahmad et al. (2012).

`

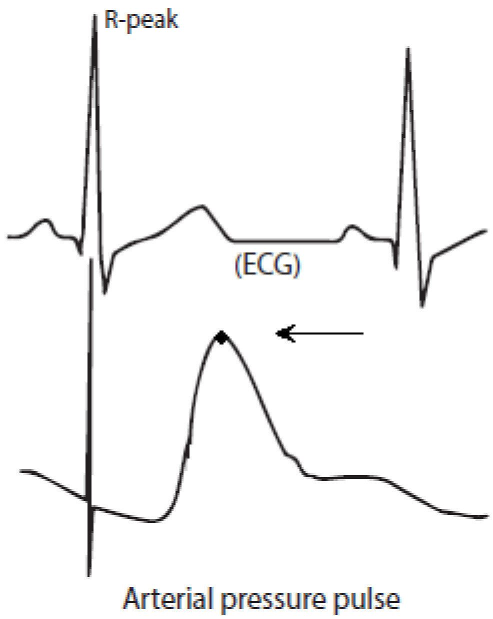

Figure 2.4: Pressure peak identifying approach based on simultaneously recorded ECG and oscillometric signal. The identified peak in the pressure pulse is shown with a dot (Adapted with permission from Forouzanfar, 2014).

The detected peaks are then used to generate the corresponding oscillometric waveform envelope (OMWE) (Ball-llovera 2003; Gersak et al. 2006), which is later smoothed (Geddes et al. 1982; Sorvoja et al. 2005; Jazbinsek et al. 2005; Chunbao and Lingjiao 2007).

The estimation of systolic and diastolic blood pressure is performed with the OMWE using different approaches. Typically, the Mean Arterial Pressure (MAP) is first detected as the cuff pressure that corresponds to the time index of the maximum amplitude from the generated envelope (Forster and Turney1986). The cuff pressure at which the amplitude of the oscillations reaches the systolic ratio (r_s) of the maximum amplitude A is then determined as the SBP. The cuff pressure at which the amplitude of oscillations falls down to the diastolic ratio (r_d) of the maximum amplitude A is determined as the DBP, as shown in Figure 2.2. The values of r_s range from 45-73 % of the maximum value corresponding to the MAP and for r_d range from 69-83 % of the MAP (Chen 2011; Forouzanfar 2014).

`

Other approaches have used Neural Networks (NN) (Forouzanfar et al. 2010; Lamonaca et al. 2013; Forouzanfar et al. 2015), in which a feature-based NN is designed to find an implicit relationship between the blood pressure and the corresponding oscillometric waveform envelope. Methods based on measurements of the Pulse Transient Time (PTT), which is the time delay between the initial contraction of the heart and the arrival of the pressure pulse at peripheral site, have also been described by several authors (Teng and Zhang 2007; Gesche et al. 2012; He et al. 2013; Forouzanfar et al. 2015).

2.2 Signal quality and blood pressure measurement

Blood pressure signals are known to be non-stationary signals (Yang, and Chon 2010), and so require advanced techniques to deal with them. Various methods are used in signal processing, ranging from conventional filters to computational intelligence methods. In this section, different techniques to monitor and/or enhance oscillometric blood pressure measurements are introduced.

2.2.1 Motion artifacts

Motion artifacts are a common problem in non-invasive blood pressure measurements (Pickering et al. 2005; Abderahman et al. 2015). Even small sudden motions can result in large signal changes. What makes it challenging is that these artifact signals might be interpreted as a pressure signal, which will result in erroneous blood pressure estimations (Stebor 2005; Balestrieri and Rapuano 2010). Therefore, blood pressure measurement accuracy can be seriously hindered by motion artifacts (Walloch 1990; Charbonnier et al. 2000).

Motion artifacts typically appear in the form of additional components superimposed on the measured signal. Sometimes such a portion is clearly identifiable (Reddy et al. 2009), at least visually, but at other times it is not. Although the problem is serious, a search of the literature shows that very little work has been done to deal with it, especially as regards transient motion artifacts. Even with the few methods that have been proposed, they have mostly dealt with the detection of such artifacts rather than with suppressing them.

`

Furthermore, current validation techniques and standards of blood pressure devices do not deal with maintaining accuracy in the event of patient motion or during patient transport (Friesen et al. 1981; Kimble et al. 1981; Diaprose et al. 1986; Cullen et al. 1987; Park et al. 1987; Sonesson et al. 1987; Wareham et al. 1987; Chia et al. 1990; Colan et al. 1993; Gevers et al. 1996; Papadopoulos et al. 1999; Nelson et al. 2002; Sorvoja et al. 2005; CAS Medical Systems 2010).

A marketed technology called Smartcuf^{TM} attempts to identify the occurrence of artifacts by combining blood pressure signals along with ECG recorded using gel electrodes placed on the chest. This technology has been claimed to be able to identify and disregard signals that are attributable to motion artifacts based on the ECG. One drawback of the method is the fact that having a peak between each two R-peaks is not enough to conclude that it is a true pressure peak, except in the case where the artifact is due to identifiable vibrations. Using the method, it would be difficult to deal with a case in which a large transient artifact appears in the OMW (Gibson et al. 2008).

To confirm the quality of the Smartcuf^{TM} performance, a study compared different blood pressure monitors in the presence of vibrations with and without the Smartcuf^{TM}. Results show an increase in the device accuracy of about 18% (Revision labs 1998). Another study that took advantage of other recorded vital signals proposed an offline method to monitor artifacts, where pressure signals were synchronized with ECG and Korkotkoff sounds in order to detect the artifact intervals accurately (Abdul Suko et al. 2012). The key idea there was that the Korkotkoff sounds would be noisy when artifacts occur, which allowed identification of those intervals.

Motion sensors such as capacitive sensors were used in other studies to generate an artifact reference signal (Choi et al. 2007; Park et al. 2007), and then an adaptive filter was employed to suppress the noise. The problem faced by this method was its instability, as the system kept producing oscillations even after the motion event ended. A patented method has also used recursive filters such as the Kalman filter to reject motion artifacts (Dorsett and Davis 1990). However, due to the fact that in motion artifacts, noise statistics change with respect to time (Bennett and Taylor 1991; Taylor et al. 1995; Chu et al. 2005), the use of such filter would not be the best first choice, as the degree of accuracy in this filter is inversely proportional to the processing speed.

`

Furthermore, using Kalman filters requires great care when choosing the appropriate stochastic and functional models, for which a detailed study of the targeted signal is needed. Errors in modeling the signal will cause the Kalman filter to diverge, which would degrade nonstationary signals like the blood pressure signal (Zaknich 2005).

Pulse matching techniques based on pattern matching were used as part of a fuzzy logic system and a regression model (Huo et al. 2006). Abnormal pulses which came from either measurement motion disturbance or cardiovascular abnormalities were detected offline. However, these techniques would be ineffective in the case of large and/or random interferences such as typical with transient motion artifacts. Another study by Theodora et al. (2014), investigated combinations of artifact due to transient motions and vibrations caused by vehicles. They used an accelerometer during invasive blood pressure measurements, and the technique was based on the reflected wave transit time (RWTT) model.

The system was implemented by implanting two accelerometers, and measurements were taken directly from the artery while the accelerometer readings were taken from positions directly above the artery and on opposite sides. The advantage of having two accelerometers on opposite sides of the artery was to achieve a differential mode measurement. What is interesting in this technique is that both sensors can monitor accelerations of the whole body, such as in the case of vibrations, and the arterial acceleration, but in different directions. Another use of accelerometers is in Photoplethysmograph (PPG)-based blood pressure estimations, as they provide a reference signal that can be used to implement an adaptive filter (Gibbs and Asada 2005; Abdul Sukor 2012).

Another study that investigated mixed motion artifacts with vehicle vibrations (in ambulances) (Koo et al. 2007) took advantage of having the accelerometer embedded in the cuff, in order to subtract it later from the pressure signal based on the following relation:

$$P_m(t) = P_c(\mathrm{t}) + P_a(t) \tag{2.1}$$

where $P_m(t)$ is the measured cuff pressure, $P_c(t)$ is pressure without the motion artifact, and $P_a(t)$ is the pressure interference added due to motion. Note that $P_a(t)$ was calculated based on repetitive trial and error experiments and not by extracting a system transfer function. During the experiments, a low pass filter (LPF) and an amplifier were employed to construct $P_a(t)$.

`

The use of simulators for calibration under such challenging measurement conditions is also not ready for real-world use yet. Simulators are designed to be references for calibrating blood pressure monitors. The more accurate their signals are, the more efficient the calibration process will be. In the case of calibrating against motion artifact, it is not possible to predict all kind of motions, including speed, strength and number of events during a specific measurement. This explains the lack of studies using simulators with motion artifacts (Balestrieri et al. 2013).

2.2.2 Environmental effects

As discussed above, it is not easy to control the conditions under which the BP measurements take place. Whether they take place at home or outside, environmental conditions vary all the time. Awareness of environmental effects on electronics in general is not new. Many researchers have tried applying different approaches to fully compensate for these effects or to at least to reach an acceptable level of accuracy (Fong et al. 2011; Bruins et al. 2012).

Again, the potential harm associated with an inaccurate medical device generally requires high performance accuracy. For non-invasive blood pressure measurements, the international standard ISO81060-2 requires a mean absolute error of less than 5 mmHg, while the ANSI/AAMI SP10:2002 requires the standard deviation of the error (SDE) to be less than 8 mmHg.(ISO81060-2 2009; ANSI/AAMI SP10:2002)**.**

In general, the term environmental effect involves all components of the environment conditions, including humidity, temperature and other factors. However, because piezoresistive sensors are the most common type of pressure sensors used in blood pressure monitors, the humidity factor can be neglected, and the effect of change in temperature is more important (Chao 2005; Zernike and Belavic 2012).

When the sensor is to be implanted in the human body, the drift is most likely to happen during the first few hours. During these hours, the sensor will warm up to reach internal body temperature (Nicolaas 1996). The drift in this initial period is too serious to be ignored, and in fact in some cases it can reach up to 10 mmHg.

`

Picker et al. (2000) used a calibration procedure that involved heating the sensor for about 30 minutes before starting the calibration process. This time gave the researchers the chance to study the response of the sensor in a temperature comparable to that found when implanted inside the human body. After heating the sensor, a mercury pressure meter was used as a reference due to its high stability and reliability (Skirton et al. 2011). On the other hand, other researchers recommend the use of digital pressure devices as a reference instead (Shah et al. 2012), because these are known to be both user and environmental friendly (Stergiou et al. 2012).

Another invasive blood pressure study done by Sharma et al. (2012) took advantage of having feedback of temperature changes obtained with a temperature-dependent thin film, which is integrated in the pressure sensor. A look-up table was generated ahead of time and it was used later on for compensation. Results show a fast recovery time for the pressure sensor (0.17 s).

Another way of thinking about this problem is to take advantage of the temperature coefficient of some electronic components. Casey et al. (2011) described a system based on the Wheatstone bridge and a differential amplifier. The circuit was provided with two additional resistors with negative and positive temperature coefficients to help compensate for the changes in the pressure sensor itself.

Another related approach was reported in Wang et al. (2011), which described a system based on a bridge connected with a transistor. The idea behind this approach was based on the fact that the transistor resistance has a negative temperature coefficient, which can be used to compensate the bridge output change due to the temperature.

The use of a differential amplifier to measure pressure values is described in Kress et al. (1990)**.** The proposed system monitors temperature changes by measuring system behaviour under different operational temperatures and compensates for changes using an offset subtraction stage. A method of soldering the pressure sensor in a vacuumed package is shown in (Totsu et al. 2005)**.** This step was done to suppress thermal drift during in-vivo tests later on (Birch and Morris 2003).

`

Another study shows a technique of using the Schering Bridge, which makes it easier to determine changes in sensor behaviour due to temperature changes or ageing in general. Drifts in this bridge will appear as a phase shift instead of a voltage difference, which can make them easier to identify (Sarath and Komaragiri 2012).

A method that combined both hardware and software to accomplish the temperature compensation is introduced in Xu and Liu (2013). The authors reported a high degree of compensation using a temperature sensor integrated with the pressure sensor. Data were collected in the form of a coefficient matrix, which was translated to a temperature compensation model. This model was used as a reference for comparison later on. Results show an improvement in both accuracy and linearity.

2.2.3 Ageing (Time drift)

Time drift is considered another source of error in blood pressure estimation, but in this case, the error source comes from the device itself. One of the main components in any automatic blood pressure system is the pressure sensor. Typically, this sensor is made of a piezoresistive material, which has advantages over other types of pressure sensors. Piezoresistive sensors are superior in terms of integration on a chip, high dynamic range (Eswaran and Malarvizhi 2013), Signal-to-Noise performance (Neumann et al. 2004), and immunity to humidity (Chao 2005; Zernike and Belavic 2012).

With any measurement device, calibration is a commonly recommended practice to compensate for sensor drift due to ageing. With medical devices in particular, periodic calibration is usually critical to avoid potentially harmful consequences. Many calibration approaches and recommendations for blood pressure measurement devices are available, but they are mostly manual. They either require sending the device to the manufacturer (NHS 2008), or they might ask the user to follow a specific procedure to accomplish all the calibration steps (Empress 2008). These calibration procedures usually require a reference device, and the choice for a reference varies between mercury manometers (Muecke et al. 2009), electronic reference devices (Pinet et al. 2005), or mechanical gauges (Seo et al. 2012).

As shown in Figure 2.5, the calibration steps include connecting the blood pressure monitor under test to a reference monitor using a T-shaped tube, and following a certain pressure schedule containing different pressure set points (Noharm Organization2013).

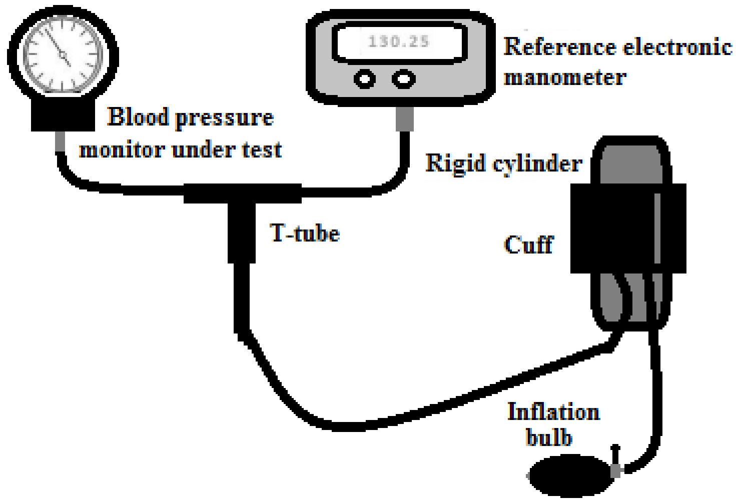

Figure 2.5: System setup for the process of calibrating a blood pressure monitor using another reference monitor.

An important factor to consider before choosing a reference for calibration is whether the required type of blood pressure measurement is invasive or non-invasive. Chavko et al. (2007) introduced a method to calibrate invasive pressure sensors using the OhmedaXcaliber calibrator device.

The process involved connecting both the pressure measurement device and the calibrator together, and covering different points along the pressure range between 0 to 400 mmHg. These predefined test points were used as a permanent reference for calibration after that. deGreeff et al. (2010) introduced a method using the same procedure but which uses a DPI 610 pressure calibrator.

Another common calibration procedure in invasive studies is the use of in-vitro tests instead of having a reference. In this case, the pressure sensor is put in a controlled chamber, where pressure varies over time. This kind of test helps the researcher to determine a calibration curve, thus allowing prediction of the sensor response (Fiala et al. 2013). Note that the calibration range used was between 0-250 mmHg to ensure covering the whole operating pressure.

`

Another invasive study described an automatic calibration system that was installed and integrated in a continuous flow ventricular assist device (Eigler et al. 2011). This calibration system took advantage of the atmospheric pressure in the lungs to generate a reference point, which was used for calibration purposes.

Counting on atmospheric pressure for calibration purposes was also introduced by Shi et al. (2011). In this study, the calibration technique was done based on the fact that the intra-thoracic pressure could be substituted for atmospheric pressure as lungs are open to air, which makes it a fixed point for calibration.

The use of an implanted pressure transducer connected to a telemetry channel was introduced by Samson et al. (2011). This method was based on pressurizing the animal under test at both positive and negative levels while recording the related shifts through telemetry. This research showed that a relation between these shifts and the pressurization takes place as long as the animal was in steady state during that time. Taking advantage of this relation, a calibration was performed by an implanted transducer. The transducer was connected with a body plethysmograph, which was responsible for monitoring the applied pressure of 8 mmHg above and below atmospheric pressure. Other groups used similar telemetry data obtained before and after implanting a pressure sensor as reference data for calibration purposes (Zwijnenberg et al. 2011; Montiel et al. 2014; Choy et al. 2014). This reference data was stored in the form of a look-up table, which included a few set-points that could be utilized later.

For non-invasive measurements, the available choices for a reference are mercury meters (Papaioannou et al. 2012), simulators (Newell 2013:30; Balestrieri et al. 2013; Riedel et al. 2011), aneroid sphygmanometers (Ostchega et al. 2011), and other automatic pressure devices (de Greeff et al. 2010). One drawback in having a device calibrating another is that the reference device may not itself be well calibrated. That is why the most common device used as a reference is the mercury blood pressure meter (de Greeff et al. 2010). Simulators are still not widely used as calibrators; they are still in an early phase of testing and they cannot yet be considered as a reliable reference. The challenge here is reaching a point where the generated signals are considered accurate enough.

`

The use of an aneroid sphygmanometer was presented by Ostchega et al. (2011). The approach involved a calibration procedure using the Netech Digimano digital vacuum meter. The measurements took place on a weekly basis for 1.5 years of the project's life to ensure an accurate performance. No details were given about the calibration procedure that took place during the experiment. This is typical for most of the published studies, as they mention that there was a calibration procedure followed, but with no or few details.

The procedure to calibrate a device using a Netech Digimano digital vacuum meter according to the Carolina Population Center (Whitsel et al. 2015) is to connect the device to be calibrated with the NetechDigimano digital vacuum meter using a T-connection, and start from a pressure value of 280 mmHg and keep decreasing it 20 mmHg in each step until reaching 20 mmHg.

Another interesting research project monitored the ageing of discrete sensors by comparing the signal-to noise-ratio (S/N ratio) before and after applying an accelerated ageing process (Santo et al. 2010 and 2013). The authors reported that it is possible to identify small cracks on the sensor's diaphragm that develop as the sensor ages.

2.2.4 Conclusion

As can be seen from the literature, there are many areas of research that are still open when it comes to the improvement of blood pressure measurement quality. Having a blood pressure monitor either at home or in a clinic requires paying attention to factors that can negatively affect the measurement. Similarly, there is a need to address the problem of artifacts that occur during patient transport. Currently available technology does not include an auto-calibration process that compensates against short term artifacts, medium term changes due to changes in environmental conditions, or long term drift due to ageing. The lack of relevant research is particularly acute with the non-invasive oscillometric method, as there are a few publications related to invasive blood pressure measurements. Moreover, in the small number of relevant publications, the focus is usually on detecting artifacts or drift, rather than trying to solve the issue.

`

2.3 Empirical Mode Decomposition

2.3.1 Introduction

Empirical Mode Decomposition (EMD) was first introduced by Norden Huang in 1971 (Huang et al. 1971) as a method to decompose complex signals into finite components, called intrinsic mode functions (IMFs).

Each IMF should satisfy the following rules:

1. The number of extrema and the number of zero-crossings in the whole dataset must either be equal or differ at most by one.
2. The mean value at any point of the envelope defined by either the local maxima or the local minima envelope is zero.

The algorithm basically aims to produce smooth envelopes, which are defined by local maxima and minima of a sequence, and then subtracts the mean of these envelopes from the initial sequence. This requires the identification of all local extrema in the sequence under test as shown in Figure 2.6.

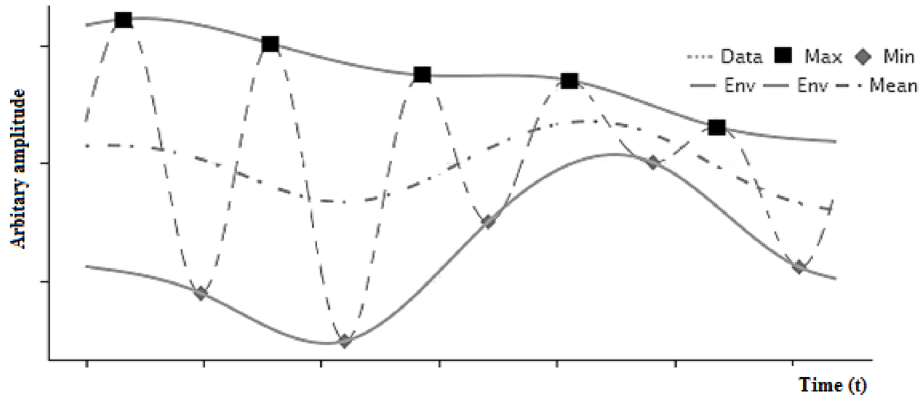

Figure 2.6: Time domain signal x(t) showing both the upper and the lower envelopes.

`

In Figure 2.6, the mean was calculated based on the two envelopes, generated by locating extrema points throughout the signal.

The choice of having EMD here as the core of the new algorithms to suppress artifacts and compensate for drift is because with EMD, signals are considered at the level of their unique local oscillations; the algorithm deals with each signal as a special case. Furthermore, the algorithm has the ability to auto-calibrate itself with respect to the signal that has been processed (Flandrin et al 2004).

In the literature, EMD has been used in a wide range of applications, and some that involve denoising or removing trends are described next. One such application was denoising electromagnetic interference components from ground penetrating radar signals (Battista et al. 2009), in which a method of amplitude modulation for IMF reconstruction was introduced. Adaptive filtering based on the ability of EMD to denoise signals, is considered another important application. This approach was used by He et al. (2014) for acoustic echo cancellation. Results obtained showed that the algorithm was able to model the system's transfer function and track different changes in an unknown environment faster than the one using a normalized adaptive filtering structure approach.

Another application of EMD is in signal enhancement. Research presented by Looney et al. (2008) used the algorithm for enhancing speech signals. The proposed approach was based on comparing the generated IMFs with a filtered reference noise. Another group, He et al. (2011) and (2012) used EMD for enhancing the quality of ECG signals. A method based on Ensemble Empirical Mode Decomposition (EEMD) was used to filter out both Gaussian noise and contact noise in raw ECG signals. Based on the results, the proposed method shows better performance in comparison with other filtering methods.

Hasan and Hasan (2009), developed an EMD-based system to remove musical noise from speech signals. The algorithm was based on the fact that musical noise always appears in the first few IMFs, which made them easier to be automatically removed.

`

Other applications for EMD include statistical approaches (Khaldi et al. 2008; Wu and Huang 2009; Baykut and Akgul, 2010; Boutana et al. 2011), which focused more on extracting information regarding system behaviour based on the IMFs, while others used the EMD approach for signal trend identification (Flandrin et al. 2004). The approach used by Flandrin et al. for detecting the trend is based on an algorithm named the ratio approach, in which an IMF that reflects the trend is detected using an algorithm based on the ratio between each IMF that is extracted and the one before it. In another study, Pinheiro et al. (2012) combined both EMD and Principal Component Analysis (PCA) to a set of cardiovascular signals to separate different components of the signals such as the baseline noise.

2.3.2 EMD algorithm

The algorithm can be divided into three main steps:

1- Interpolation (typically using cubic spline).

2- Sifting process in order to extract and identify intrinsic modes.

3- Numerical convergence criteria to help stop the iterative process after ensuring that all IMFs have been identified.

Empirical Mode Decomposition algorithm:

Running the algorithm requires performing the following detailed steps:

1. Identify all local maxima and minima of the time domain signal $d_o(t) = x(t)$

2. Interpolate between all the maxima and connect them by a cubic spline curve. Same process applies for the minima. Results will generate the upper and lower envelopes $e_u(t)$ and $e_l(t)$, respectively.

3. Compute the mean m(t) of the two envelopes:

$$m(t) = \frac{e_u(t) + e_l(t)}{2} \quad (2.2)$$

`

4. Extract the new signal (sifting process)

$$d_1(t) = d_o(t) - m(t) \tag{2.3}$$

5. Loop back to "1" until the corresponding signal $d_k(t)$ can be considered an IMF, where:

$$C_1(t) = d_k(t) \tag{2.4}$$

6. Loop back to "1" on the residual $r_n(t) = x(t) - C_n(t)$ in order to get all the time domain signal's IMFs $C_1(t)$,$C_2(t)$.., $C_N(t)$.

The algorithm terminates when the resultant residual signal is constant, has monotonic slope, or is a function with only one single extrema (Flandrin et al. 2004). The flowchart in Figure 2.7 below summarizes these steps.

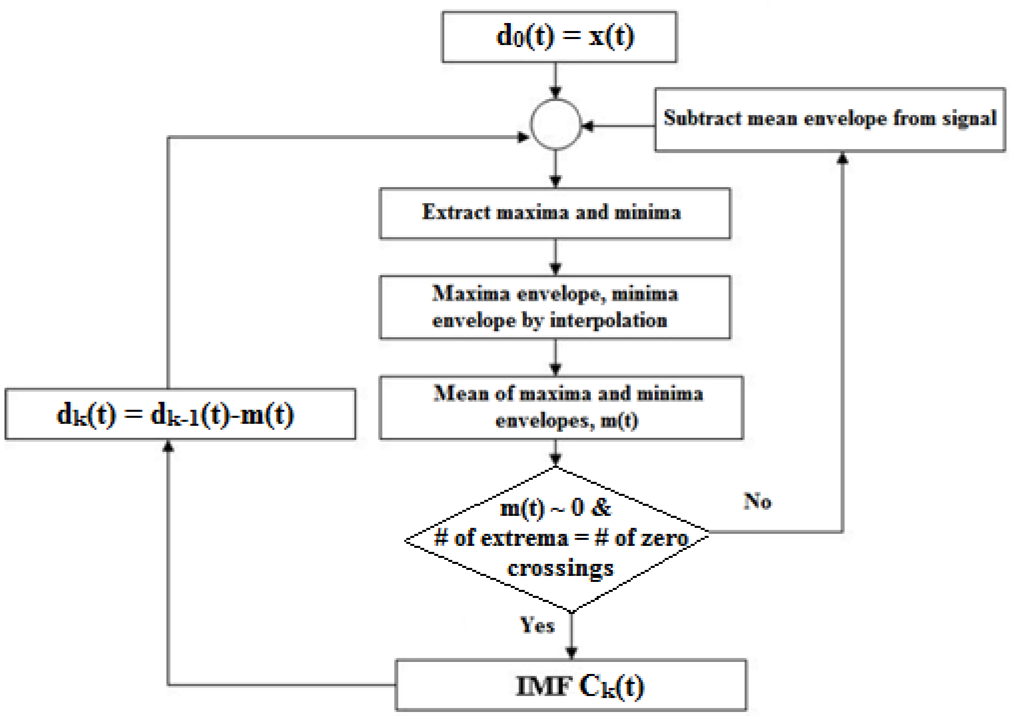

Figure 2.7: A flowchart of the Empirical Mode Decomposition algorithm.

`

Challenges associated with EMD vary with the application. A difficulty can be encountered when attempting to determine a suitable stopping criterion (Chen et al. 2006). The condition for an IMF to be considered is having a zero mean value of the upper and lower envelopes, or at least a value close to zero. However, over-sifting the signal to try meeting this condition may result in removing the physically meaningful amplitude variations in a certain IMF. Another issue that might concern some applications is referred to as the border effect (Rilling et al. 2003), which is basically the risk of generating extra IMFs due to the way the start and end points of the signal were chosen before being fed to the algorithm. Sampling time is another factor to be considered, as there is a risk of missing an extrema point if the sampling time is too long (Stevenson et al. 2005).

`

CHAPTER 3: SUPPRESSION OF SHORT TERM DISTURBANCES DUE TO MOTION ARTIFACTS

3.1 Introduction

It is always recommended to stay calm, relaxed, and to sit with a certain posture while taking a blood pressure measurement (Rabi et al. 2011; Cicolini at al. 2011; Brien et al. 2013). On the other hand, a technology to deal with the effects of even simple movements during a measurement is not yet embedded in commonly used blood pressure monitors. In this chapter, a method to detect and suppress the effect of motion artifacts, both in the form of transients and vibrations, is presented. With transient motion artifacts, the method is referred to as the Intrinsic Mode Functions Selective Analyzer (IMFSA), while with vibration; the method is referred to as the Intrinsic Mode Functions Collector (IMFC). The core of both methods is an EMD stage, which is responsible for generating the required IMF signals as will be shown below (Abderahman et al. 2015).

3.1.1 Effect of vibrations

Taking a blood pressure measurement in a moving vehicle, such as an ambulance, is often required. Paramedics may need to check on a patient's vital signs during transfer to the hospital. This means that blood pressure estimation will be susceptible to the vehicle vibrations, which appear as high frequency components superimposed on the pressure signal, as shown in Figure 3.1 below.

`

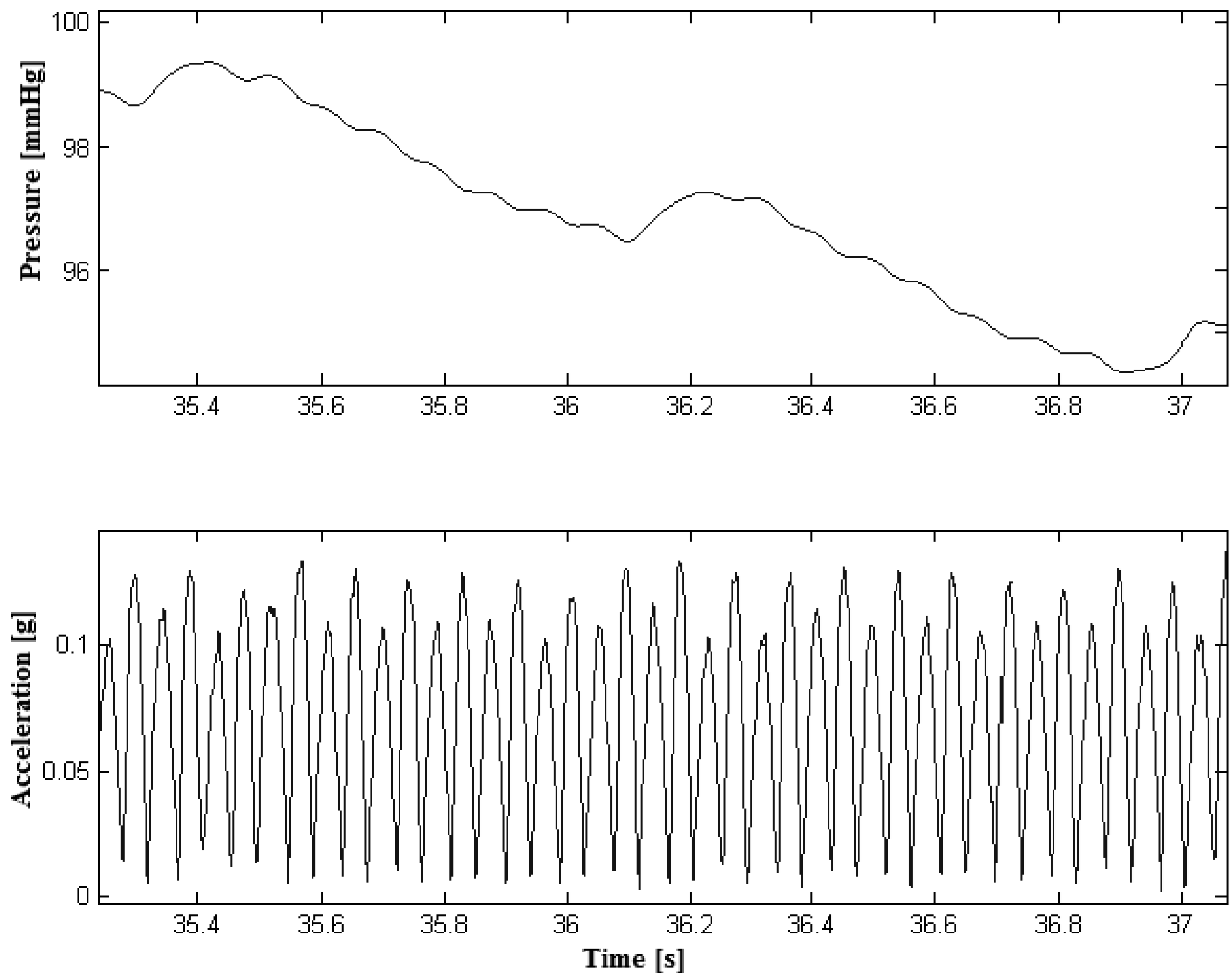

Figure 3.1: A zoomed-in region for a vibration signal (below) and as it appears in the oscillometric blood pressure waveform during approximately one pulse period (above).

According to Gunaselvam and Niekerk (2005), the vibration frequency in vehicles, as experienced by passengers under usual driving conditions, varies between 10–25 Hz with an acceleration magnitude of 0.1 to 0.2 g.

`

3.1.2 Effect of transient motion artifacts

As recommended, the patient should stay still until the blood pressure measurement is completed. In cases where a patient moves his/her arm during a measurement, this motion will appear in the recorded pressure signal, as shown in Figure 3.2 below. The risk here is that this unwanted signal will be treated as part of the pressure signal, degrading the accuracy of the measurement or producing completely erroneous estimates.

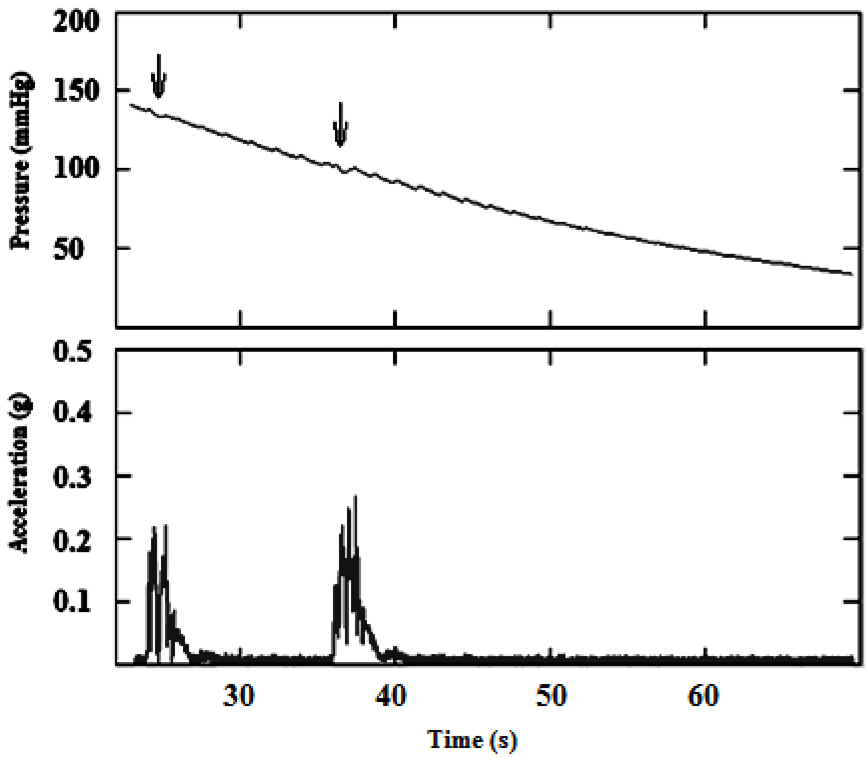

Figure 3.2: Example of a cuff pressure deflation signal (above) affected by two motion artifacts, as recorded by an accelerometer (below).

From Figure 3.2, it is clear that the accelerometer was able to detect two events of motion artifact during the measurement. These events also appear in the pressure deflation curve.

Because the motion artifact signal is not sustained, using a filtering approach such as an adaptive filter would not be the best choice, because it would be difficult for the filter to adapt during the transient interval of the artifact (Gao et al. 2010).

`

On the other hand, wavelet-based methods require predefined thresholding, resolution level, and a specified wavelet before they can be applied (Donoho 1995). To overcome these problems and to design a system that can cope with both the uncertainty and transience of motion artifact signals, the choice was made to use an EMD based filtering method to suppress them in the recorded signal.

3.2 Methods

The proposed approach takes advantage of having an accelerometer embedded in the blood pressure monitor cuff, in order to detect and quantify the type of motion that occurs during blood pressure estimation. The accelerometer used is a 3-axis accelerometer (MMA7361L, Freescale Semiconductor, Austin, Texas), shown in Figure 3.3. This accelerometer was chosen due to its low power consumption, size, and sensitivity (acceleration is detected between ±1.5g and ±6g). Refer to Appendix B for the datasheet.

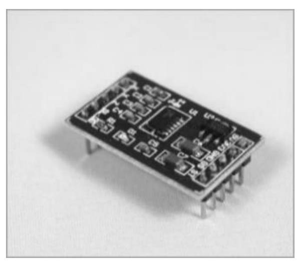

Figure 3.3: The 3-axis accelerometer by Freescale Semiconductor (MMA7361L) used in this study.

A high level diagram of the overall system used for distinguishing vibrations from transient motion artifacts is shown in Figure 3.4. The selector compares the time series accelerometer signal's power over the period of the measurement, using a window of size 512. (Lathi and Ding 2009). The algorithm then compares results obtained in all the windows. The decision will be made based on the fact that periodic signals result in a uniform power over the whole time series, while aperiodic signals result in varying powers levels during the whole set. Therefore, if the differences in power between the windows are greater than a threshold (here taken as 10%), the signal is classified as transient.

`

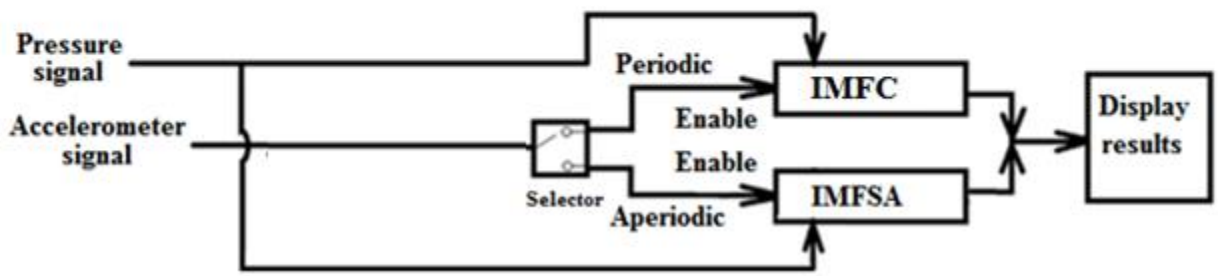

Figure 3.4: Overall block diagram of the artifact suppression system including both the IMFC (Intrinsic Mode Functions Collector) and the IMFSA (Intrinsic Mode Functions Selective analyzer) algorithms.

Both approaches require having IMFs generated by an EMD algorithm. As mentioned in Chapter 2, the EMD method deals with each signal as a special case. Each time a new signal enters a signal processing stage based on EMD, the algorithm will decompose it without the need of having a pre-selected basis. In other words, the EMD algorithm deals with signals at the level of their own local oscillations (Labate et al. 2013).

3.2.1 System set-up

During each experiment, the ECG, cuff pressure, and accelerometer signals were all collected synchronously using National Instruments hardware and LabVIEW software (Austin, Texas), transmitted to a personal computer, and processed in Matlab later on. The prototype (named InBeam) to collect the ECG and pressure signals, shown in Figure 3.5, was designed and assembled by Ahmad et al. (2012). The hardware/software which simultaneously collects the signal from the accelerometer placed on the cuff was added in the current work. This device also concurrently collects the ECG which is used to help in the detection of the individual pulses in the pressure signal. These in turn are used to construct the oscillometric signal. However, the algorithms described in this thesis do not depend on the recording of an ECG signal, and can be used with other methods that measure the oscillometric signal. Therefore, the approaches described in this paper are general and can be integrated in any oscillometric blood pressure monitor.

The InBeam prototype has four main components: an analog ECG amplifier, a pressure transducer, a mini dc air pump, and a screw-controlled manual pressure release valve. The ECG amplifier is built using an instrumentation amplifier (INA-129, Texas Instruments, Dallas, Texas) that operates on a dc voltage of ±5V and has an output in the range of 20–2000 μV. The pressure transducer

`

used in the prototype is the Vernier pressure transducer (BPS-BTA, Beaverton, OR). The output voltage from the transducer is in the range of 0-5V, which corresponds to a pressure range of 0-250 mmHg.

Inflating the cuff is done through a 6V mini air pump with the ability to control the inflation speed through a screw-controlled manual pressure release valve. On the National Instruments CompactDAQ data acquisition system, the input module NI 9239 was used to harvest both the ECG and the cuff pressure signals, while the NI9234 input module was used for the acquisition of three accelerometer data channels (x, y and z). The signals were conditioned, buffered and sampled using a 24 bit ADC (analog to digital converter) at a sampling frequency of 2000 Hz.

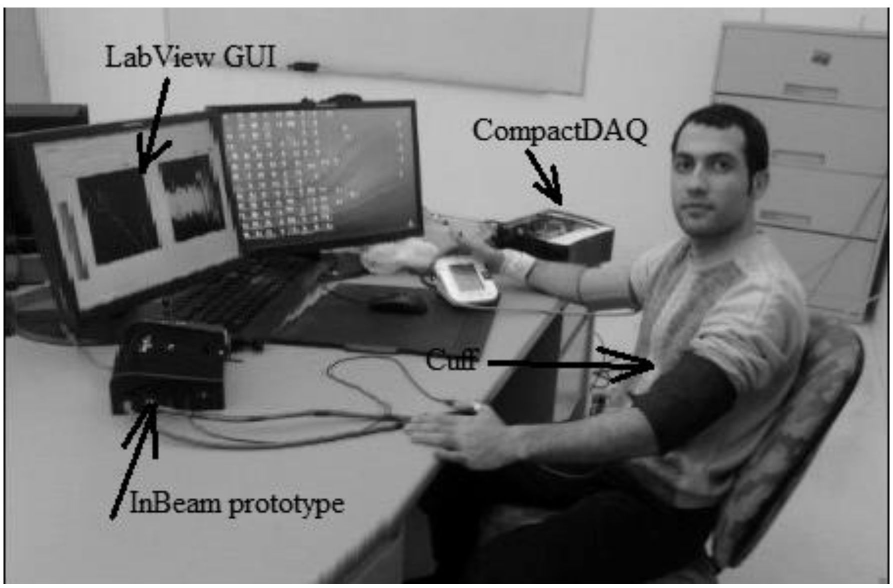

Figure 3.5: ECG, cuff pressure, and accelerometer recording system, where the InBeam prototype and the CompactDAQ are both shown.

The accelerometer placement on the cuff is shown in Figure 3.6 below.

`

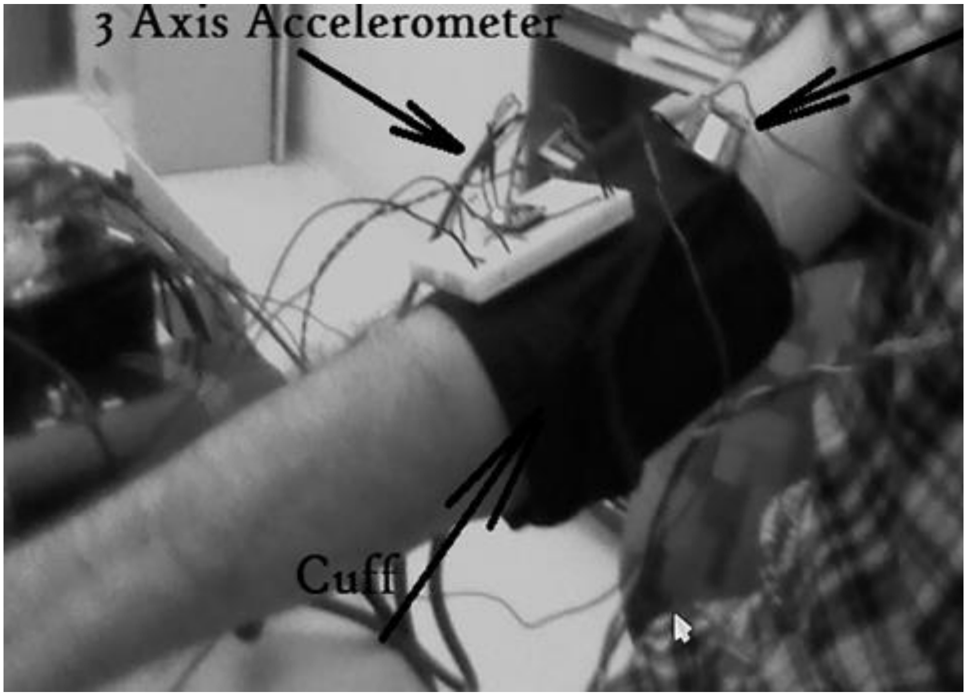

Figure 3.6: Location of the 3 axis accelerometer on the cuff, as it was used in the experiment.

Furthermore, in all parts of the experiment, the Food and Drug Administration (FDA)-approved Omron HEM-790IT monitor was used as a reference device.

The focus of the study is to demonstrate that the proposed algorithms have succeeded in suppressing motion artifacts, and so the estimates obtained using the InBeam device are compared before and after suppression of the artifacts. The utilization of the Omron device was to provide a fixed reference point for the estimates before and after suppression.

To mimic vehicle vibrations, a vibration motor model Uni Vibe 45mm–28mm (Precision Microdrives, London, UK) was used. Figure 3.7 shows both the motor and the subject posture used to test the effect of vibrations on blood pressure measurements.

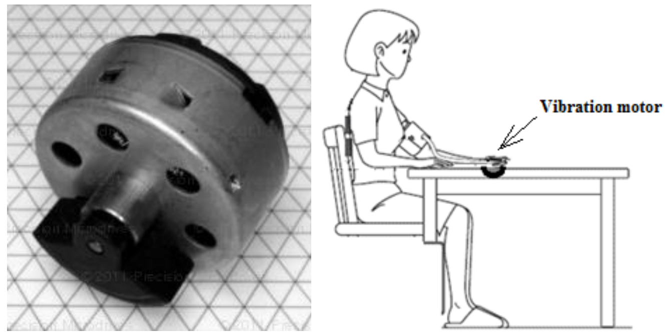

Figure 3.7: Left: The vibration motor model Uni Vibe 45mm-28mm (Precision Microdrives). Right: Subject posture during the experiment.

One of the advantages of using this motor is that it allows control of vibration frequency, speed, and acceleration by varying the input voltage. The motor's datasheet includes a graph that shows how varying the voltage leads to different frequency, speed, and acceleration operating points (Appendix C). From Figure 3.8, it can be seen that the control over the speed is done through the duty cycle of the pulse wave modulation (PWM) signal supplied by a microcontroller (PIC18f458, Microchip Technology Inc., Chandler, Arizona).

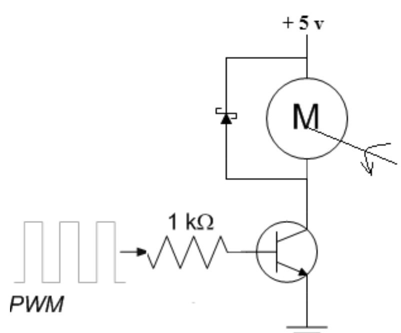

Figure 3.8: Vibration motor speed control circuit using pulse width modulation (PWM) signal fed to the base of an NPN transistor.

`

Moving on to transient motion artifacts, the analysis is also based on the five different signals: an ECG signal, the 3-axis accelerometer signals, and a cuff pressure signal, again all recorded synchronously. The signals from the accelerometer record the acceleration that occurs on the three different axes; x, y and z as shown in Figure 3.9.

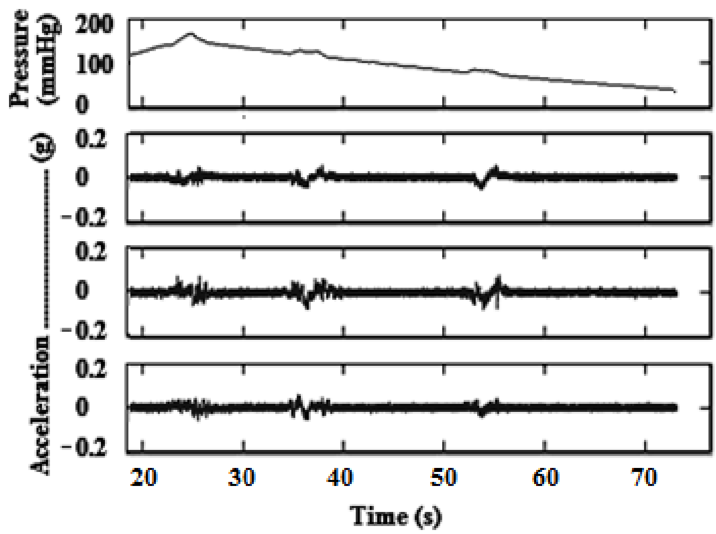

Figure 3.9: A cuff pressure signal (during the last portion of inflation then followed by deflation) affected by transient motion artifacts (top) with the corresponding x, y, and z signals from the accelerometer (2nd plot to bottom).

Processing the three accelerometer signals to locate intervals of motion requires the following steps:

- Smoothing each signal separately using a 1000 point moving average filter.
- Averaging the 3 axis signals using the following formula:

$$R(t) = \sqrt{x(t)^2 + y(t)^2 + z(t)^2} \tag{3.1}$$

where, x, y and z are the signals from the corresponding axes.

`

In Figure 3.10 below, the processed accelerometer signal R(t) is shown synchronized with the cuff pressure signal.

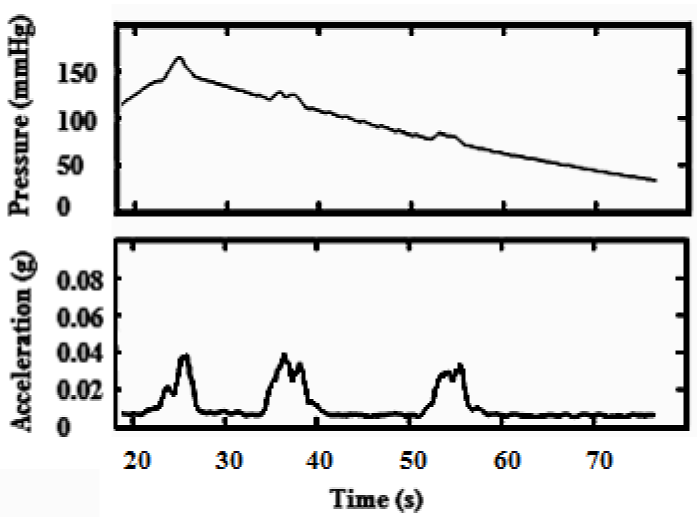

Figure 3.10: Example of a smoothed cuff pressure affected by motion artifacts (top) with the corresponding processed acceleration signal R(t) (bottom).

Comparing the oscillometric waveform that is extracted from the cuff pressure signal with the obtained accelerometer signal (Figure 3.11), it is seen how it correlates with the accelerometer signal (in this case with a correlation coefficient of 0.88).

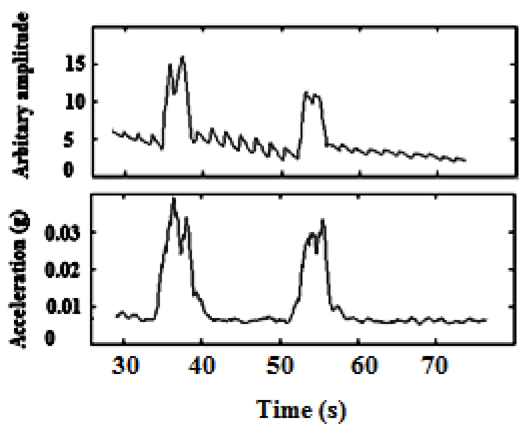

Figure 3.11: Example of a smoothed oscillometric signal (top) with the corresponding acceleration signal (bottom) recorded in one of the conducted experiments.

`

Furthermore, Figure 3.12 below shows the correlation between the accelerometer signal and the cuff pressure signal during events of artifact motion for all the collected cases. The high correlation between the two signals allows the use of the accelerometer signal to detect the intervals of artifacts in the oscillometric signal.

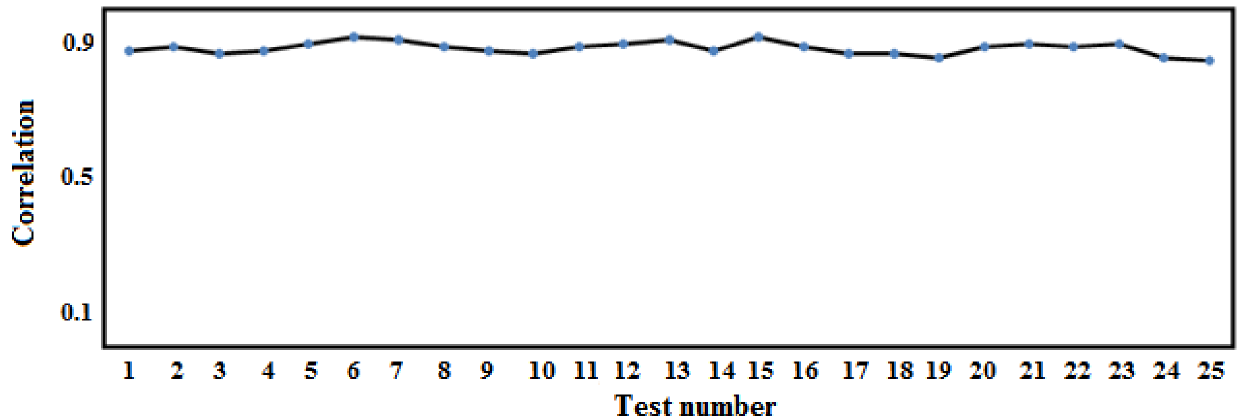

Figure 3.12*:* Correlation between the accelerometer signal and the cuff pressure signal during events of motion artifact, evaluated over all the study cases.

3.2.2 Experimental protocol

This study is based on data obtained from five healthy subjects (males of age range 22 – 30 years) with each performing 5 recordings with transient motion artifacts (for a total of a 25 datasets) and 2 recordings with vibration artifacts (for a total of 10 datasets). Using the system set-up described in subsection 3.2.1, the following steps were followed for each subject:

- A brief description of the study, the goals and the procedure were explained to all participants before starting the measurements and informed consent was obtained in accordance with the requirements of the University of Ottawa Research Ethics Board (Ethics approval: H 09-14-06).
- The participant sat in a comfortable seat with his left arm relaxed on a supporting table.

- Blood pressure measurements were taken on both participant arms. The laboratory (InBeam) prototype was used to measure the blood pressure from the left arm, and accelerometer motion data and ECG were recorded simultaneously. The reference blood pressure measurement was taken on the right arm, just after the left arm measurement, using the OMRON blood pressure monitor.
- A single-lead ECG was measured using two gel electrodes placed on the participant's chest as shown in Figure 3.13, with a ground point on the right hand. Lotion was applied under the electrodes to decrease skin resistance.

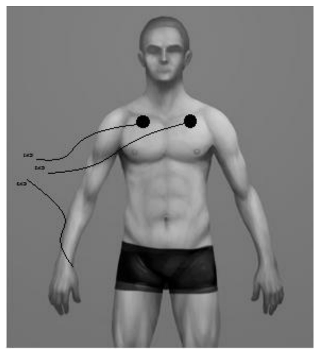

Figure 3.13: Electrode locations used for recording the ECG.

- The participant was asked to perform a few movements during the measurements, such as: moving his arm in a trigger motion, shaking his hand, moving his fingers, and holding a vibration motor. The actions followed the order shown in Table 3.1 below, and more details on the performed movements are found in Appendix A.

Table 3.1: Protocol for motion artifact experiment performed by the subjects

Test description	Number of tests / participant*
Elbow up twice	2
Fingers tapping three times	2
Hand up once	1
Emulate vehicle vibration	2 (Strengths: approximately 0.05 and 0.15 g)

*** Estimated time: 2 min / test**

`

- When testing the effects of vibrations, the participant was asked to place his hand on top of a vibration motor. During the test, the strength and the duration of the vibrations were chosen not to exceed the limits set in the international ISO 2631-1:1997 standard.

- To avoid stressing the participants, a five minute gap was placed between tests, resulting in a total of approximately 45 minutes for each session per participant.

From the total dataset, three sets were randomly chosen and used for the purpose of developing the algorithm, as will be shown in the next subsection.

3.2.3 Intrinsic Mode Functions Selective Analyzer (IMFSA) for transient artifact suppression

IMFSA is a new algorithm that is based on EMD and proposed in this thesis. The approach requires obtaining all IMFs from both the OMW and the accelerometer signal. Examples of the IMFs obtained from both these signals are shown in Figures 3.14 and 3.15.

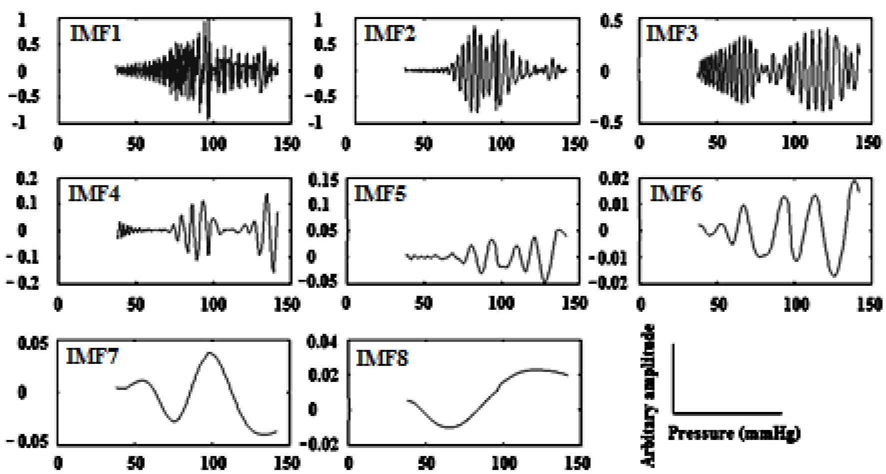

Figure 3.14: Example oscillometric waveform IMFs generated through the EMD algorithm from a case study.

`

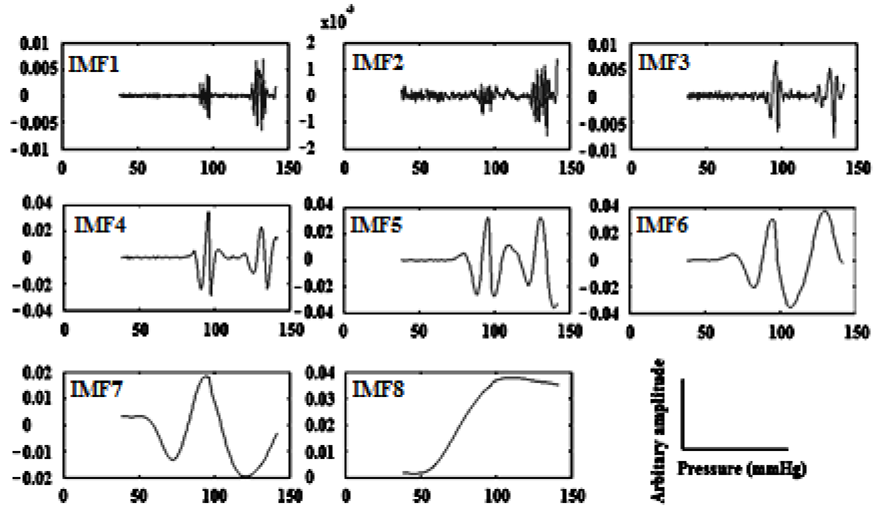

Figure 3.15: Example accelerometer IMFs generated through the EMD algorithm from a case study.

Figure 3.16 illustrates a comparison between pairs of IMFs from a clean OMW and from an OMW that suffers from motion artifacts. From the figure, the first three pairs of IMFs have some similarity, with a correlation factor that reaches an average of about 0.8 between each pair. It can also be noted that the differences between IMF1 in both OMWs are prominent only in regions of artifacts. Pairing the IMFs this way was the starting point used to develop the IMFSA algorithm.

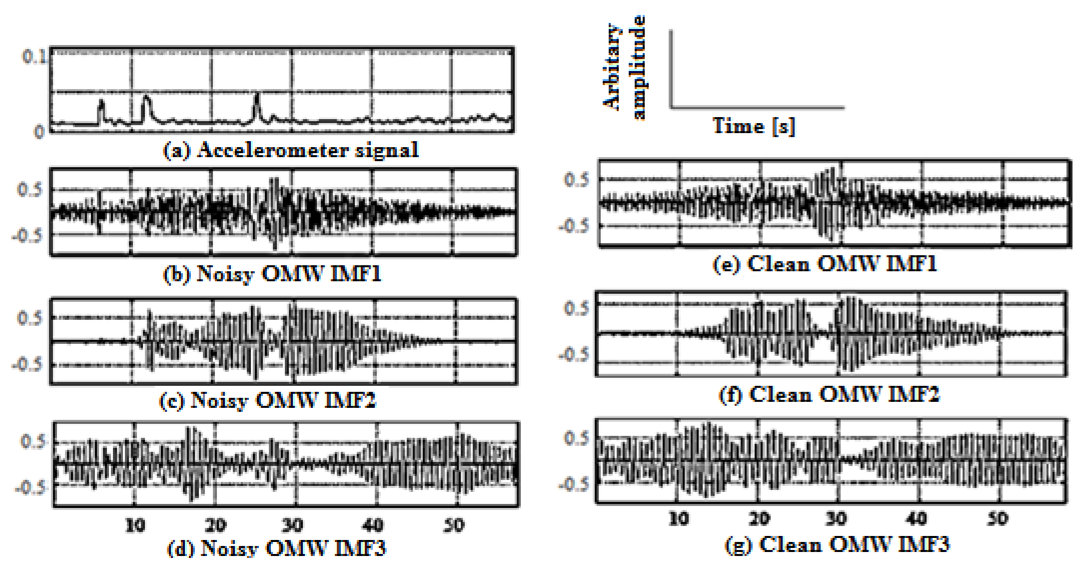

Figure 3.16: A comparison of IMFs in time domain between two OMWs, where one is clean (right) and the other suffers from motion artifacts (left).

`

Furthermore, the Dynamic time warping (DTW) approach was used to demonstrate the similarity between the OMW IMFs of the same order. DTW was run between an IMF from each group and the IMF with the same order from the clean OMW.

The DTW approach allows an elastic shifting of the time axis, which helps accommodating similar sequences, even if they are out of time phase (Mizutani 2006). Figure 3.17 illustrates the difference between a comparison performed using the Euclidean distance and Dynamic time warping.

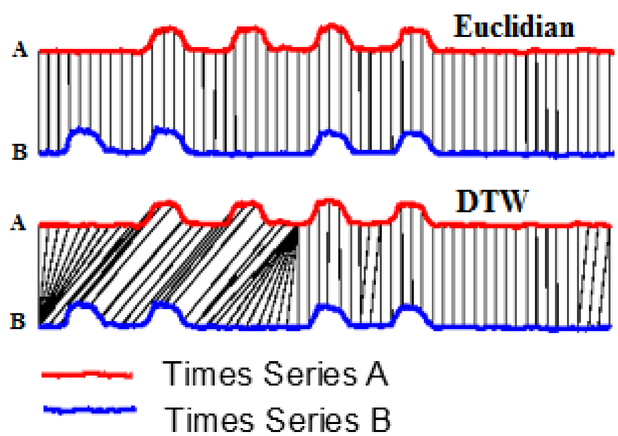

Figure 3.17: A comparison between Euclidean distance (top) and the Dynamic time warping (bottom) algorithms.

From the figure above, it can be seen that although the Euclidean Distance approach is considered a popular approach for defining similarity, it cannot accurately work in cases where the two signals under test are in different time phases. On the other hand, Dynamic time warping approach is more dynamic which makes it a reliable method to follow.

The DTW algorithm computes an approximate weighted geodesic shortest path between different points on each of the two signals under test by adding additional vertices on the edges. This is followed by connecting these points to form straight segments, and then applying Dijkstra's algorithm (Dijkstra 1959) to find the shortest path (Aleksandrov et al. 2000).

`

Dijkstra's algorithm uses the warp path distance, which is calculated using the difference between the two signals. Therefore, the two signals under test are considered identical in intervals where DTW distances are zero. This shortest path is represented by a cost function which appears as a diagonal line, thus the straighter the line, the higher the degree of similarity between the two signals (Salvador and Chan 2007).

Figure 3.18 reflects the results obtained by applying DTW to show the degree of similarity between corresponding pairs of the first three IMFs. The differences usually occur in regions of artifacts. These results show that there is a consistent pattern in the IMFs obtained using the proposed approach, which was the first step towards studying the effect of using each IMF in the algorithm. The straight line shows the shortest time warping distance between the two signals under test.

`

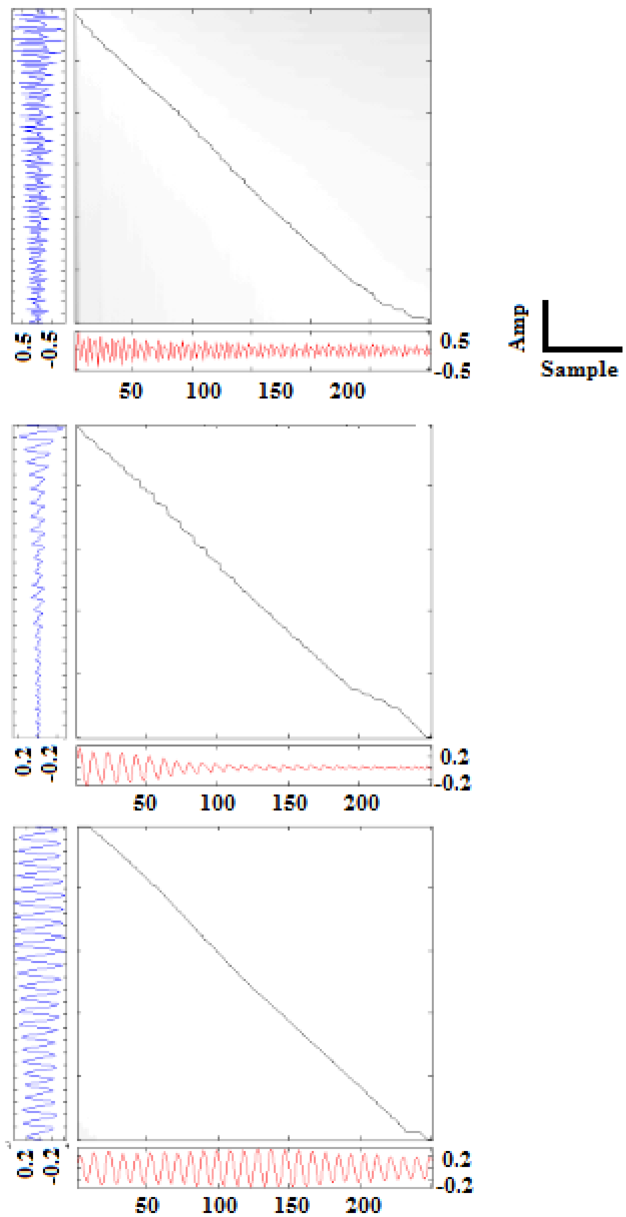

Figure 3.188: Applying the DTW approach on IMFs: 1, 2, and 3 from a noisy OMW and a clean one to demonstrate the similarity through the obtained distance (solid straight line). Top: IMF1, Middle: IMF2 and Bottom: IMF3. The Clean IMF is the vertical signal while the horizontal is the noisy IMF.

`

Another way to explore the effects of artifacts on IMFs extracted from an OMW can be done in the time-frequency domain (Figure 3.19). With the same case study as in Figure 3.16, it can be seen that the time-frequency components are also different mainly in regions of artifacts.

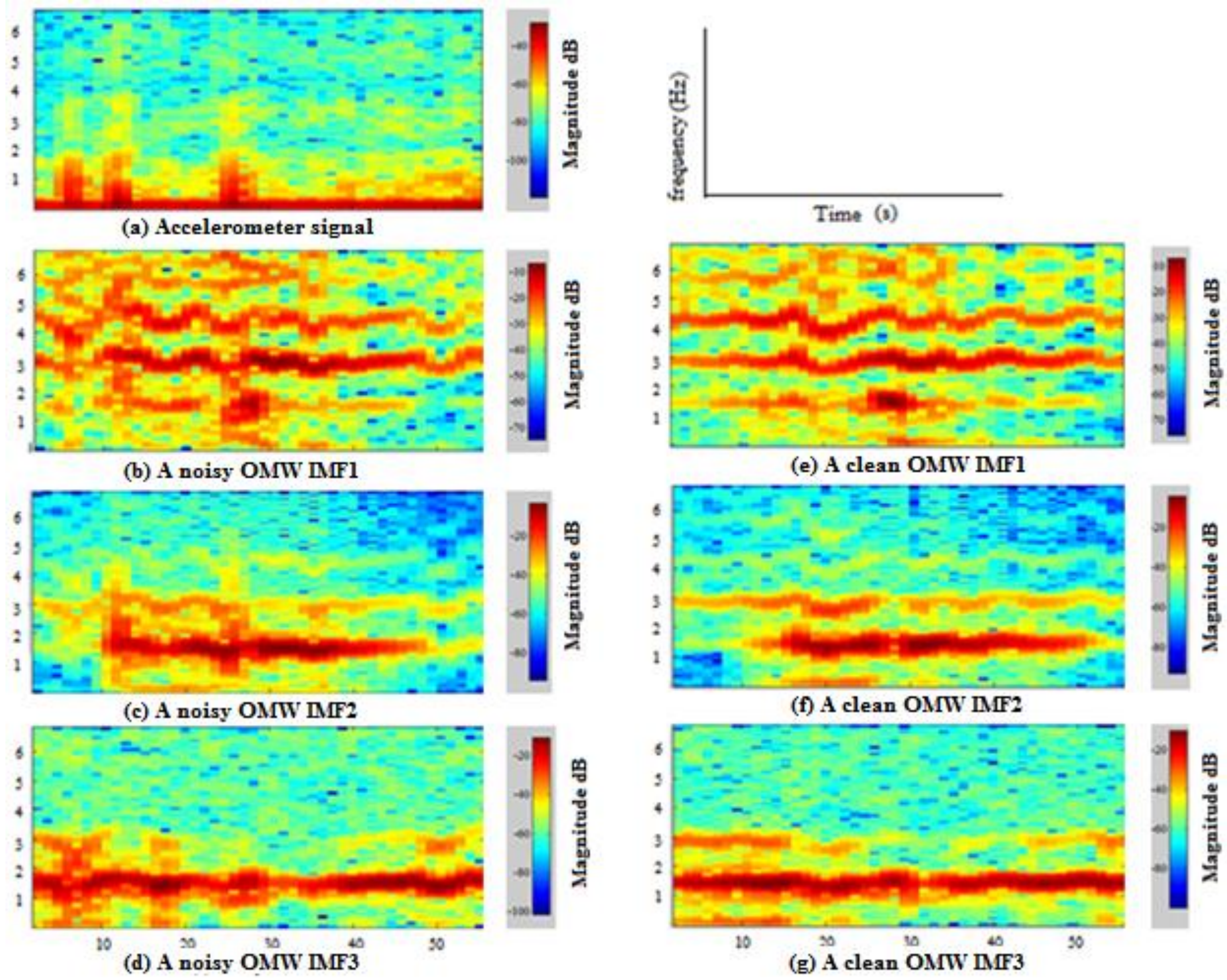

Figure 3.19: A comparison of IMFs in the time-frequency domain between two OMWs, where one is clean (right) and the other suffers from motion artifacts (left).

`

According to Kaslovsky and Meyer (2010), it is possible to divide any noisy signal's IMFs into three main categories, based on time-frequency analysis. These categories are:

- Noise IMFs, where the IMFs consist only of the noise affecting the original signal.
- Transition IMFs, where the IMFs consist of two parts, a noise part and a signal part.
- Monochromatic IMFs, where the IMFs are basically all signal.

In their paper, Kaslovsky and Meyer developed an algorithm to detect artifact events by visually comparing the frequency components and the power levels in all IMFs related to the signal under test. In contrast, the IMFSA algorithm has the advantage that instead of scanning the whole time-frequency plane looking for possible artifact components, it has a precise reference, which is the accelerometer signal. The investigation of artifacts will then take place only in intervals of motion, as pointed out by the accelerometer (Figure 3.20).

`

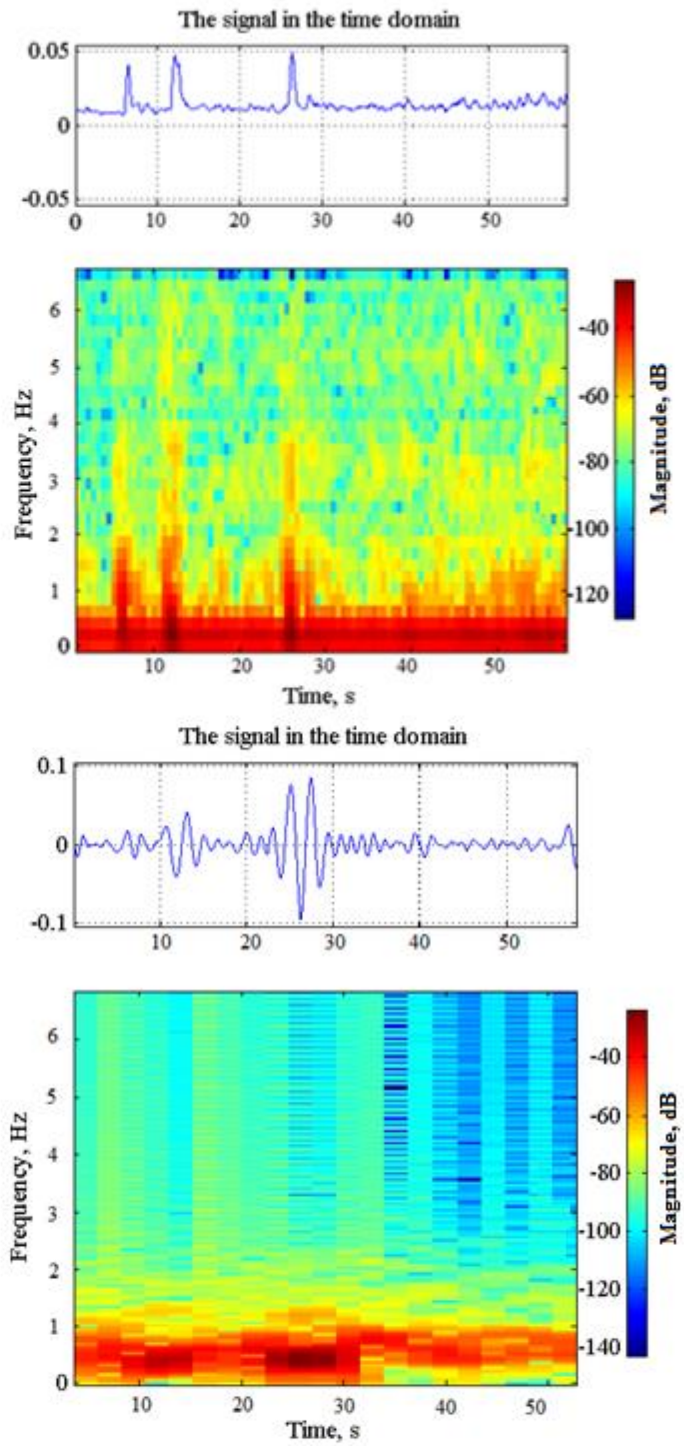

Figure 3.20: Time-frequency analysis of the accelerometer signal (top) and IMF5 from the OMW (bottom). As can be seen, the power in the IMF is higher in the general regions of artifacts.

`

The IMFSA algorithm block diagram is shown in Figure 3.21. From the diagram, it is possible to identify three different sub-blocks; A, B and C. Starting with sub-block A, the EMD algorithm is applied on the two input signals, the accelerometer signal and the oscillometric waveform. In this stage, two selectors work to separate a predefined number of IMFs from both the OMW and the accelerometer signals, as will be explained later in this section. These IMFs were selected based on studying the IMFs from three randomly chosen sets of data (out of the total of 25 sets). By visually comparing the IMFs in both the OMW and the accelerometer signals, we were able to identify the IMFs in the oscillometric signal that include prominent intervals of artifacts.

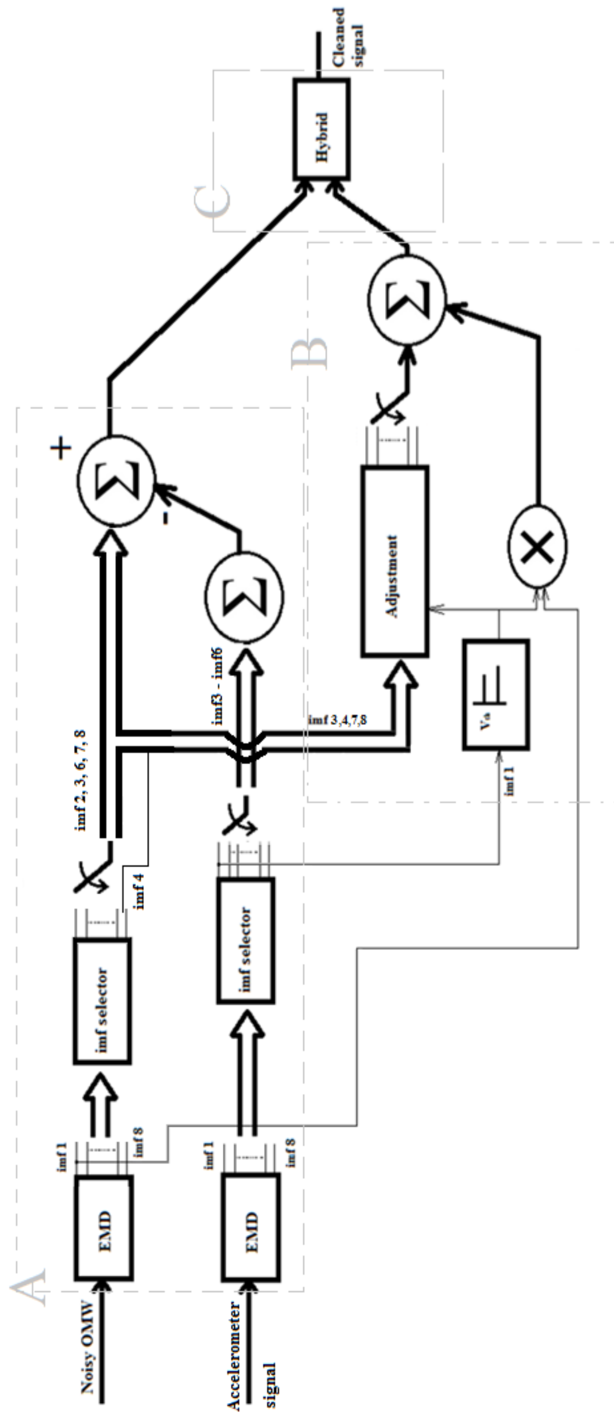

Figure 3.21: Block diagram of the Intrinsic Mode Functions Selective Analyzer (IMFSA).

`

In sub-block A, the three datasets that were chosen were analysed in time-frequency. Studying the IMFs and comparing the regions specified by the accelermometer showed that IMF1 of the OMW has the highest power of artifacts in cmparison with the other IMFs (Figure 3.22). Another conclusion obtained was that IMF5 can be considered as a noise IMF, while IMF4 can be considered as a transition IMF, according to Kaslovsky and Meyer's definition.

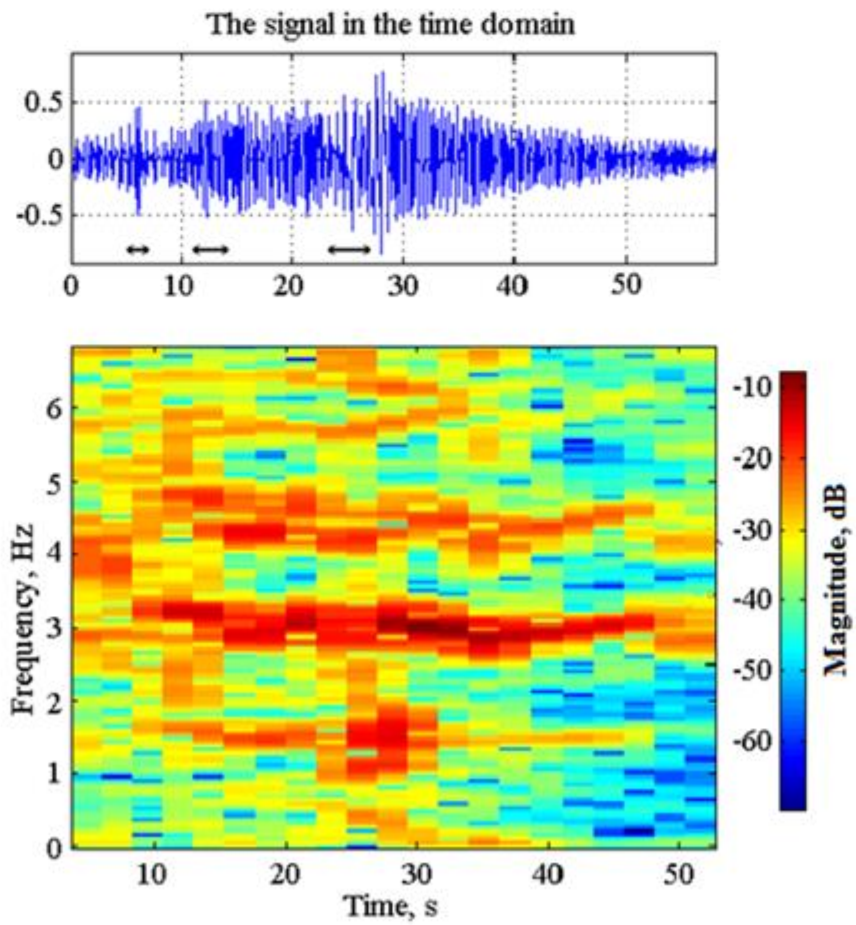

Figure 3.22: Time-frequency analysis of IMF1 obtained from a noisy OMW. It can be seen that intervals of artifacts result in additonal power in the time-frequency plan. Intervals of artifacts in this case are marked by the two headed arrow in the top subplot.

`

The process in sub-block A also includes a subtractor, where the sum of several amplified accelerometer IMFs are subtracted from other oscillometric waveform IMFs. The amplification gain used was 2.The choice of this gain was decided after estimating Mean Absolute Error (MAE) that resulted with different gains from the three randomly selected datasets, as shown in Figure 3.23 below.

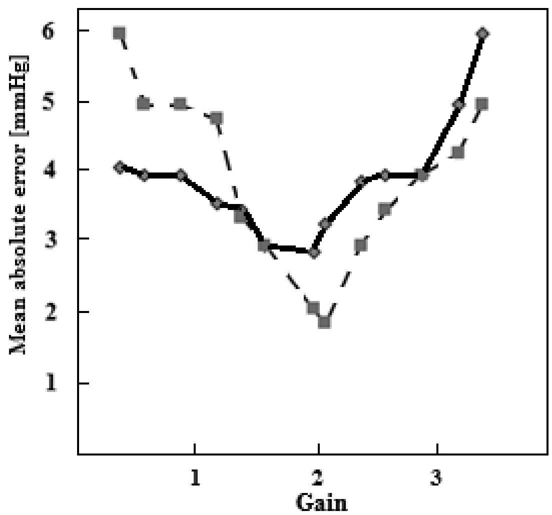

Figure 3.23: Mean absolute error (mmHg) between Omron readings and IMFSA results obtained using different gains from three randomly selected datasets. Dashed line: diastolic blood pressure. Solid line: systolic blood pressure.

As a result, an output signal from this sub-block will be in the form of:

$$\mathrm{Output} = \mathrm{IMF2} + \mathrm{IMF3} + \mathrm{IMF6} + \mathrm{IMF7} + \mathrm{IMF8} - 2 * \mathrm{IMFa3} - 2 * \mathrm{IMFa4} - 2 * \mathrm{IMFa5} - 2 * \mathrm{IMFa6} \quad (3.2)$$

where the IMFi, i Є N are the OMW IMFs, while the IMFs belonging to the accelerometer are written as: IMFai, i Є N.

`

A sample result of what the OMW will look like after passing sub-block A is shown in Figure 3.24.

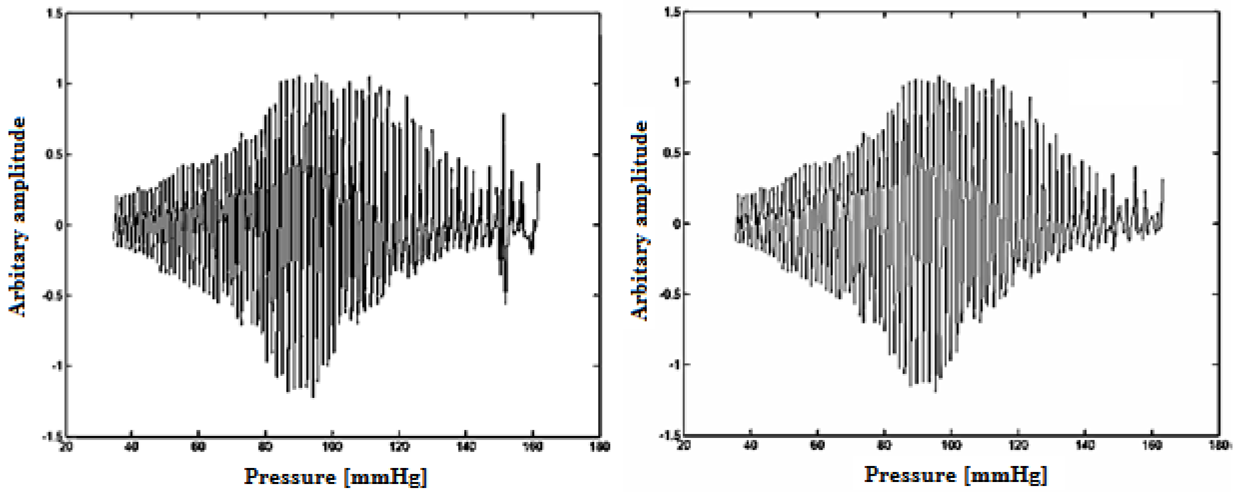

Figure 3.24: Example OMW at the input of sub-block A (Left) and the output of sub-block A in the IMFSA algorithm (Right).

Moving to sub-block B, where an adjustment process takes place, the accelerometer's signal (Figure 3.25) is used by a comparator to generate a square wave representing the intervals of artifact as a high signal and zero elsewhere. This operation will help later in the process of zeroing these intervals in the oscillometric waveform's first IMF (Figure 3.26). The optimal value of the comparator's threshold was chosen to be 0.015 g based on the aforementioned three data sets. Different thresholds were tried and the mean absolute error between Omron blood pressure monitor readings and IMFSA results was calculated (Figure 3.27).

`

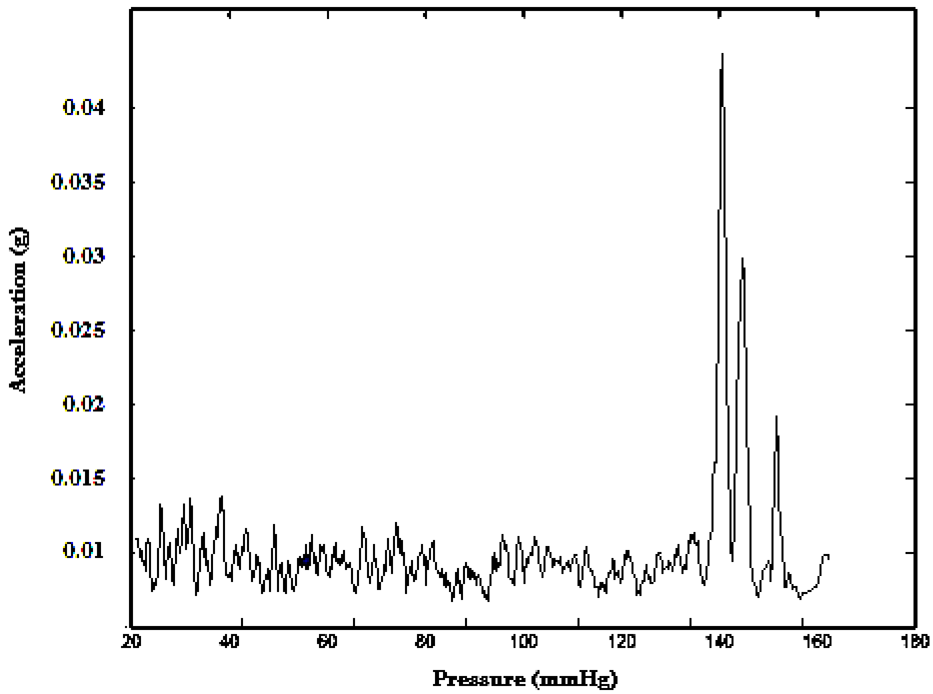

Figure 3.25: Example of a smoothed accelerometer signal obtained in one of the conducted experiments.

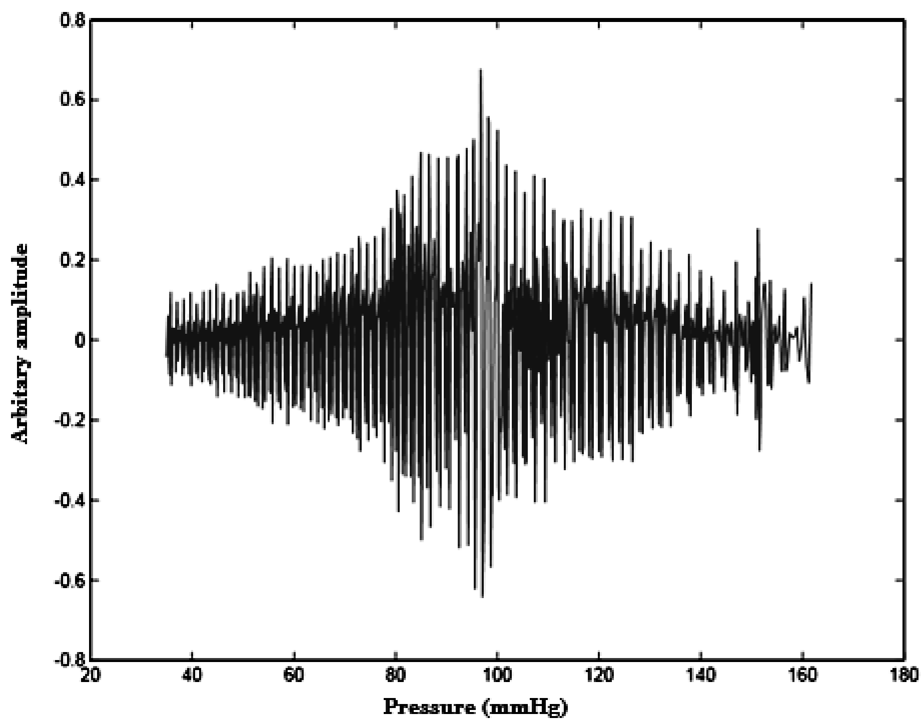

Figure 3.26: Example of an OMW first IMF.

`

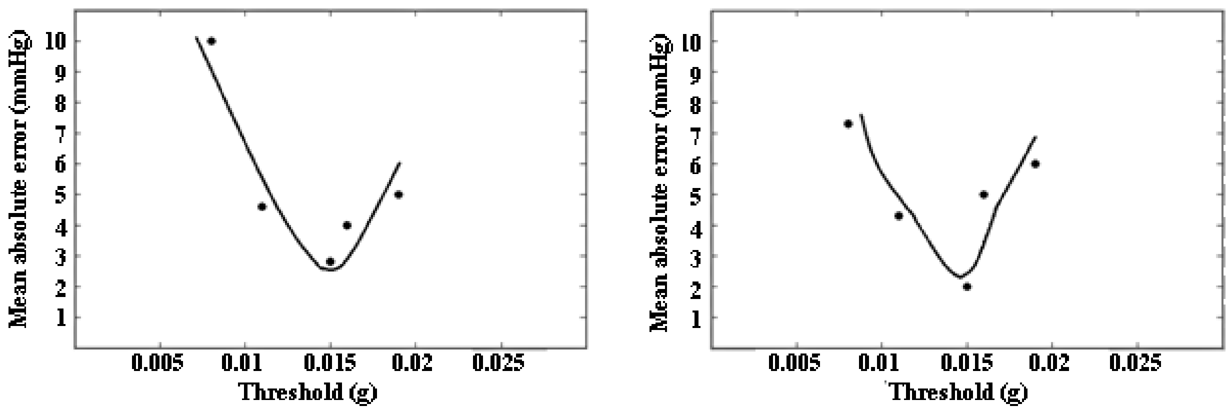

Figure 3.27: Mean absolute error [mmHg] between Omron readings and IMFSA results obtained using different thresholds on three data sets used to optimize the IMFSA algorithm using the gain of 2 that was found according to Figure 2.23. Left: Results with diastolic blood pressure. Right: Results with systolic blood pressure. The continuous line in the graph corresponds to the best fit third order polynomial function.

`

The process of detecting the artifact and zeroing the corresponding intervals in the first OMW IMF is done using the accelerometer signal that defines the interval(s) of artifacts. Figure 3.28 below shows an example of an accelerometer signal before and after passing the comparator stage.

-

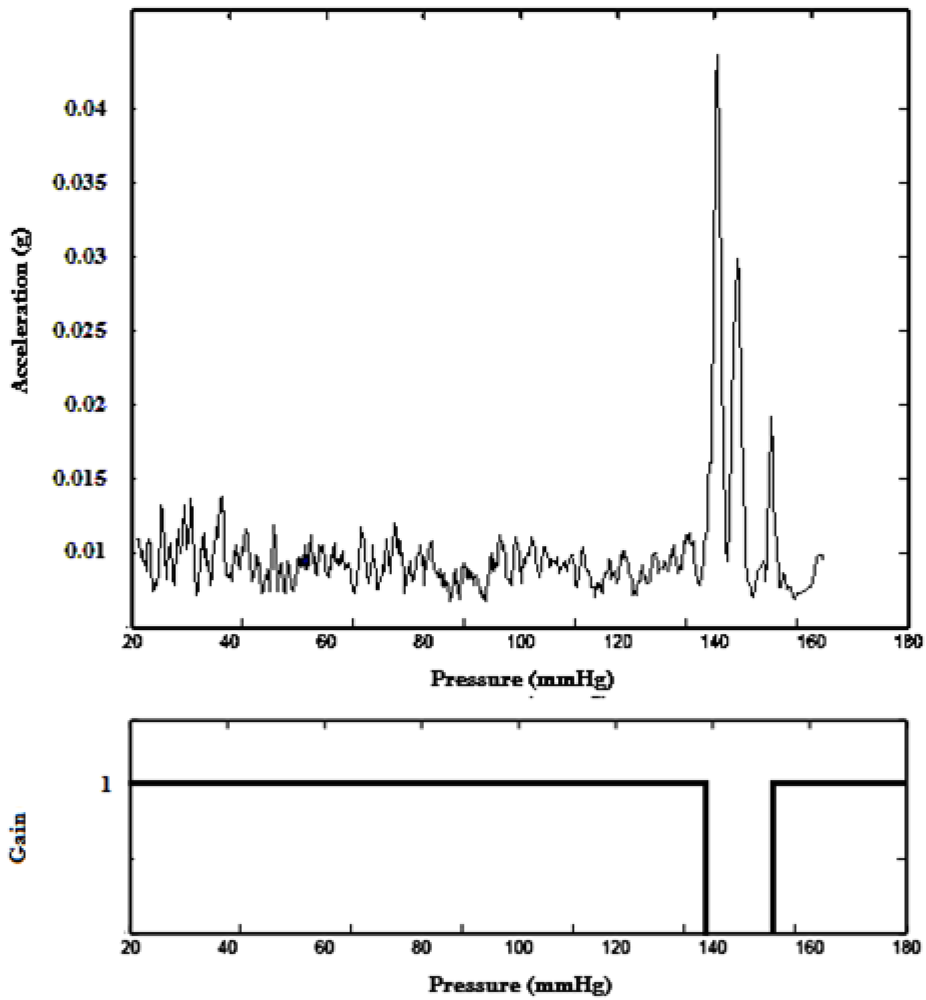

Figure 3.28: The interval of artifact as detected in an accelerometer signal (top) and the square wave representing the output from a Schmitt trigger comparator (bottom).

`

The next step is zeroing all artifact intervals in the OMW IMF1, and an example can be seen in Figure 3.29 below.

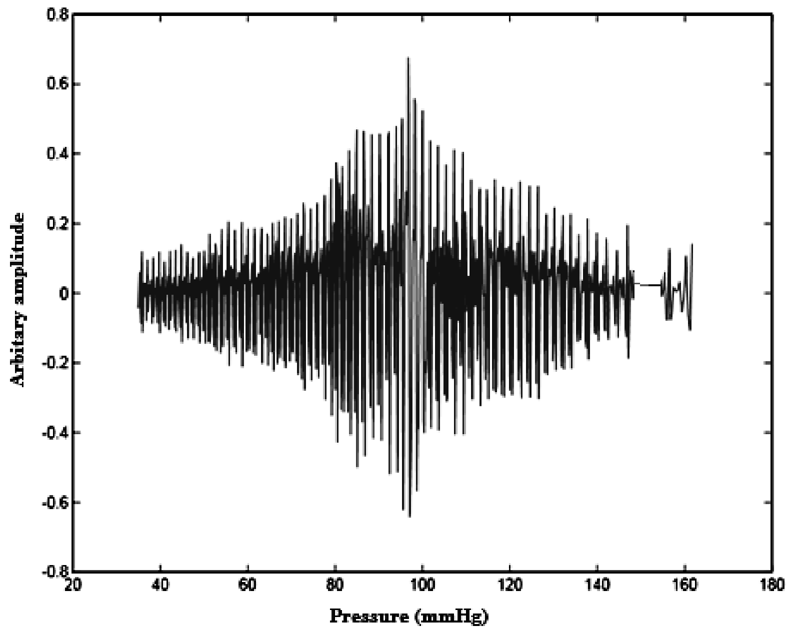

Figure 3.25

Figure 3.29: Results of zeroing artifact region in a sample OMW IMF1.

Another process takes place with the other IMFs to make up for the zero regions that appear in the first IMF signal due to the comparator and zeroing effect. This process includes magnifying only the intervals where IMF1 has been zeroed in IMF3, IMF4, IMF7 and IMF8 as follows:

$$\mathrm{IMF3} = 1 * \mathrm{IMF3} \tag{3.3}$$

$$\mathrm{IMF4} = 2 * \mathrm{IMF4} \tag{3.4}$$

$$\mathrm{IMF7} = 16 * \mathrm{IMF7} \tag{3.5}$$

$$\mathrm{IMF8} = 32 * \mathrm{IMF8} \tag{3.6}$$

The criteria followed in choosing these IMFs are the same as in previous sub-block A, but in addition, IMF4 is also chosen in this part of the algorithm, as IMF4 is considered as a transition IMF, according to the definition set by Kaslovsky and Meyer. Therefore, using it here will ensure the inclusion of some of the signal-related components that are missing from sub-block A in the IMFSA algorithm.

`

The magnifying factors in Equations 3.3– 3.6 are chosen based on the order of the IMF, since in the EMD algorithm, an average of the upper and lower envelopes is performed whenever the next IMF is obtained resulting in an attenuation by a factor of 2 (Huang et al. 1971). The magnifying factors therefore compensate for this successive attenuation. A sample IMF3 before and after magnifying is shown in Figure 3.30 below.

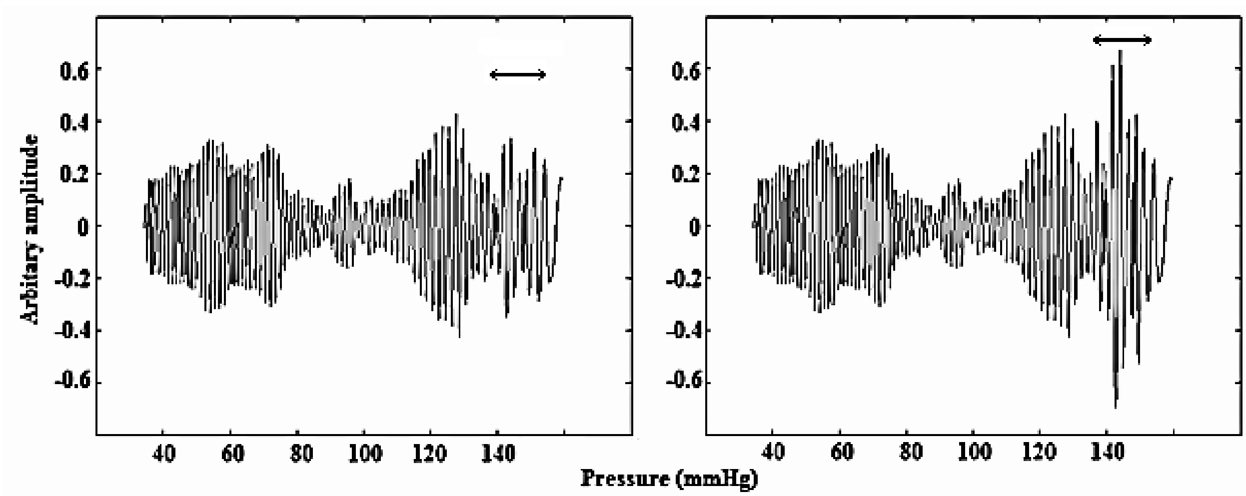

Figure 3.30: A sample oscillometric waveform IMF3 before magnifying the region of interest (left) and after (right).

A sample of what the output from sub-block B looks like is shown in Figure 3.31 below.

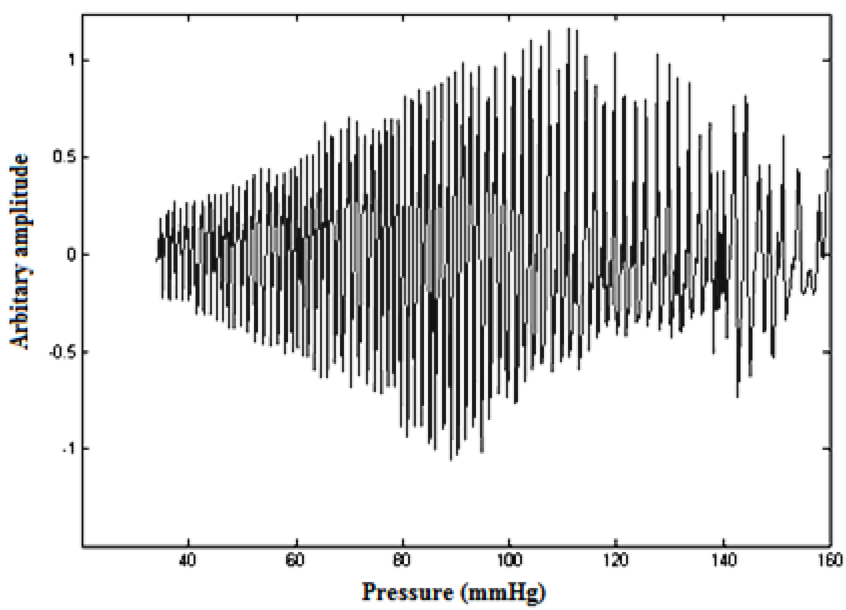

Figure 3.31: A sample signal that results from the process that takes place in sub-block B of Fig. 3.19.

`

Finally, in sub-block C, the outputs from the sub-blocks A and B enter a hybrid function, where a minimum function and an average function are applied. The minimum function compares points from the outputs of sub-blocks A and B and chooses the point-by-point minima, and the average function takes a point-by-point average between the output from sub-block A, sub-block B, and the results from the minimum function.

Figure 3.32 below shows the result of applying the IMFSA algorithm on one of the study cases in comparison with the results obtained with a conventional approach that does not include EMD-based motion artifact suppression.

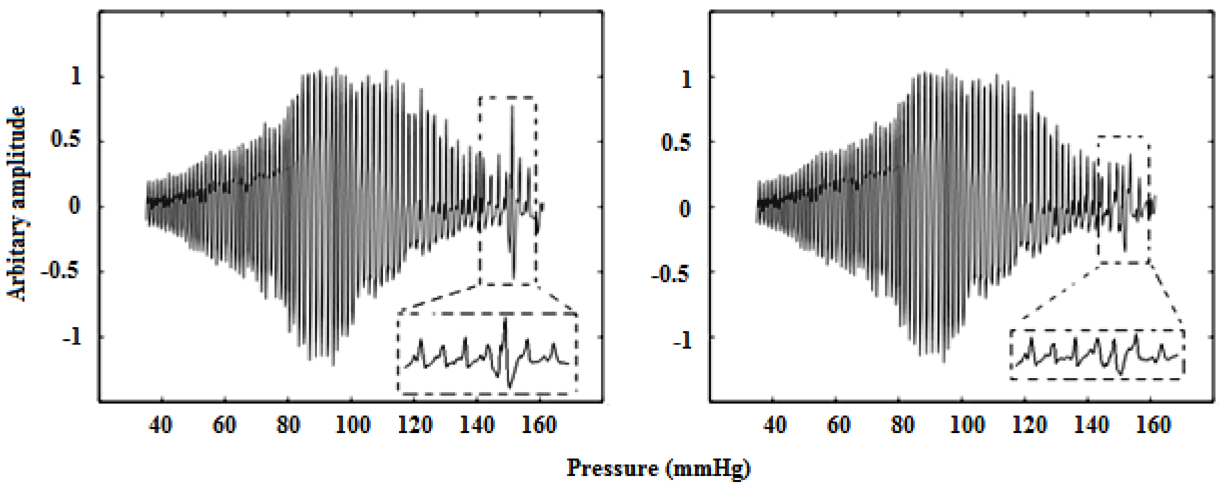

Figure 3.32: Sample case showing the result of the IMFSA algorithm (right) in comparison with the conventional approach that does not include the EMD-based artifact suppression (left).

3.2.4 Intrinsic Mode Functions Collector (IMFC) for vibration artifact rejection

After detecting a periodic vibration signal using the 3-axis accelerometer, the measured OMW is processed using EMD. The determination of the IMFs stops just before the EMD process reaches the vibration signal. After experimenting with two sets of data, it was found that stopping after six IMFs will ensure a good recovery of the signal.

`

The process of recovering the signal, referred to as Intrinsic Mode Functions Collector (IMFC) is therefore performed using the following formula for the output signal y(t):

$$y(t) = \sum_{n=1}^{6}(IMF_n) \qquad (3.7)$$

Figure 3.33 below shows the time-frequency analysis of IMF7 obtained by applying the EMD algorithm on an OMW that suffers from vibrations. As shown in the time-frequency plot, there is a clear indication of a periodic signal.

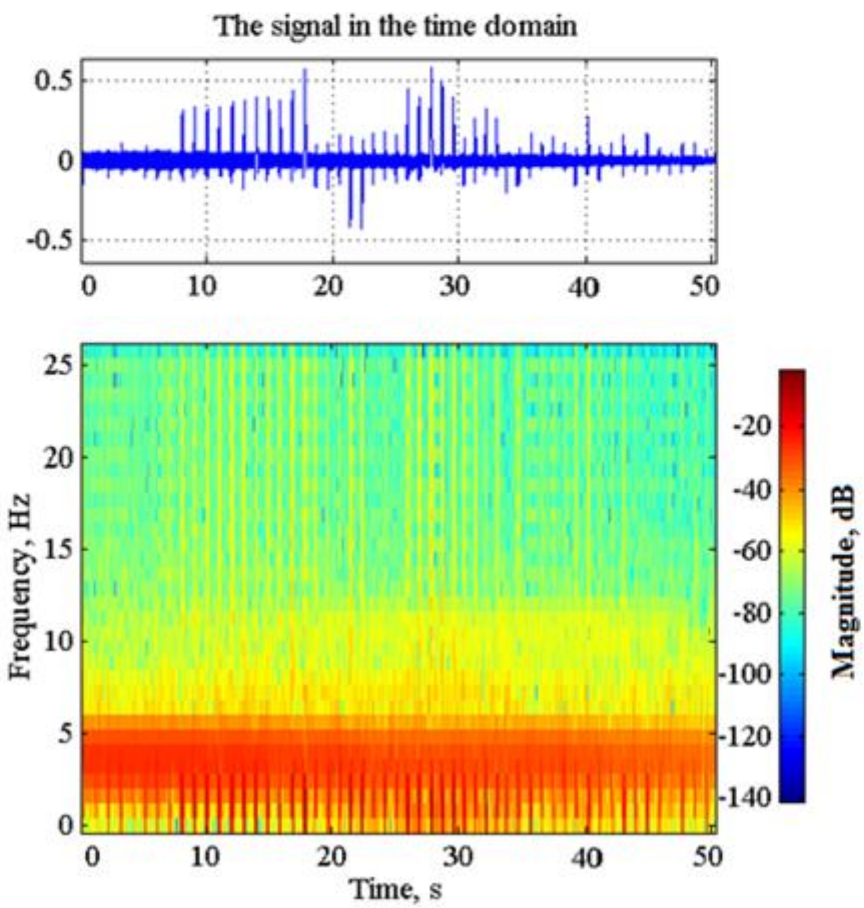

Figure 3.33: Time frequency analysis of IMF 7 in an OMW that suffers from vibration motion artifacts

\`

By ruling out IMFs considered as noise IMFs in OMWs contaminated by vibration, the useful components of the OMW are retained. Figure 3.34 shows an example of vibration artifacts superimposed on the oscillometric waveform and the effect of the cleaning process using the IMFC algorithm.

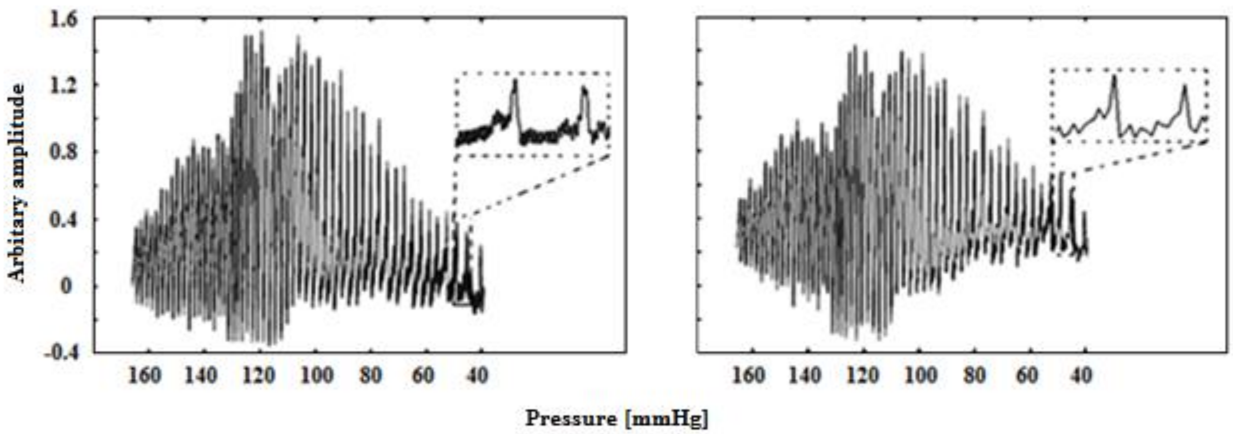

Figure 3.34: A comparison between the OMW that is corrupted by a vibration signal (left) and after cleaning by the proposed IMFC algorithm (right).

3.2.5 Performance measures

In order to evaluate the obtained performance, the following measures were calculated: the mean error (ME), the standard deviation of error (SDE), and the mean absolute error (MAE).ME reflects the degree of bias in the estimates, SDE represents the degree of spread of the errors, while the MAE represents the overall accuracy (ANSI/AAMI/ISO 81060-2, 2009). These quantities are mathematically defined as:

$$\text{MAE} = \frac{1}{n} \sum_{i=1}^{n} |f_i - y_i| \quad (3.8)$$

$$\text{ME} = \frac{1}{n} \sum_{i=1}^{n} (f_i - y_i) \quad (3.9)$$

$$\text{SDE} = \left(\frac{1}{n} \sum_{i=1}^{n} (f_i - y_i - ME)^2\right)^{0.5} \quad (3.10)$$

where, f_i is the measurement under test, while y_i is the reference measurement.

`

Note that, according to the ANSI/AAMI/ISO standard, a clinically acceptable non-invasive BP measurement device requires an SDE equal or less than 8 mmHg and an ME equal or less than ±5 mmHg.

3.2.6 Blood pressure estimation algorithm

In the experimental measurements, blood pressure estimation was done using the oscillometric method, which was described in Chapter 2. We augment the standard oscillometric method by recording an ECG signal that is synchronized with the pressure signal to help generate the required envelope. A ratio-based algorithm was applied to detect both the systolic and the diastolic blood pressure values (refer to Figure 2.2).

The cuff pressure at which the maximum amplitude oscillation occurs is determined as the MAP. The cuff pressure at which the amplitude of the oscillations reaches the systolic ratio r_s of the maximum amplitude A is determined as the SBP, while the cuff pressure at which the amplitude of oscillations falls down to the diastolic ratio r_d of the maximum amplitude A is determined as the DBP (Chen 2010; Forouzanfar 2014).Estimating the systolic ratio r_s and the diastolic ratio r_d was done by comparing a clean oscillometric signal with our reference measurement (using the Omron blood pressure monitor).The range for r_s varied from 45-73% of the maximum value represented by the MAP, while r_d varied from 69-83% of the MAP (Figure 2.2).

The algorithm is summarized in the following steps:

1- Collect synchronized ECG and CP (cuff pressure) signals.

2- Detect the R-wave in the ECG by running a peak detection algorithm.

3- Implement a linear interpolation algorithm between the CP signal and the R-peaks detected in Step2 to generate a trend line for the CP signal.

4- Subtract the CP trend line from the CP signal to obtain the corresponding OMW (oscillometric wave).

5- Find all the peaks and troughs in the OMW.

`

6- Find the OMW envelope by subtracting the peaks from the troughs

7- Apply the ratio algorithm to identify to estimate SBP and DBP with respect to the MAP, which is the global maximum in the envelope signal.

It should be noted that the both the proposed EMD-based approaches, and the conventional method to which it was compared, used the same steps described above to estimate SBP and DBP. The only difference between the proposed and conventional approaches is that the EMD-based approaches involve an initial stage to suppress the motion artifact in the OMW prior to further analysis. Moreover, with both approaches, the ratios were determined based on the Omron measurement, which allows performing a comparison between the performance of the two methods relative to the same reference measurement.

3.3 Experimental results

3.3.1 Vibration artifact rejection

The effect of vibrations is to disturb the signal, often resulting in a shifted envelope. The performance of the proposed EMD-based IMFC algorithm was tested on the whole dataset. The results obtained with the proposed algorithm were compared with the corresponding results obtained using the same oscillometric algorithm, but with no artifact suppression. The comparison of the performance of the two methods was done using Bland-Altman analysis with respect to the reference measurement obtained using the Omron device (Altman and Bland 1983; Bland and Altman 1986).

Bland-Altman analysis is considered an excellent tool to investigate the agreement between results obtained using a method under test and a reference method. In a Bland-Altman plot, the y-axis represents the difference between the readings, while the x-axis represents the average. Figures 3.35 and 3.36 below show the Bland-Altman plots for SBP (systolic blood pressure) and DBP (diastolic blood pressure), respectively, for the proposed algorithm using IMFC and for the same oscillometric method with no EMD-based analysis. On both graphs, the bias (ME) and the limits of agreement (ME ± 1.96 × SDE) are shown as continuous and dashed lines, respectively.

`

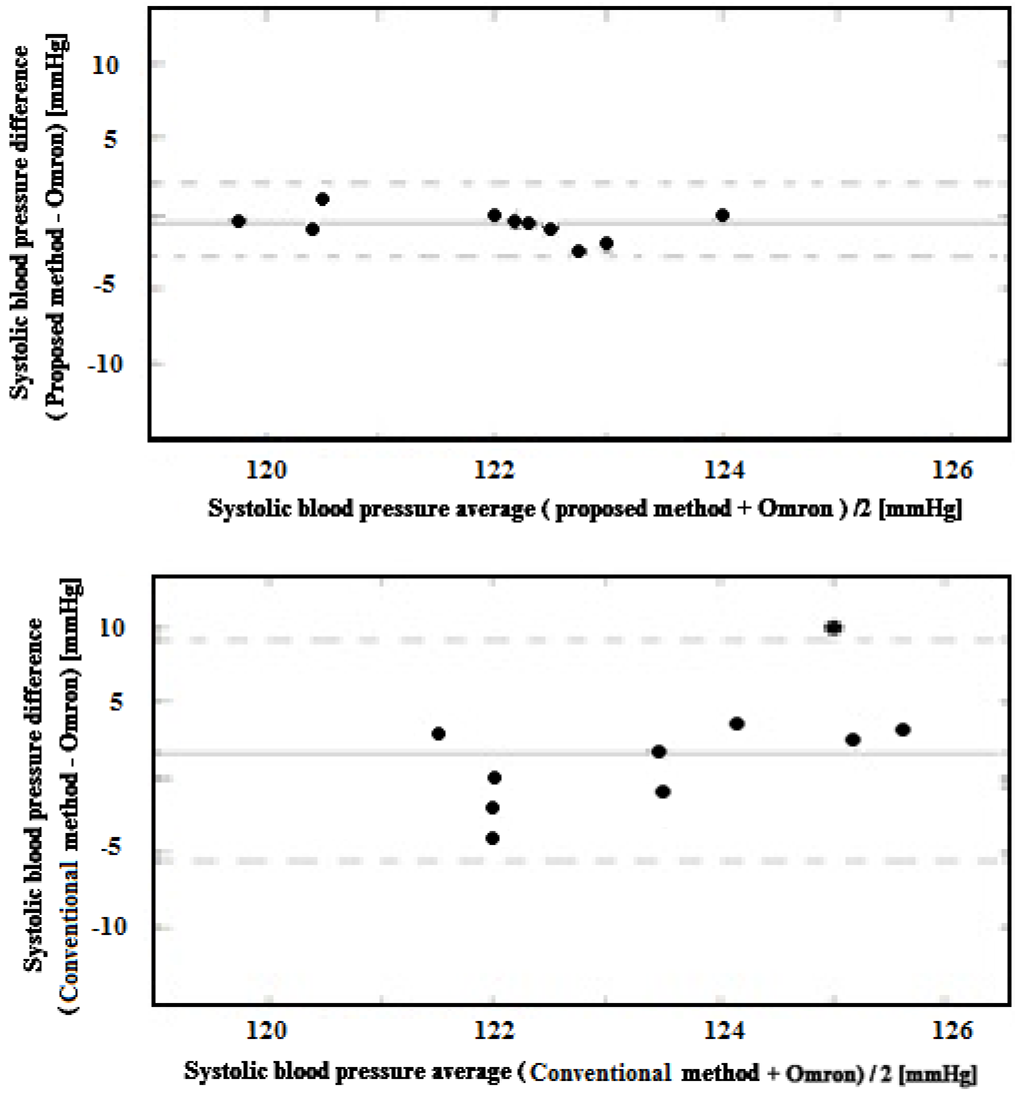

Figure 3.35: Bland-Altman plot of the systolic blood pressure estimation with vibration artifacts based on five subjects with two tests each. Top plot is for the proposed method and bottom plot is for the conventional method. Horizontal dashed lines show limits of agreement, while the continuous central line shows the bias.

`

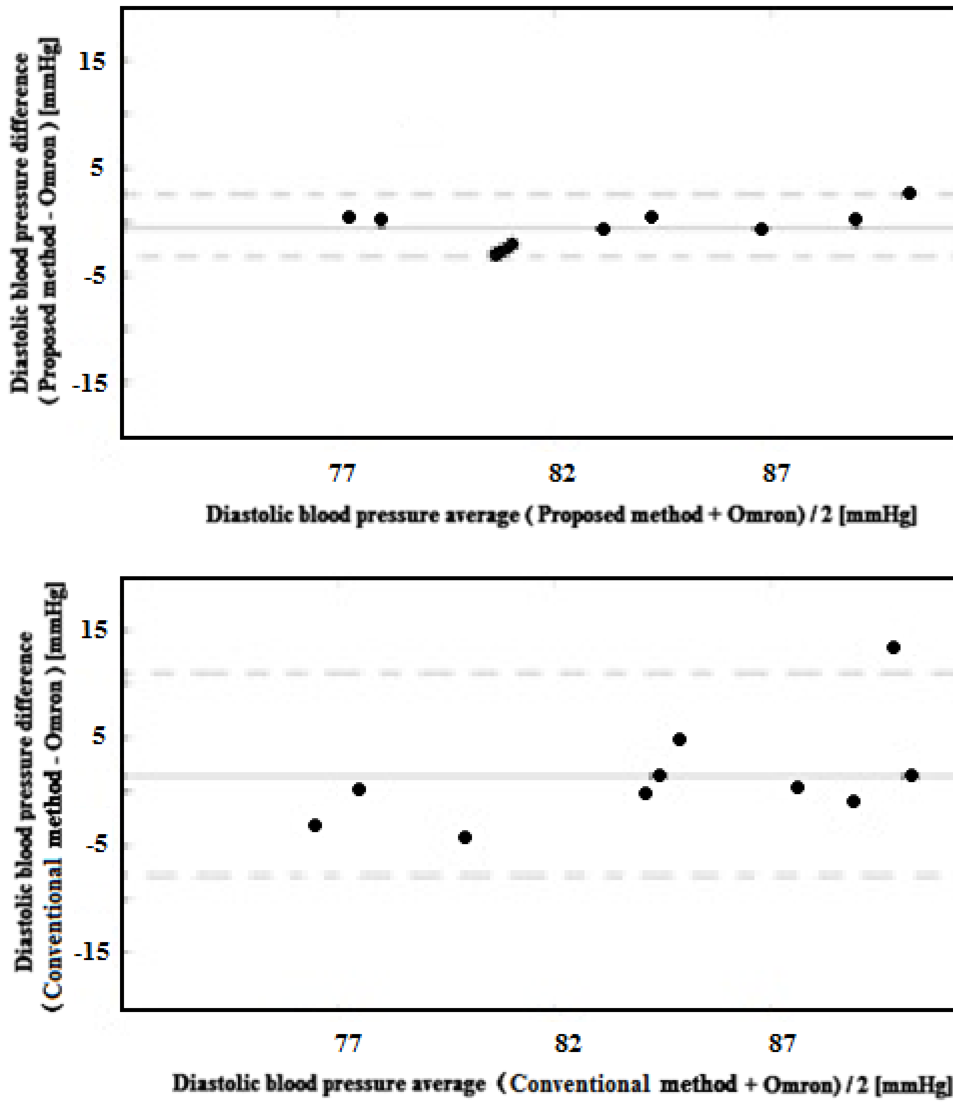

Figure 3.36: Bland-Altman plot of the diastolic blood pressure estimation with vibration artifacts based on five subjects with two tests each. Top plot is for the proposed method and bottom plot is for the conventional method. Horizontal dashed lines show limits of agreement, while the continuous central line shows the bias.

It is seen that using the proposed algorithm (IMFC), the estimation is in closer agreement with the one made by the Omron device, compared with the estimation obtained with the same oscillometric method but without suppression of the artifact due to vibration, as the limits of agreement obtained with the proposed approach are narrower.

`

Table 3.2 shows the overall performance of the two approaches using mean error (ME), standard deviation of error (SDE), and mean absolute error (MAE). As can be seen, with the proposed method, all the error measures were reduced for both SBP and DBP. In particular, the SDE, which is commonly used in evaluating the accuracy of non-invasive blood pressure estimation methods (ANSI/AAMI/ISO 81060-2, 2009), shows a reduction of 4 mmHg in the case of DBP and 2.8 mmHg in the case of SBP.

Table 3.2: Overall performance obtained with the estimation of systolic and diastolic pressure before and after suppression of the artifacts due to vibration using the proposed method (based on a dataset of 10 recordings from 5 subjects).

Measure	**Pre-suppression**		**Post-suppression**	
	SBP	DBP	SBP	DBP
Mean error [mmHg]	1.7	1.9	-0.6	-0.4
Mean absolute error [mmHg]	3.1	3.5	0.8	1.1
Standard deviation of error [mmHg]	3.8	5.5	1.0	1.5

3.3.2 Transient motion artifact rejection

To investigate the performance of the proposed IMFSA approach, results obtained with it were compared with those obtained using the conventional approach that does not incorporate EMD-based analysis. Typically, the effect of applying the EMD-based approach modifies the envelope by returning the slope of the affected region to an acceptable level. Figure 3.37 shows one example of applying the IMFSA on the oscillometric waveform envelope (OMWE) and the corresponding envelope obtained with the conventional approach.

`

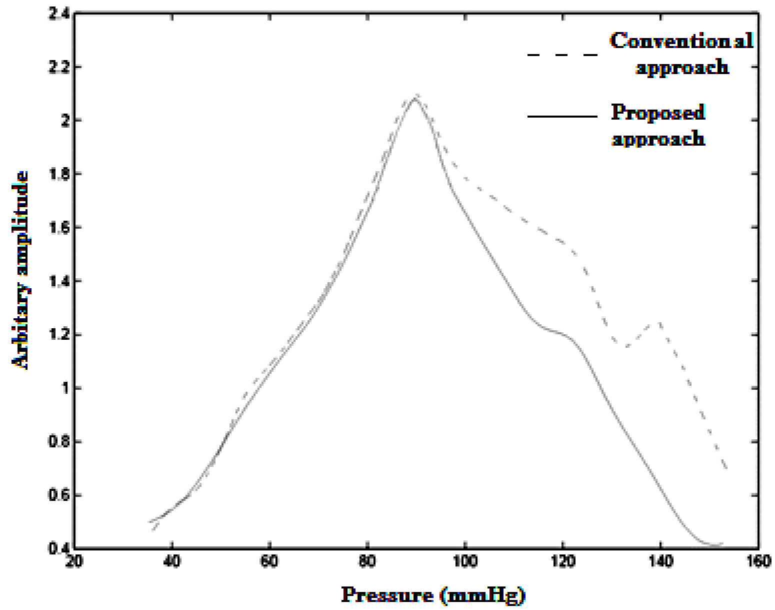

Figure 3.37: An example OMWE obtained by the IMFSA approach (continuous line) and the envelope obtained by the conventional approach (dashed line).

Another method to investigate further the frequency composition of the signal before and after recovery is the Short-time Fourier transform (STFT). This is shown in Figure 3.38, where it was estimated over non-overlapping windows of approximately 5 sec duration each. From the figure, it can be seen that the power of the signal in the period of artifacts was successfully reduced after applying the IMFSA algorithm.

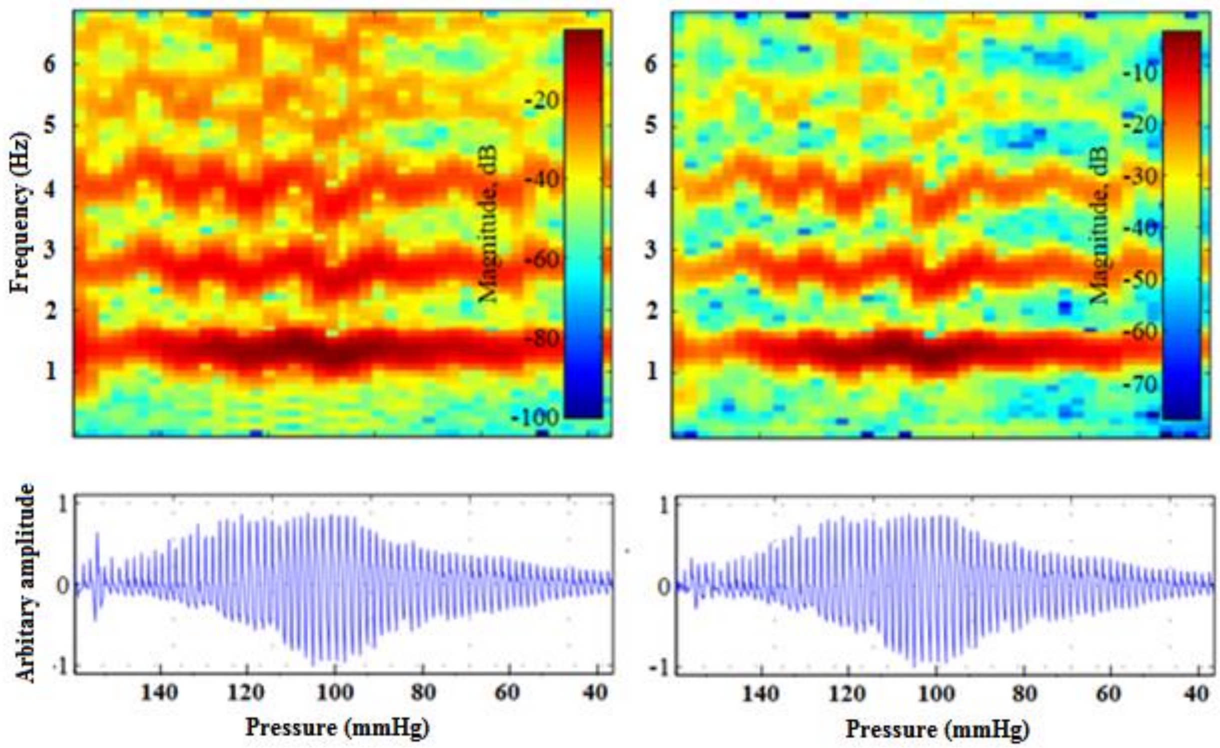

Figure 3.38: An example of the Short-time Fourier Transform, of the OMW obtained with window durations of approximately 5 sec before applying the IMFSA (top left) and after applying it (top right), and the corresponding time-domain signals (bottom).

Bland-Altman plots were used to compare the performance of the IMFSA algorithm with that of the conventional algorithm, with the Omron monitor serving as the reference method in both cases. Figure 3.39 shows the case of SBP, while Figure 3.40 shows the same comparison, but with DBP.

Compared to the reference measurements, it can be observed that the limits of agreement (LOA) of the IMFSA method are considerably narrower than those of the conventional method, for both SBP and DBP. Moreover, the conventional approach errors appear to be proportional to the magnitude of measurement, at least for SBP, unlike the errors obtained with the IMFSA algorithm.

`

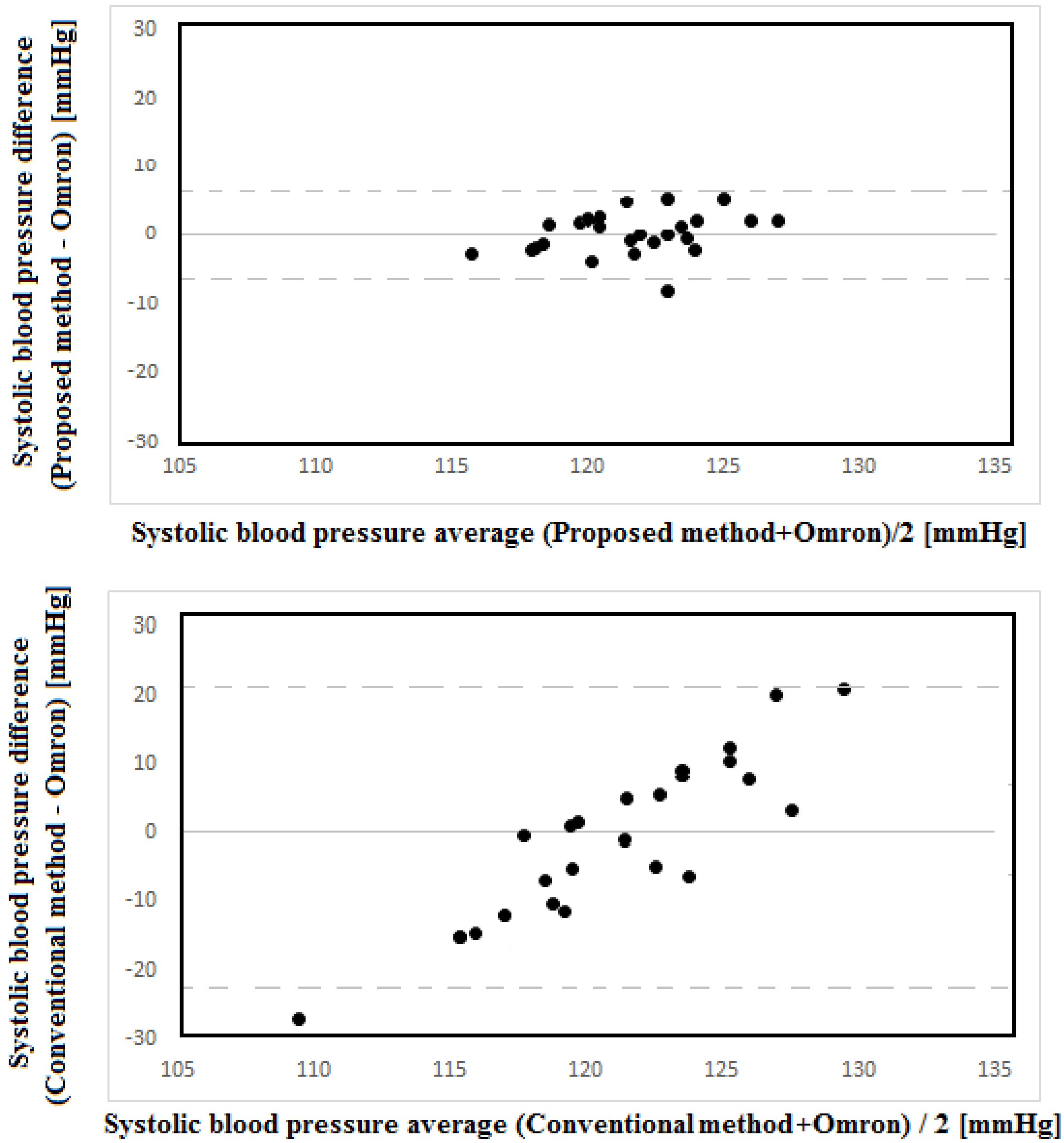

Figure 3.39: Bland-Altman plot of the systolic blood pressure estimation with transient motion artifacts based on five different subjects. Top plot is for the proposed IMFSA method and bottom plot is for the conventional method. Horizontal dashed lines show limits of agreement, while the central continuous line shows the bias.

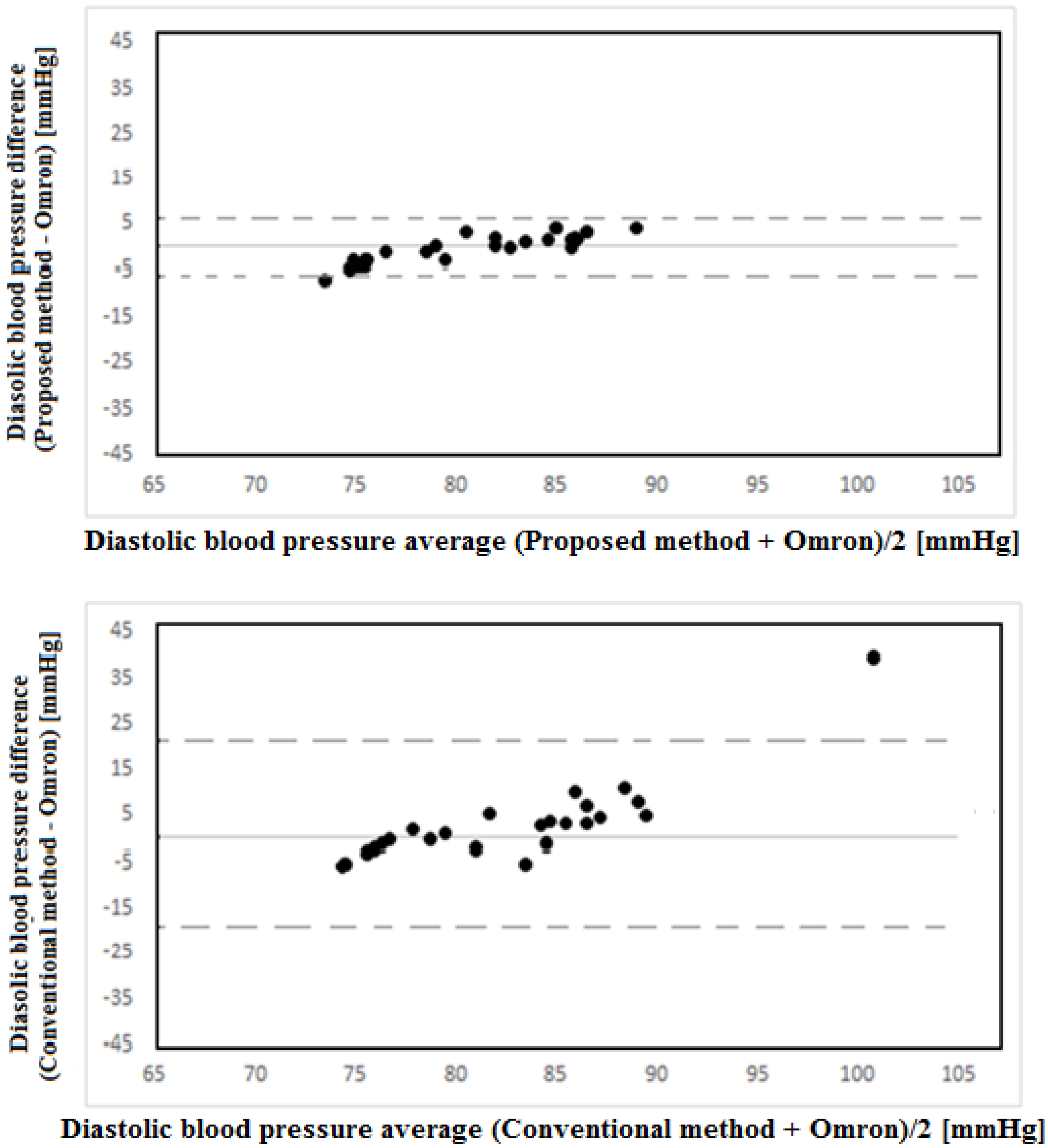

Figure 3.40: Bland-Altman plot of the diastolic blood pressure estimation with transient motion artifacts based on five different subjects. Top plot is for the proposed IMFSA method and bottom plot is for the conventional method. Horizontal dashed lines show limits of agreement, while the central continuous line shows the bias.

`

Table 3.3 below shows the overall performance before and after suppression of the transient motion artifacts based on IMFSA in terms of mean error (ME), mean absolute error (MAE), and standard deviation of error (SDE) with the entire dataset. The results show that IMFSA method for suppressing transient motion artifacts provides accurate estimates of systolic and diastolic pressure. In particular, before artifact suppression, the SDE exceeds the 8 mmHg limit set by the ANSI/AAMI/ISO 81060-2 (2009) standard. After artifact suppression, the SDE is reduced to a level well below the 8 mmHg limit, for both SBP and DBP.

Table 3.3: Overall performance obtained with the estimation of systolic and diastolic pressure before and after suppression of the artifacts due to transient motion artifacts using the proposed IMFSA method (based on a dataset of 25 recordings from 5 subjects).

Measure	**Pre-suppression**		**Post-suppression**	
	SBP	DBP	SBP	DBP
Mean error [mmHg]	-0.9	3.2	0.3	0.0
Mean absolute error[mmHg]	9.4	5.3	2.4	2.4
Standard deviation of error [mmHg]	11.6	8.7	3.1	2.9

Table 3.4 below displays the results obtained with another set of blood pressure measurements with different types of transient motion artifacts and only using a commercial blood pressure monitor (the Omron device). The experiment was conducted on one subject. The motion artifacts included in the study were: arm motion while the hand is fixed, finger clicking, and arm shakes.

The effects of these motion artifacts are indicated and the results are compared with a reference measurement obtained immediately after, using the same device but without any movement by the subject. In the table, “E” represents an error code displayed by the device which indicates a failure of the measurement. Note the frequent failure of the measurements with the motion artifacts, and that, in other cases, an estimation of blood pressure will actually take place, but the presence of motion artifact results in very high errors.

Table 3.4: Results obtained in the presence of different transient motion artifacts in comparison with a reference measurement, with both measurements performed using an Omron blood pressure monitor. “E” is an error code displayed by the device indicating a failure of the measurement.

Test number	Description	With Motion Artifacts		Reference (without motion artifacts)	
		SBP [mmHg]	DBP [mmHg]	SBP [mmHg]	DBP [mmHg]
1	Elbow up, once	E		120	80
2	Elbow up, once	E		116	77
3	Elbow up, twice	E		118	74
4	Elbow up, three times	142	81	123	85
5	Fingers tapping	125	83	125	79
6	Fingers tapping	145	78	126	81
7	Fingers tapping	E		122	86
8	Arm shakes	123	93	117	81
9	Arm shakes	E		126	88
10	Arm shakes	E		124	79

3.4 Discussion and Conclusions

As discussed in the literature, an increase of even 3 mmHg to 4 mmHg in a blood pressure should be considered clinically significant. According to a study based on a 1 million-patient meta-analysis shows that an increase in the systolic blood pressure of about 3-4 mmHg could translate into 20% stroke mortality from ischemic heart disease (Prospective Studies Collaboration 2002). As a result, it is important to achieve high accuracy in blood pressure measurement.

Obtaining an accurate non-invasive blood pressure estimation can be challenging. Vibration is one of the factors that can negatively affect blood pressure measurement when it takes place in a moving vehicle such as an ambulance. The proposed EMD-based IMFC algorithm shows the ability to suppress artifacts due to vibrations and provide more accurate estimates of blood pressure in comparison with the conventional method.

Another challenge that was addressed in this chapter is the suppression of transient artifacts due to motion. Commercially available blood pressure monitors may completely fail to give a reading when such artifacts occur. Different artifacts were introduced during measurements, and analysis based on the proposed EMD-based IMFSA algorithm were made. The ability to locate artifact events accurately using the concurrently recorded accelerometer signal was the key to enable artifact suppression. The high correlation between the accelerometer signal and the pressure signal in the intervals of artifacts supports the choice of using the accelerometer signal for this purpose. The proposed algorithm considerably improved the accuracy of the blood pressure estimates in comparison with the commonly-used conventional algorithm, and allowed the estimates to be well within the requirements of the ANSI/AAMI/ISO standard.

`

As has been discussed in the literature review in Chapter 2, this area of research is still fertile and it is hardly discussed by any journal papers. Most of the oscillometric based blood pressure measurement experiments emphasize the importance of keeping the patient (or the person under test) calm during the measurements to eliminate any chance of an erroneous estimation (Sorvoja and Myllylä, 2005). Moreover, there has been little effort to distinguish between the two common types of motion artifacts, namely vibrations and transient motion artifacts. Usually the term is used for both types and the suggested methods are somehow claimed to work on both (Koo et al. 2007).

Most of the research done in this area is reported either in the form of conference papers or patents, which usually do not contain sufficiently informative descriptions as would be found in journal papers. Usually when accuracy is described, it is reported as an overall accuracy with a single number. Some patents have proposed synchronizing the cuff pressure and the ECG signals to discard unwanted signals, given that between any two ECG R-peaks, there has to be a pressure pulse, at least when the heart rhythm is normal. The analysis is done by applying a global maximum scan for peaks between each two ECG R-peaks. One example is the Smartcuf^{TM} introduced by Gibson et al (2008). Although this approach is in theory appropriate, applying it would suggest working with a clean cuff pressure signal, where pressure pulses are clear. Figure 3.41 below shows a case study of the effect of having motion artifacts during a blood pressure measurement. From the figure, it is clear that the detection of the peaks in the OMW would not be accurate if we depend on the ECG R-peaks. Therefore, this can result in an erroneous estimation of blood pressure.

`

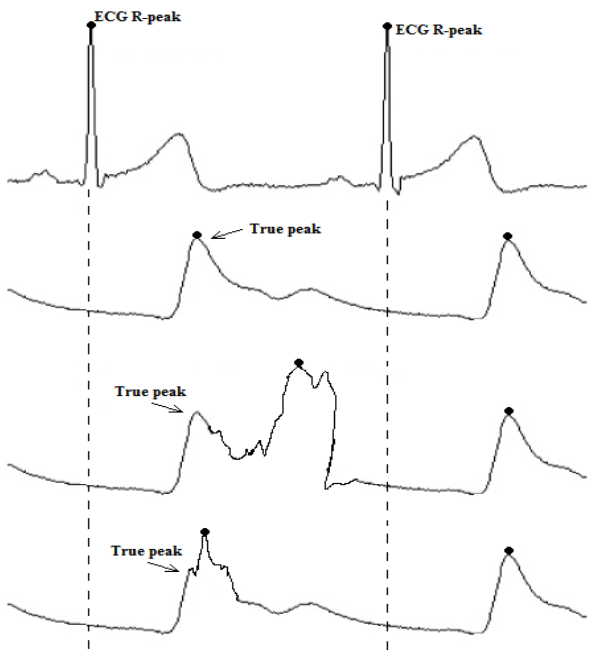

Figure 3.41: A case study showing the effect of motion artifact on pressure pulse peak detection. Top: ECG signal. Second row: a clean cuff pressure signal acting as a reference. Third row: an artifact signal contaminating the true pressure pulse. Bottom: Another example showing both the pressure pulse and the artifact signal merged into a one pulse. The circles indicate results of running a peak detection algorithm.

A PhD thesis introduced a method based on the use of a biosignal reference, in the form of Korotkoff sounds to detect events of artifacts (Abdul Suko et al. 2012). One problem here is that this type of biosignal reference will add more complexity to the system and make it harder to use, particularly by untrained home users.

Another PhD thesis from the University of Florida (Thakkar 2005) simulated the blood pressure pulse waveform as a periodic signal and added simulated Gaussian noise. From the graphs included in the thesis, the blood pressure signal was based on a purely sinusoidal signal, and did not include features or variations of real pulse waveforms. The noise cancellation stage in the proposed algorithm was a comb digital filter, which is an excellent choice when dealing with periodic signals. The problem in this technique is that the blood pressure pulse signal is not a perfectly periodic signal.

`

A conference paper by Usuda et al. (2010) developed a technique where a monitor system can stop the cuff deflation in the event of motion artifacts to prevent including them in the calculations later. However, few details about the technique were provided. One problem in this technique is the slowness of the time response of the monitoring system in events of artifacts. Another likely problem is the number of artifacts that such a system can handle. A similar technique may be already incorporated in currently available commercial blood pressure monitors, but as Table 3.4 shows, artifacts not only often result in a failure of the measurement, but in other cases can lead to very inaccurate measurements.

The use of a capacitive sensor connected to a water packet implanted in the cuff to measure the effect of motion artifact was introduced in another conference paper (Park et al. 2007). The system consists of an adaptive filter tuned by the signal coming from the capacitive sensor. Problems encountered were in the form of extra oscillations after the artifact event due to the water packet.

A journal paper by Terry et al (1990) presented a sensor array system for motion artifact cancellation using piezoresistive sensors array. The experiment they performed was based on a tonometric monitor with the intra-arterial blood pressure as a reference. Results achieved an accuracy level of (2.24 ± 8.7) mmHg, which is slightly over the allowable standard deviation of error defined by ANSI/AAMI/ISO 81060-2, 2009.

Sorvoja et al. (2005) mentioned the use of a three point median filter to deal with artifacts in the introduction section of the paper. However, in the paper, no further details are provided. A small test was done to compare both the IMFSA and a median filter, which was proposed in a previous work, to examine the selectivity in both. IMFSA successfully detected the regions in the OMW defined by the accelerometer and suppressed the artifacts without affecting the remainder of the signal, whereas the median filter severely distorted the amplitudes of the pulses near the artifacts. As a result, the estimated SBP and DBP obtained with the proposed IMFSA method were closer to the reference measurements than those obtained with the median filter. (Smith1997).

`

As can be seen in Figure 3.42, using a three point median filter only in intervals of artifacts, which have been detected by the accelerometer, affects the signal shape and amplitude, as shown in the zoomed sample. Figure 3.43 uses the same case studied in Figure 3.42, but this time compares the effect of the median filter with that of the proposed IMFSA algorithm. The figure shows that the IMFSA algorithm saved the unique frequency components of the OMW, while the three points median filter adds clipping regions as well as extra unnecessarily attenuated regions.

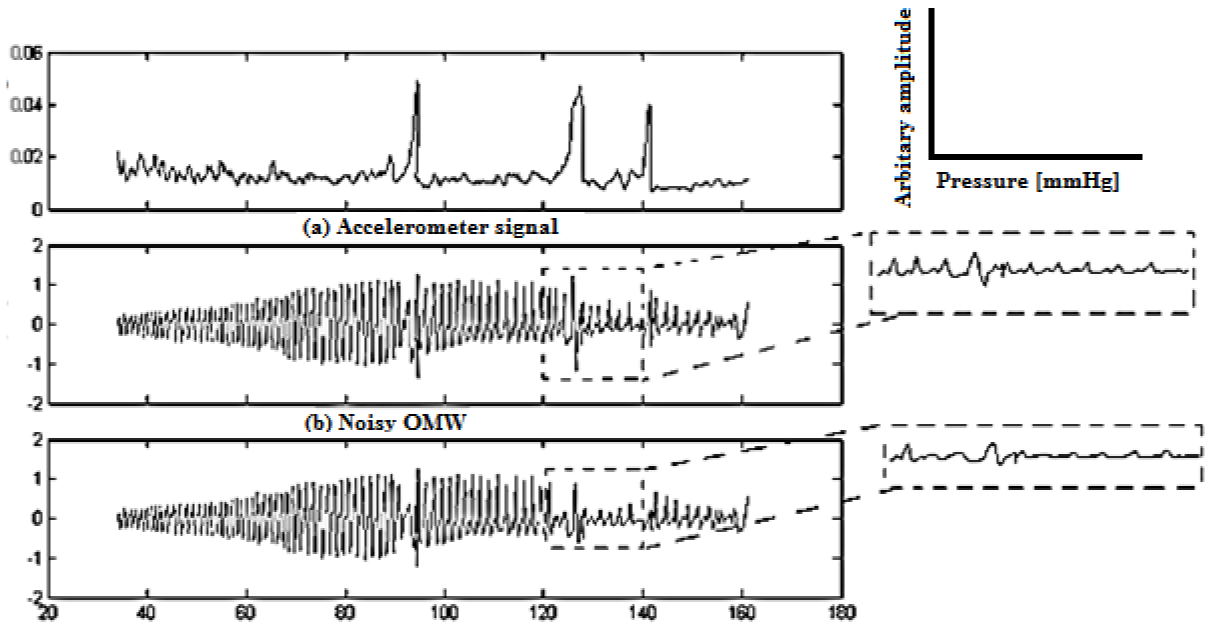

Figure 3.42: A case study that shows an OMW affected by three periods of motion artifacts and the results obtained after applying a median filter only in the intervals of artifacts as specified by the accelerometer.

`

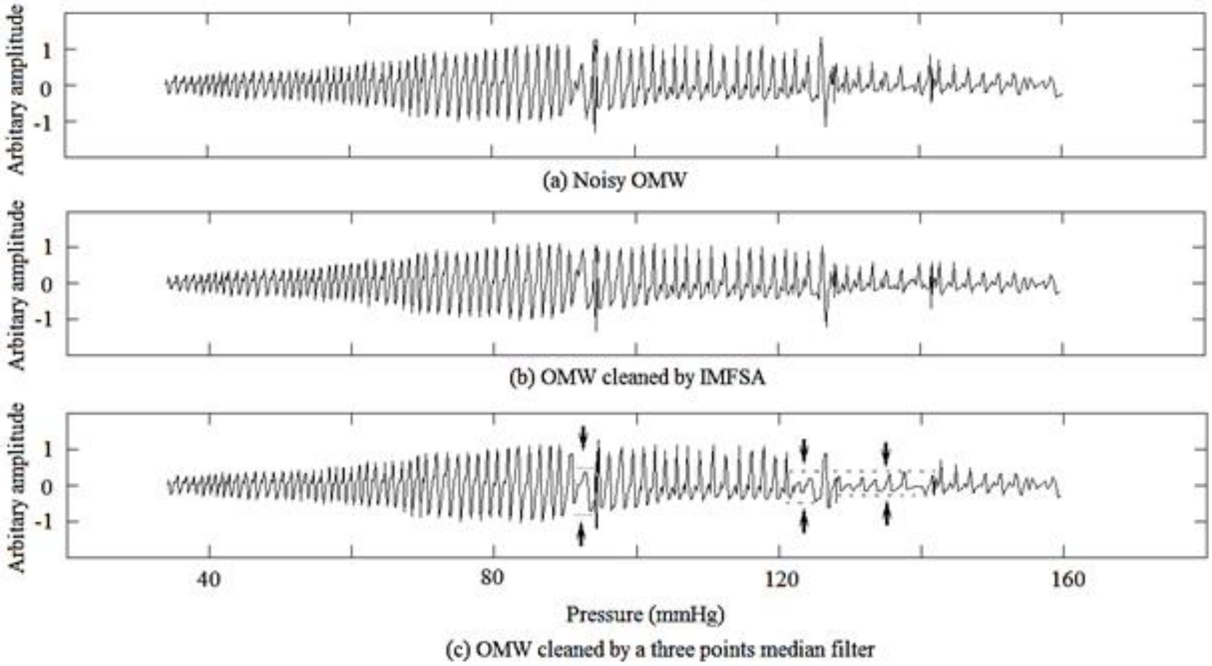

Figure 3.43: A comparison between the results obtained with the proposed IMFSA algorithm and an accelerometer based three points median filter on the same OMW shown in Fig. 3.42.

`

The envelopes for the cases shown in Figure 3.43 above are shown in Figure 3.44, and they resulted in a blood pressure SBP/DBP estimation of 120.2/73 mmHg with the IMFSA and an estimation of 121/71 mmHg in the case of the accelerometer-based three point median filter, with the reference pressure being 119/77 mmHg. Note that applying the median filter blindly (i.e. without having accelerometer-based knowledge of the artifact intervals), as suggested in the paper by Sorvoja et al. (2005) will result in 105/73 mmHg.

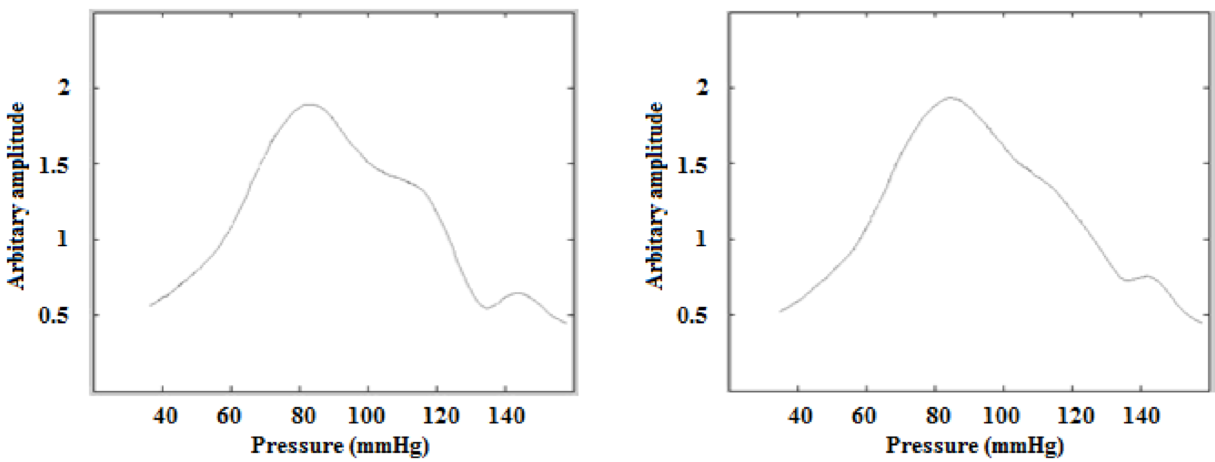

Figure 3.44: Envelope obtained after applying IMFSA (right) and an accelerometer-based three point median filter on the same OMW (left).

`

Figure 3.45 below shows a comparison between the results obtained by running IMFSA over the 25 tests, which include 56 transient motion artifacts in total, and the results from a method based on the three point Median filter and from the conventional oscillometric estimation without suppression of the motion artifacts. As can be seen, with both the SBP and the DBP, the IMFSA approach is the one with the lowest overall MAE.

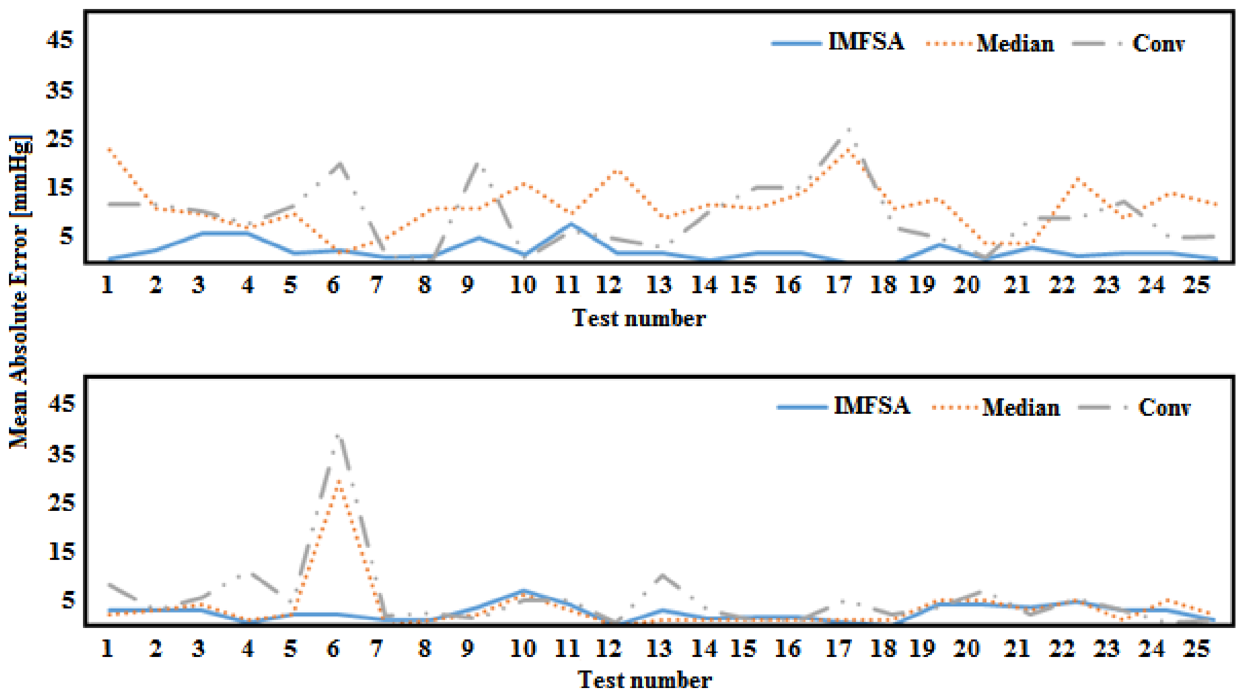

Figure 3.45: Comparison between MAE obtained with the IMFSA, method based on the Median filter, and the conventional oscillometric estimation without suppression of the motion artifacts over 25 tests, which include 56 transient motion artifacts in total. Top: results with the SBP and Bottom: Results with the DBP.

Another advantage of the proposed system is that it is completely automated. Moreover, placement of additional electrodes to measure ECG is not required, since a dry electrode is embedded in the cuff and the circuit can be completed by touching another electrode embedded in the measuring device. The accelerometer will also be embedded in the cuff and software will be responsible for the rest. The obtained accelerometer signal, as seen in Figures 3.2 and 3.11, shows a high level of reliability in detecting both small and large motion events.

`

The performance of both the IMFSA and IMFC algorithms was tested on the 35 recorded datasets obtained from five healthy subjects. The experiments we conducted involved 56 different motion artifacts during the blood pressure measurements, and ranged between one and three movements during each measurement.

The accuracy of both proposed algorithms was analyzed in terms of three performance measures: mean error (ME), standard deviation of error (SDE), and mean absolute error (MAE). The results were compared with the FDA-approved Omron oscillometric BP monitor (HEM-790IT). This monitor has gone through various clinical validation tests and its performance satisfies the standards set forth by the European Society of Hypertension and the Association for the Advancement of Medical Instruments (Omron Healthcare Inc 2006; Feghali et al. 2007; Coleman et al. 2008).

Results obtained using the IMFSA algorithm to suppress the effects of transient motion artifacts show a mean absolute error of 2.4 mmHg for both SBP and DBP, in comparison with around 9.4 mmHg and 5.3 mmHg for SBP and DBP respectively obtained using the conventional approach (Table 3.3). The spread of the error was measured using the SDE. Results obtained with the IMFSA were 3.1 mmHg and 2.9 mmHg for SBP and DBP, respectively, in comparison with the conventional approach which gave 11.6 mmHg for SBP and 8.7 mmHg for DBP.

The IMFC algorithm to suppress the effects of vibration artifacts resulted in a mean absolute error of 0.8mmHg and 1.1 mmHg for SBP and DBP, respectively, in comparison with the conventional approach that resulted in 3.1 mmHg and 3.5 mmHg for SBP and DBP (Table 3.2). In terms of the spread of error, the IMFC resulted in an SDE of 1.0 mmHg and 1.5 mmHg for SBP and DBP, respectively, while the conventional approach, gave an SDE of 3.8 mmHg and 5.5 mmHg for SBP and DBP.

The performance of the proposed algorithms was investigated further using Bland–Altman analysis (Figures 3.35, 3.36, 3.39, and 3.40). This technique makes it easier to study the agreement between any two methods. One of the signs supporting the choice of using IMFSA and IMFC for suppressing transient motion artifacts and vibrations, respectively, is that the limits of agreement (LOA) with the reference measurements are narrower than those obtained with the conventional approach.

`

These results indicate that both the proposed approaches were able to successfully suppress the artifact signals in the OMW and improve the blood pressure estimation. Comparing the results obtained using the proposed methods with the conventional oscillometric approach that does not include an EMD-based stage for artifact suppression shows that the two proposed methods meet the requirements of the international standard ANSI/AAMI/ISO 81060-2, 2009.

Future work could involve using invasive intra-arterial methods to obtain more accurate reference measurements for the purpose of validation, expanding the study to include more extreme motion artifacts, such as those associated with physical activity, and the possibility to integrate the algorithms in a microcontroller.

`

CHAPTER 4: COMPENSATION FOR MEDIUM TERM DRIFT DUE TO ENVIRONMENTAL CHANGES

4.1 Introduction

Accuracy in blood pressure measurements can be affected by different factors (Figure 4.1). Other factors related to the external noise and fluctuation in the power supply (electrical bias) may affect the measurements but are not considered major factors (Sinnadurai and Wilson 1982). The figure shows that environmental factors, and specifically the ambient temperature, is one of the influencing factor during the measurement of blood pressure. Other environmental factors such as humidity are considered negligible in comparison with temperature (Zernike et al. 2013). The figure also shows that time (ageing) is another influencing factor, but this will be dealt with in Chapter 5.

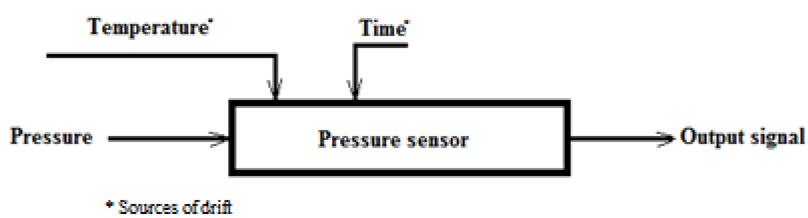

Figure 4.1

Figure 4.1: A general view of influencing factors on a pressure sensor

As seen from the literature review in Chapter 2, the way the effect of temperature has been studied in the blood pressure field has typically been related to its effect on the human body during the measurement and not its effect on the device itself, except in some studies related to invasive blood pressure measurements (Fujiwara et al. 1995; Kalia 2014; Van den Hurk et al. 2015).

`

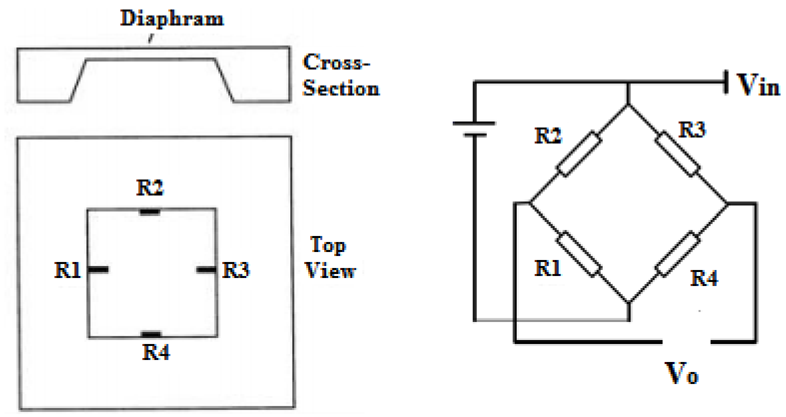

Figure 4.2: Internal structure of a piezoresistive sensor. Left: placement of the resistances on the diaphragm. Right: The Wheatstone bridge configuration.

When no pressure is applied, the steady state output V_o is calibrated to be zero. Applying a pressure will change V_o to a non-zero value. Semiconductor wafers are used in order to add more integration, mechanical stability, higher sensitivity, and better efficiency (Beclin et al. 2005). From Figure 4.2:

$$\frac{V_o}{V_{in}} = \frac{R_1R_3 - R_2R_4}{(R_1+R_2)(R_3+R_4)} \tag{4.1}$$

In general, blood pressure monitor user manuals always include a section that discusses the ideal operating temperature, and how the manufacturer is not responsible for measurements that take place out that range. Most of the time, the range that is indicated is between (10 – 40) ^{o}C (Samsung 2006; A&D Medical 2007; Omronhealthcare 2012).

`

4.2 Temperature drift

To demonstrate the phenomenon of temperature drift, semiconductor theory has been used (Tamim and Estrada 1991; Tian et al. 2009; Suja et al. 2013). In general, the resistance of a material can be simply described as a function of structure dimensions:

$$R = \rho\frac{L}{A} \tag{4.2}$$

where, “L” is the material length, while “A” is its cross section and “ρ“ is the resistivity.

Furthermore, Equation 4.2 shows that any changes in “A” and/or “L” cause a change in the resistance”$\mathbf{\Delta R}$ “:

$$\frac{\Delta R}{R} = \frac{\Delta \rho}{\rho} + \frac{\Delta L}{L} + \frac{\Delta A}{A} \tag{4.3}$$

In other words, both dimensions and resistivity changes cause the resistance to change. It is also possible to quantify the strain “ε“of the material as:

$$\varepsilon = \frac{\Delta L}{L} \tag{4.4}$$

Another important parameter here is the gauge factor “G”, which is an indicator of the strain sensitivity.

$$G = \left(\frac{\Delta R}{R}\right)/\left(\frac{\Delta L}{L}\right) \tag{4.5}$$

Substituting 4.3 in 4.4 results in:

$$G = \frac{\Delta R}{\varepsilon R} \tag{4.6}$$

`

Piezoresistive sensors are like other resistors; they have a temperature coefficient of resistance (TCR) and a temperature coefficient of gauge factor (TCGF) (Hwang et al. 2004). Including these two factors will add more accuracy to the design of the sensor:

$$\mathrm{TCR} = \frac{1}{\Delta \mathrm{T}} \frac{\Delta \mathrm{R}}{\mathrm{R}} \tag{4.7}$$

Or

$$\mathrm{TCR} = \frac{1}{\Delta \mathrm{T}} \frac{R_{T-}R_{O}}{R_{T}} \tag{4.8}$$

And for the temperature coefficient of gauge factor:

$$\mathrm{TCGF} = \frac{1}{\Delta \mathrm{T}} \frac{G_{T-}G_{O}}{G_{T}} \tag{4.9}$$

where ΔT is the temperature change, R_o and G_o are the sensor's steady-state resistance and gauge factor respectively, and R_T and G_T are the new resistance and gauge factor due to the temperature change.

Results from the above analysis show how the applied pressure affects the resistance of a piezoresistive sensor by changing the dimensions of the structure, which in turns can be measured using a circuit configuration such the one shown earlier in Figure 4.2. Another conclusion is that there is a direct relation between the temperature and the value of the steady state resistance that is dependent on a temperature coefficient.

`

Another way to describe the thermal behaviour of piezoresistive sensors is by a factor called the piezoresistive correction factor. This factor, shown in Equation 4.9, was first extracted from an analytical model by Lenkkeri (1986), and it shows the effect of both temperature and doping concentration on the piezoresistive behaviour.

$$\mathrm{P(N,T)} = \frac{300}{T}\frac{1}{\left(1+\exp\left(-\frac{E_f}{K_b T}\right)\right)\ln(1+\exp\left(\frac{E_f}{K_b T}\right))} \tag{4.10}$$

where E_f represents the Fermi energy, N is the doping concentration, T is the temperature in Kelvin, and K_b is Boltzmann's constant. Using this correction factor, the piezoresistive behaviour can now be described as:

$$\Pi\ (\mathrm{N,T}) = \Pi\ (N_o, 300K) * P(N,T) \tag{4.11}$$

where Π (N,T) is the piezocoeficient value for low-doped silicon, N and No are the doping concentration at any time and the initial doping concentration respectively (Abdelaziz et al. 2014). The significance of this coefficient is due to the fact that it explains the relation between the change in the electrical resistance and the applied stress (Kanda 1982), as given in the relation below:

$$\Delta R/R = \pi\sigma \tag{4.12}$$

where σ is the stress on the semiconductor wafer.

According to Hooke's law (Kanda 1982):

$$\sigma = E * \varepsilon \tag{4.13}$$

where E is Young's modulus, and ε is the strain

The behaviour of silicon piezoresistive sensors was examined by Abdelaziz et al. (2014). Results obtained show that P(N,T) is inversely proportional to both the temperature and the doping concentration in the range of 230 – 315 K (or -43.15 to 41.85 C), which includes our range of interest for operating blood pressure monitors (Figures 4.3). Figures 4.4 and 4.5 also show how temperature affects the piezoresistive coefficient and sensor output voltage, respectively.

These figures show that the temperature is an important factor in determining the piezoresistive behaviour.

`

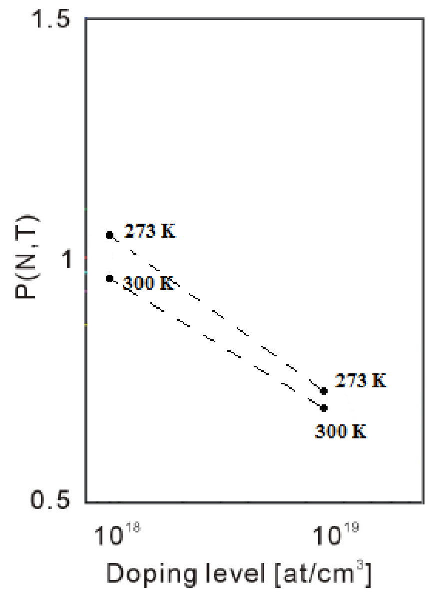

Figure 4.3: Piezoresistance correction factor P(N,T) as function of temperature and doping level for p-type silicon (Adapted with permission from Abdelaziz et al., 2014).

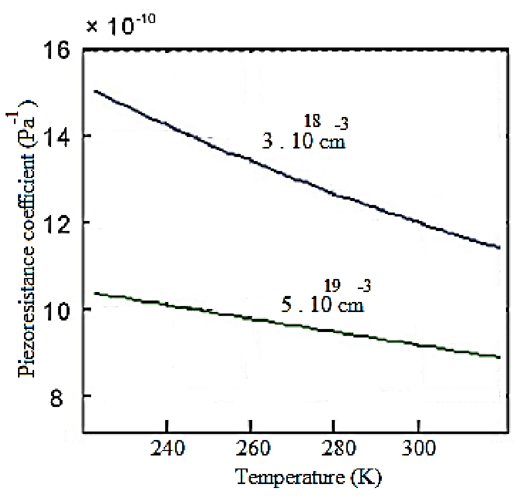

Figure 4.4: Temperature effect on the piezoresistance coefficient for two different piezoresistive sensor structures, with ($3x10^{18}$) cm^{-3} and ($5x10^{19}$) cm^{-3} doping levels. (Adapted with permission from Abdelaziz et al., 2014)

`

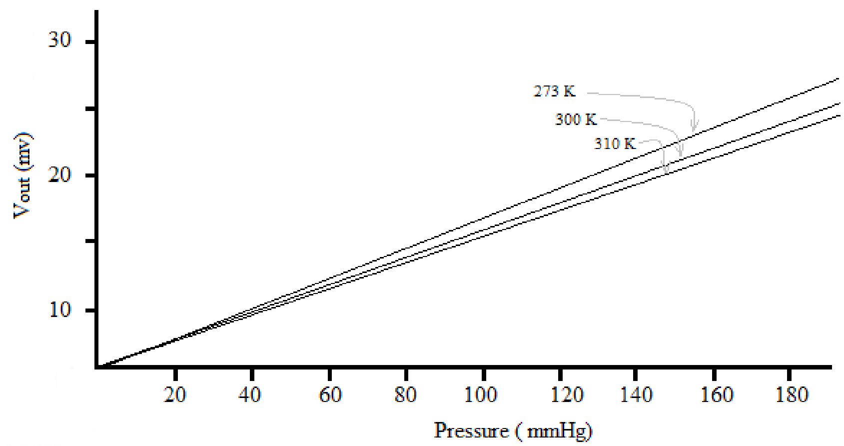

Figure 4.5: Temperature effect on the output of a piezoresistive sensor under different applied pressure values. (Adapted with permission from Abdelaziz et al., 2014)

The temperature drift is determined by the temperature dependence of both the resistance and the gauge factor (Equations 4.8 and 4.9), while both are a function of structure dimension. As shown in the literature review in Chapter 2, no published work has yet been done to deal with the temperature effect on non-invasive blood pressure monitors. Most of the research is either concerned with invasive blood pressure systems or the temperature effect on human physiology during the measurement itself. On the other hand, according to most pressure sensor datasheets, the output is always going to be temperature dependent.

From the literature, it is possible to show some results related to how the temperature affects the performance of piezoresisitve sensors. The use of such studies, even if they are not related to the blood pressure field, can be used to prove the point. Kim and Wise (1983) conducted a study in a high pressure application to describe the magnitude of the temperature dependence in a piezoresistive sensor having a diaphragm thickness of 19µm over a wide range of temperatures. Results from the study show that the drift can reach 700 mmHg in the case of a zero applied pressure and a temperature range between -20 and 40 ^{o}C. This means that using the sensor under such conditions requires having a compensation stage.

`

4.3 Methods

4.3.1 Compensation system

In this part of the research, a subsystem is responsible for monitoring the piezoresistive sensor's resistance changes with respect to temperature, and it is implemented to act as a reference for compensation purposes. The data collected through this monitoring function can be easily stored in a look-up table (LUT), and will be readily accessed when the compensation is required. As seen in Figure 4.6 below, a temperature sensor is mounted on the device to collect temperature data. The next step is to match this data with the corresponding measurements of the sensor's resistance to form an LUT.

The data collection is done offline, with the device off, and the measurements are in the form of:

$$R_{measured} = R_o \pm \Delta R_{temp} \tag{4.14}$$

Here, $R_{measured}$ is the detected resistance of the sensor, R_o is the steady-state resistance of the same sensor, and ΔR_{temp} is the resistance change due to temperature change.

The sensor's resistance and the ambient temperature are collected synchronously, and these two sets are saved in microcontroller memory in the form of an LUT. In Figure 4.6, all the processing steps that take place in the microcontroller are bordered by the dashed line. The block labeled as Algorithm represents the oscillometric blood pressure estimation algorithm

`

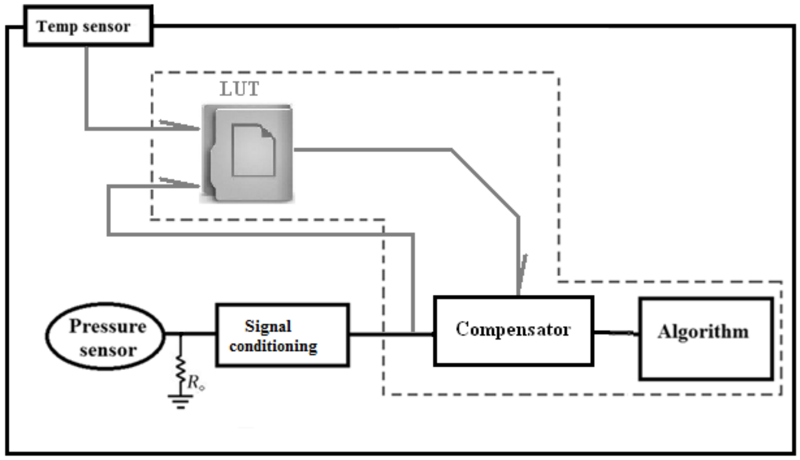

Figure 4.6: Overall proposed temperature compensation system, where the pressure sensor's resistance is monitored and a compensator stage is used to adjust the output according to the ambient temperature.

After the look-up table has been generated, the compensator will be able to adjust the output based on the ambient temperature during the on-line measurement. At any time, the measured pressure will be a composition of resistance changes due to pressure and due to temperature (Equation 4.15).

$$R_{measured} = R_o \pm \Delta R_{pressure} \pm \Delta R_{temp} \tag{4.15}$$

where R_o is the steady-state value for the sensor's resistance, ΔR_{temp} is the change in the sensor's resistance due to temperature and $\Delta R_{pressure}$ is the change in the sensor's resistance due to the applied pressure.

Measuring changes in resistance is mostly done through measuring changes in the voltage across it (Figure 4.7), so it is possible to write the formula as:

$$V_{measured} = V_o \pm \Delta V_{pressure} \pm \Delta V_{temp} \tag{4.16}$$

where $V_{measured}$ is the measured voltage across the resistance, V_o is the steady state voltage, and both ΔV_{temp} and $\Delta V_{pressure}$ are changes in voltage due to changes in temperature and pressure respectively.

`

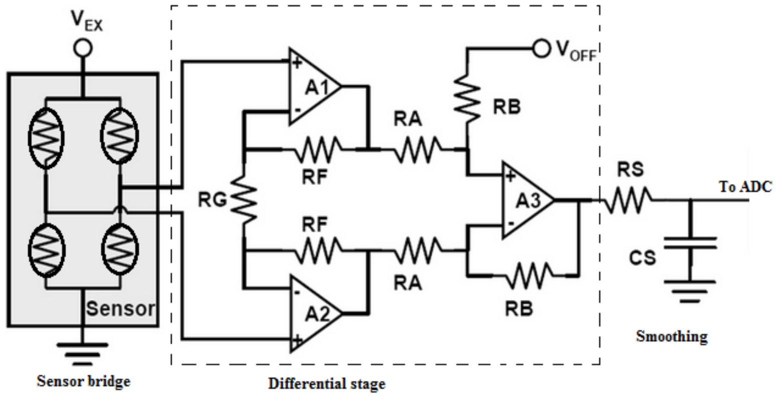

Figure 4.7: Circuit conditioning to convert the changes in a piezoresistive sensor's resistance to voltage. Starting from the left, the bridge circuit is shown, to the middle stage where a differential amplifier measures the bridge output, and finally there is a smoothing stage, consisting of a low-pass filter.

4.3.2 Compensation System design

Figure 4.8 below shows a detailed view of the proposed compensation system to deal with effects of temperature changes. The system consists of four main blocks; "A", "B", "C" and "D". In block "A", the subsystem is responsible for detecting the ambient temperature through the temperature sensor LM35 (Texas Instruments, Dallas, Texas 75243 USA) at the time of blood pressure measurement. Note that the temperature signal is digitized in this block with respect to a stable reference voltage. The stable (fixed) voltage network is designed so it will be temperature independent. It uses the LM136 thermally stabilized subsurface zener diode, which guarantees that the temperature error will not exceed the rated 2 PPM/℃ over a temperature range of −55 ℃ to +125 ℃. (Jung 1994; Dawes 1998).

In Block "B", the system is responsible for generating the signal needed to compensate for changes in the pressure sensor's internal resistance due to temperature. This block is based on a microcontroller, which will read both the sensor's resistance and the temperature reading, and perform compensation based on the LUT stored in the system. Block "C" is a user display, which makes it easier to troubleshoot and modify the system if required.

`

Lastly, block “D” represents the signal conditioning for the pressure sensor’s resistance. In this block, it can be seen that a voltage divider is used to measure the changes in the sensor’s resistance followed by an inverting op-amp configuration used to amplify the signal before feeding it to the microcontroller. The steady-state output voltage from this stage to the microcontroller follows the following equation:

$$V_o = V_{cc}\,\frac{R_s}{R_s+R_1} * \left(1+\frac{R_3}{R_2}\right) \tag{4.17}$$

where, V_{in} is a 5V dc voltage source and R_s is the piezoresistive sensor’s resistance.

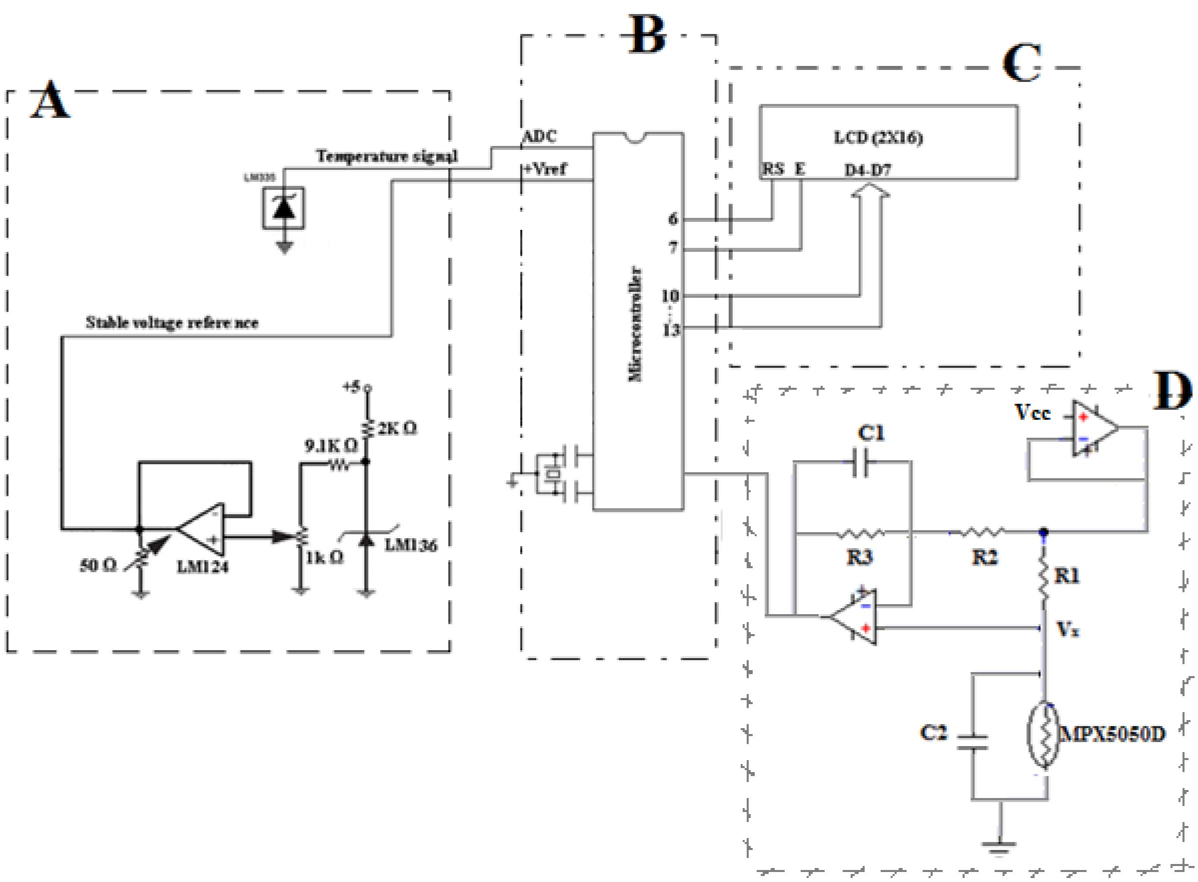

Figure 4.8: A detailed diagram of the proposed system to compensate for temperature changes divided into four main stages (A, B, C, and D). See the text for a description of the stages. Note that the piezoresistive sensor (MPX5050D) is represented here by a single resistor, but its internal structure is a Wheatsone bridge as described in Figure 4.2.

`

From Figure 4.8 above, it is possible to conduct a performance uncertainty analysis on block D, taking into account the following parameters:

- The piezoresistive sensor's resistance, R_s = 1.34 kΩ with an accuracy of 2.5% according to its datasheet, not including the temperature effect.

- R_1 = 1 kΩ, R_2 = 12 kΩ, R_3 = 3.3 kΩ., with an uncertainty of 0.1% (Figliola and Beasley 2015).

Applying the root sum-squares (RSS) approach (Dieck 1997), the propagation uncertainty can be estimated as follows:

$$\Delta V_o = ((\frac{\partial R}{\partial R_1}\, UR_1)^2 + (\frac{\partial R}{\partial R_2}\, UR_2)^2 + (\frac{\partial R}{\partial R_3}\, UR_3)^2 + (\frac{\partial R}{\partial R_s}\, UR_s)^2)^{1/2} \qquad (4.18)$$

Where, UR_1, UR_2, UR_3, and UR_s are the imprecision in these resistors.

Now applying the approach in 4.18 on the output signal (Formula 4.17) of this block (Block D) leads to:

$$\frac{\partial R}{\partial R_1} = \frac{-(R_2R_S - R_SR_3)(R_2)}{(R_2R_S + R_1R_2)^2} \qquad (4.19)$$

$$\frac{\partial R}{\partial R_2} = \frac{R_S(R_2R_S + R_1R_2) - (R_2R_S + R_SR_3)(R_1 + R_S)}{(R_2R_S + R_1R_2)^2} \qquad (4.20)$$

$$\frac{\partial R}{\partial R_3} = \frac{-(R_S)}{(R_2R_S + R_1R_2)} \qquad (4.21)$$

$$\frac{\partial R}{\partial R_s} = \frac{(R_2 + R_3)(R_2R_S + R_1R_2) - R_2(R_2R_S + R_1R_2)}{(R_2R_S + R_1R_2)^2} \qquad (4.22)$$

Finally, the overall error contributed by the resistors of the block comes up as:

$$\Delta V_o = \pm 0.0018\, V \qquad (4.23)$$

`

These results give confidence that the effect of the uncertainty in block D, including all the resistors, will not contribute more than 0.027 mmHg to the overall drift (Sinnadurai 1982).

4.3.2.1 Compensation system implementation

The system was implemented in a professional software environment called "Proteus Professional" (Labcenter Electronics Ltd, North Yorkshire UK). One advantage of using this software is that it provides accurate simulations of a large variety of different sensors, actuators, displays, and microcontrollers used in industry. Another advantage is that it provides a professional environment for embedded system design and implementation, with the ability to load .hex code to the microcontroller for testing purposes.

For the system implementation (Figure 4.9), a piezoresistive pressure sensor from the MPX family (Freescale Semiconductor, Texas, USA) is used as our pressure sensor and an LM35 sensor (Texas Instruments, Texas, USA) is used for temperature monitoring.

For LM35, the datasheet specifies a linear relation between output voltage and the temperature in the range of -50 to 125 ^{o}C, with a resolution of 10mV/°C. The used microcontroller, PIC18f4550 (Microchip Technology Inc, USA, Chandler, Arizona), was chosen for its suitable ADC (Analog to Digital Convertor) ports, SPI (Serial Peripheral Interface) option, and internal memory.

The ADC, which is used to measure both the temperature and the piezoresistive sensor's resistance, has an 8 bit resolution, with a voltage reference of 3V. A stable voltage reference circuit is designed based on the precision regulator, LM136-5.0, as suggested by Dawes (1998) and Jung (1994).

`

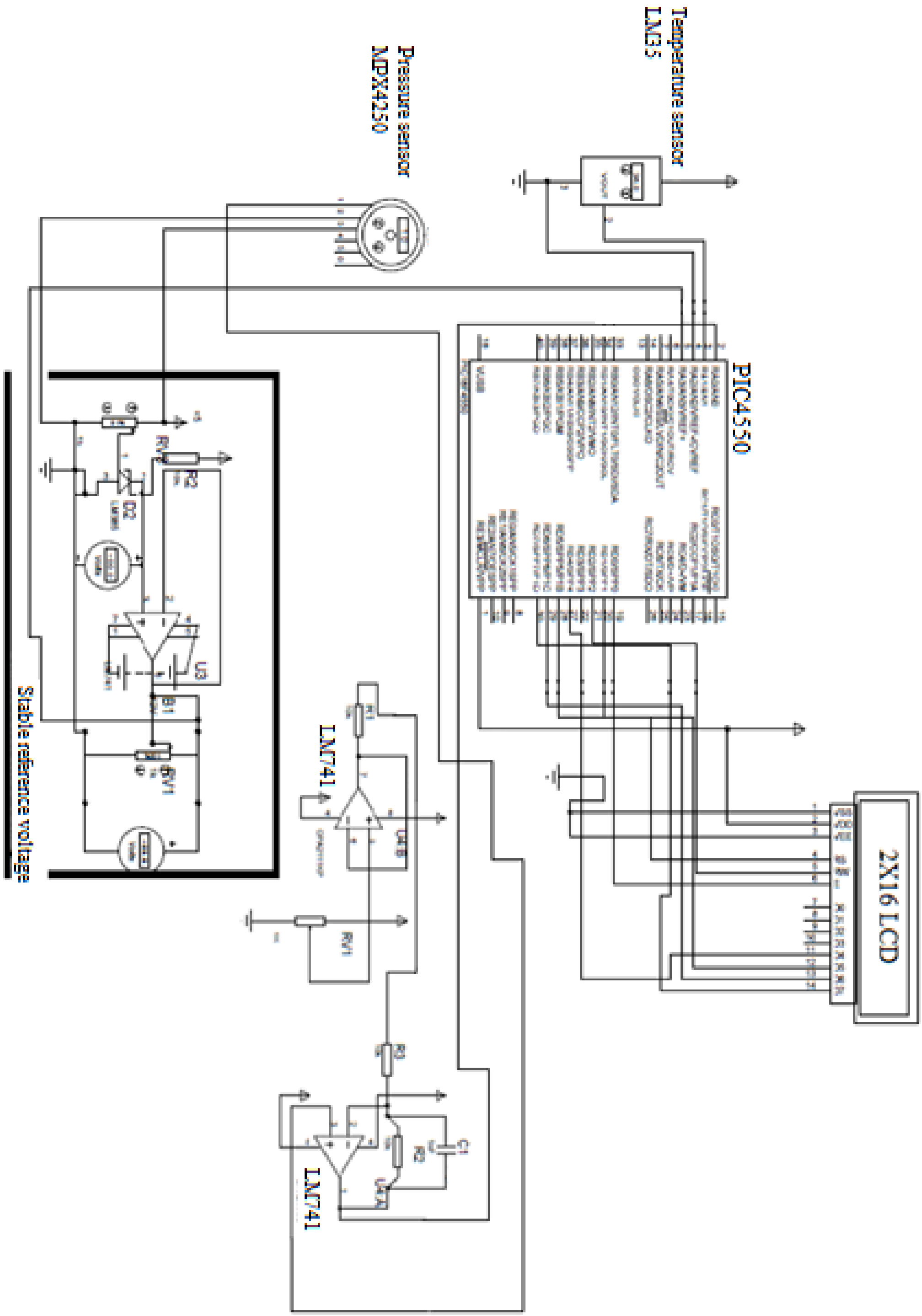

Figure 4.9: Compensator system as it is built using Proteus Professional (screenshot). The system consists of a stage for temperature monitoring, a stage for pressure monitoring, and an ADC.

`

4.3.2.2 Compensation system algorithm

As shown in Figure 4.10, the compensator will have an LUT stored in it. At any time when the compensation action is required, the system will automatically open the LUT and use interpolation to send an appropriate compensation signal to the microcontroller.

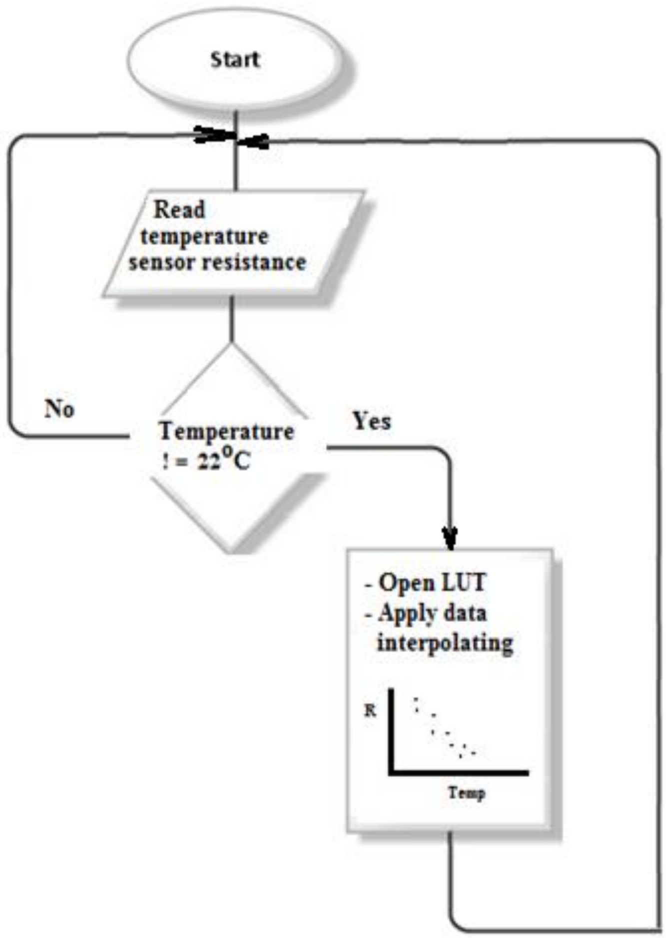

Figure 4.10: A flow chart summarising the compensation algorithm stored in the microcontroller. Note that the reference temperature value (22ºC) depends on the calibration temperature of the device.

4.3.3 Temperature drift in the MPX4250D pressure sensor

This part of the study was conducted on a physical Freescale pressure sensor model # MPX4250D (Freescale semiconductor USA, Austin, Texas) (Appendix D), which is a common piezoresistive pressure sensor frequently used in biomedical applications. Figure 4.11 shows the sensor package and its internal structure.

According to the datasheet, this sensor's nominal temperature transfer function is given by:

$$V_o = V_s(P * 0.018 + 0.04) \pm (P_{error} * T_{error} * 0.018 * V_s) \tag{4.24}$$

where P is the measured pressure, P_{error} is the pressure error, T_{error} is the temperature error factor, and V_s is the supply bias voltage given by:

$$V_s = 5.0 \ \pm 0.25 \text{ V} \tag{4.25}$$

Note that in the last equation (Equation 4.25), the uncertainty term for measuring the dc voltage supply (Vs) is suggested by the datasheet to be 0.25V, even though it is possible to find more precise voltage regulators with higher accuracy, like MAX6126 (Maxim Integrated, USA, CA, San Jose) that has a maximum uncertainty of ±0.02% according to its datasheet.

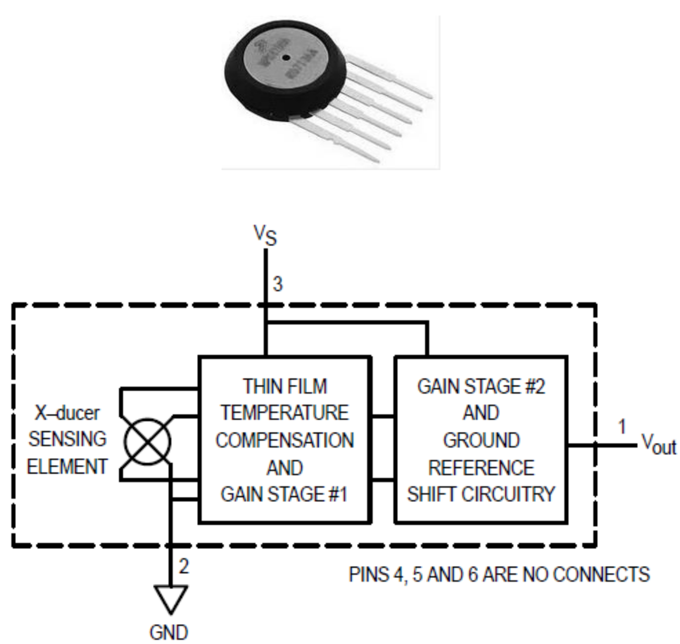

Figure 4.11: MPX4250D pressure sensor package (top) and the main internal stages as shown in the sensor's datasheet (bottom).

`

From Equation 4.24 it is seen that the output depends on two factors beside the pressure, which are the temperature and the pressure error. According to the datasheet, the temperature error factor is divided into three linear functions, as seen in Figure 4.12, while the pressure error has a constant value of 1 over the whole range from -5 to 85 °C.

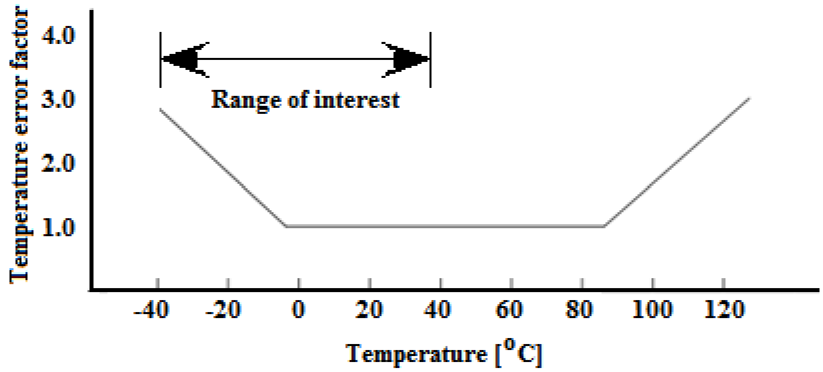

Figure 4.12: Temperature error factor as shown in MPX4250D piezoresistive sensor datasheet

The relation in Figure 4.12 above shows the steady-state response of the sensor in different operating temperatures, without showing any information related to the transient response.

A data logger was implemented using a PIC microcontroller model PIC18f4550 (Microchip Technology Inc, Arizona USA), as shown in Figure 4.13 below. For temperature readings, a temperature/humidity meter was used (Model HT 350 - Ongguan Xintai Instrument Co., Ltd, Guangdong China). It possesses a humidity accuracy of ± 2% RH (Relative humidity), an air temperature accuracy of ± 0.5°C, and a resolution of 0.01% RH. As will be seen in the next section, experimental measurements were compared with the values given by Equation 4.24 above to determine if the data provided by the manufacturer are accurate.

`

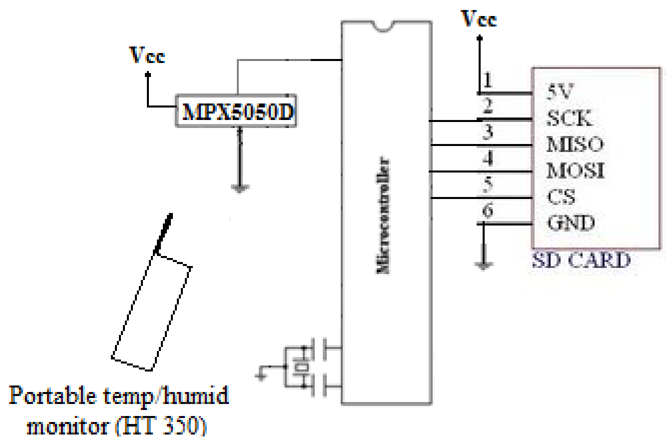

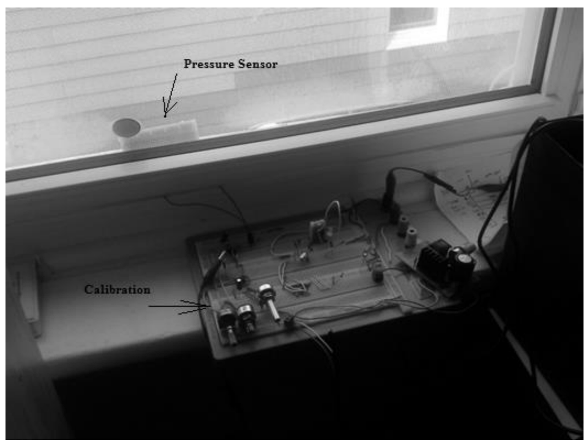

Figure 4.13: Experimental set-up to monitor temperature effect on an MPX4250D pressure sensor. Top: The system schematic, and Bottom: The system implementation. See the text for a description of the set-up.

`

4.4 Experimental data

4.4.1 Piezoresistive sensor thermal drift

Three operating temperatures were used in order to study the pressure sensor's behaviour. The temperatures were: 30 ^{o}C, 22 ^{o}C, and -8 ^{o}C. Each measurement was repeated 20 times in order to estimate the variability, and measurements are reported as mean ± stdev.

In the first part of the experiment, the sensor's output was monitored after moving it from room temperature (22 ± 0.5 ^{o}C) to a higher temperature atmosphere (30 ± 0.5 ^{o}C). Results from this part show a change in the sensor's output of about 6 % in the first 90 ± 0.5 s, which is calculated as a percentage by dividing the voltage reading at 30 ^{o}C by the voltage reading at our reference temperature of 22 ^{o}C. The mean absolute difference was +0.606 ± 0.027 V. In the second part of the experiment, the sensor was moved from room temperature (22 ± 0.5^{o}C) to a lower ambient temperature of (-8 ± 0.5 ^{o}C). The obtained results show a change in the sensor's output of about 7.6% within 60 ± 0.5 s. The mean absolute difference in this case was 0.0768 ± 0.017 V.

Figure 4.14 below represents the data obtained from the experiment on the MPX4250D piezoresistive pressure sensor in the form of the absolute difference between the sensor output before and after changing the ambient temperature.

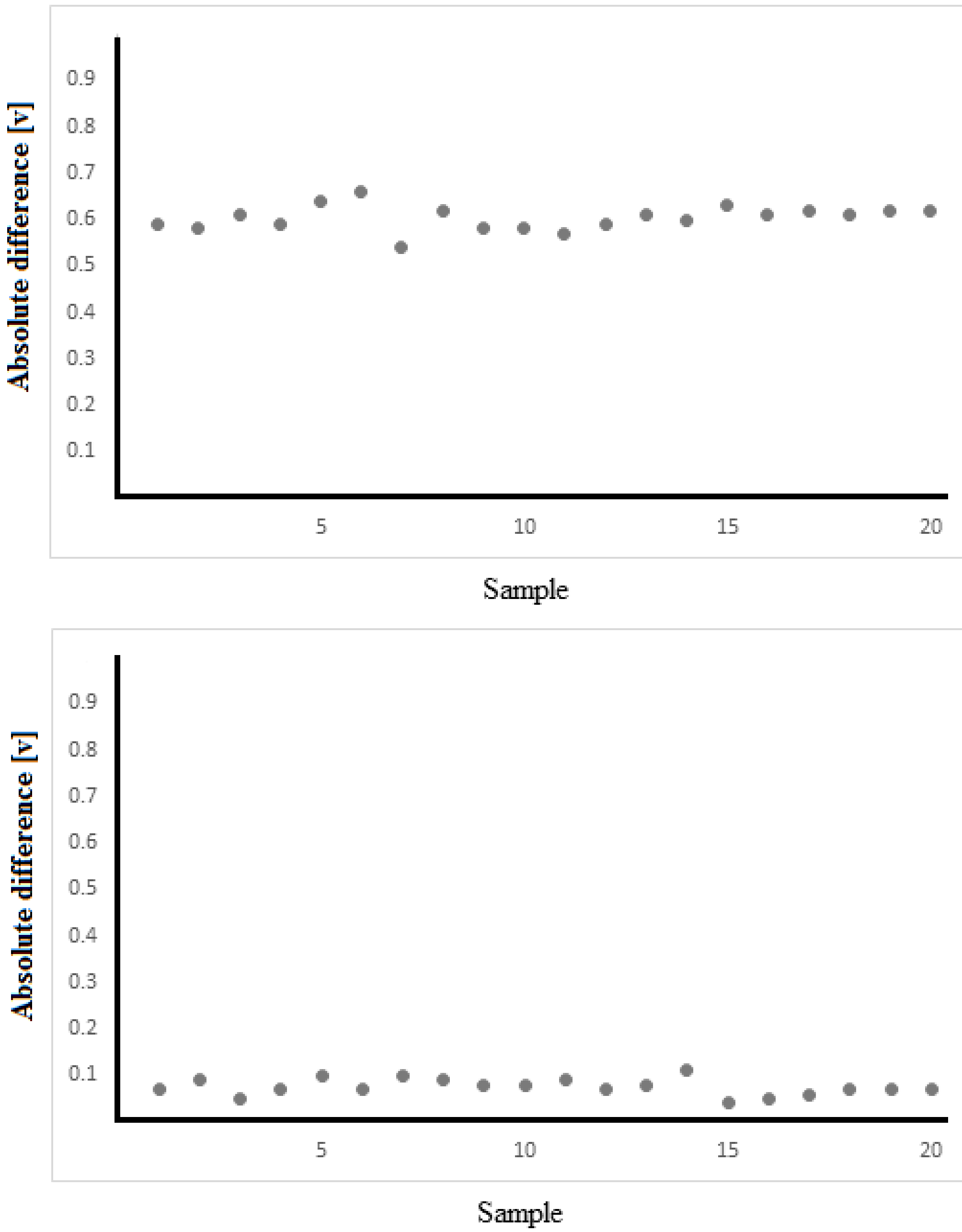

Figure 4.14: Results obtained by monitoring the output voltage from the piezoresistive sensor (MPX4250D). Top: +22 to +30ºC, and bottom: +22 to -8ºC.

`

Based in the sensor's datasheet (i.e. Equations 4.24 and 4.25), the sensor's output in the temperature range -5 to 85 ^{o}C and zero influencing pressure should not vary with temperature since the temperature error factor and the pressure error are indicated to be constant in this temperature range. However, our results show that this is not the case in practice.

4.4.2 Piezoresistive sensor thermal drift compensation

To simulate piezoresistive sensor drift due to temperature changes, data which represents a real case study from a paper published by Scilingo et al. (2003) was used along with another set of data representing the SBP monitored over four months (Bersbach 2010). Figure 4.15 shows the SBP profile, and the temperature profile.

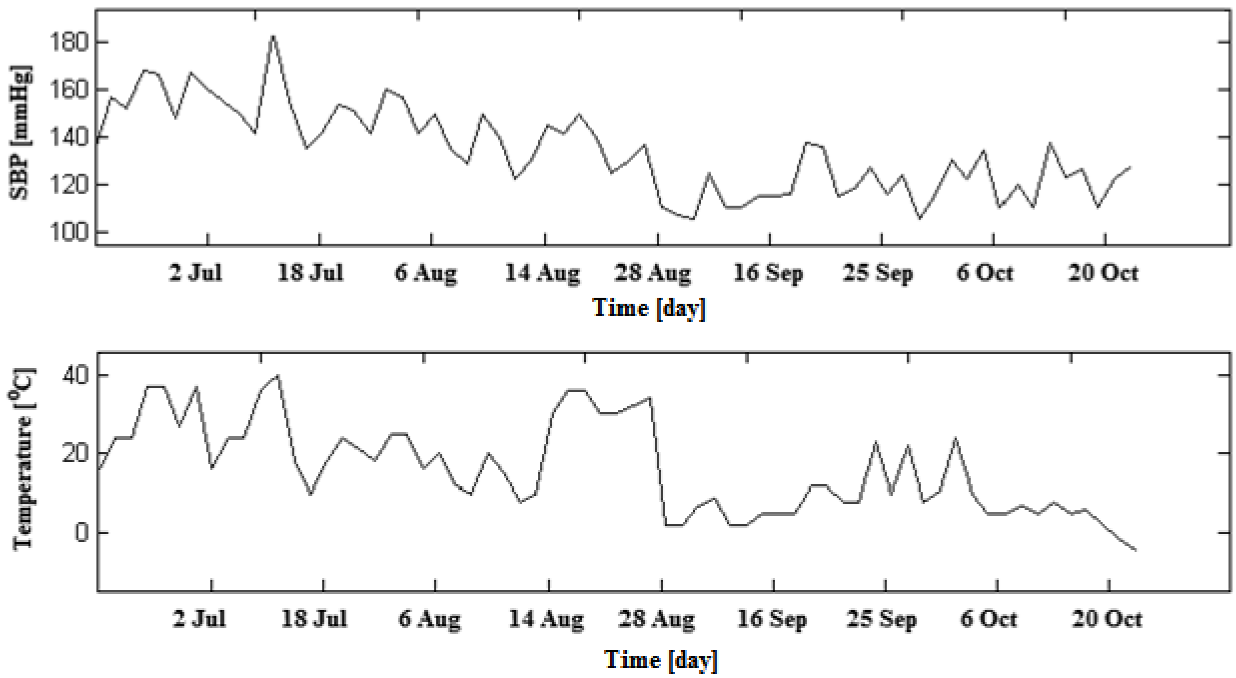

Figure 4.15: Case study to evaluate the effect of temperature-related drift on the SBP over four months. Top: SBP profile. Bottom: Temperature profile.

`

The compensation to temperature drifts takes place using the ability of measuring the difference between the steady-state resistance value at room temperature (defined here as 22 ^{o}C) and the LUT saved by the system. At any time when compensation is required, the system will automatically open the LUT and use interpolation to send an appropriate compensation signal to the MCU (Microcontroller unit).

As explained in sub section (4.3.1 Compensation system), the data collection for the LUT is done offline, possibly at the manufacturer, with the device off, and the measurements are in the form of:

$$\mathrm{R}_{measured} = \mathrm{R}_{o} \pm \Delta\mathrm{R}_{temp} \tag{4.26}$$

Here, $R_{measured}$ is the detected resistance of the sensor, R_o is the steady-state resistance of the same sensor, and ΔR_{temp} is the resistance change due to temperature change.

`

The LUT programmed in the MCU unit is shown in Table 4.1 below. From the table, the temperature values and equivalent resistance changes and pressure changes are summarized.

Table 4.1: The suggested lookup table used in the MCU based on Abdelaziz et al. (2014) and Scilingo et al. (2003)

Temperature [ºC]	**Change in Resistance [kΩ]**	**Change in Pressure [mmHg]**
-10	+0. 500	5.000
0	+0.400	4.000
10	+0.325	3.250
15	+0.315	3.150
20	+0.300	3.000
22	0	0
25	-0.380	3.800
30	-0.360	3.600
35	-0.350	3.500
40	-0.280	2.800
45	-0.270	2.700
50	-0.210	2.100

`

Figure 4.16 below shows the temperature drift influence on the SBP profile over a period of four months. From the figure, it can be seen how the SBP value are shifted from its true positions over time.

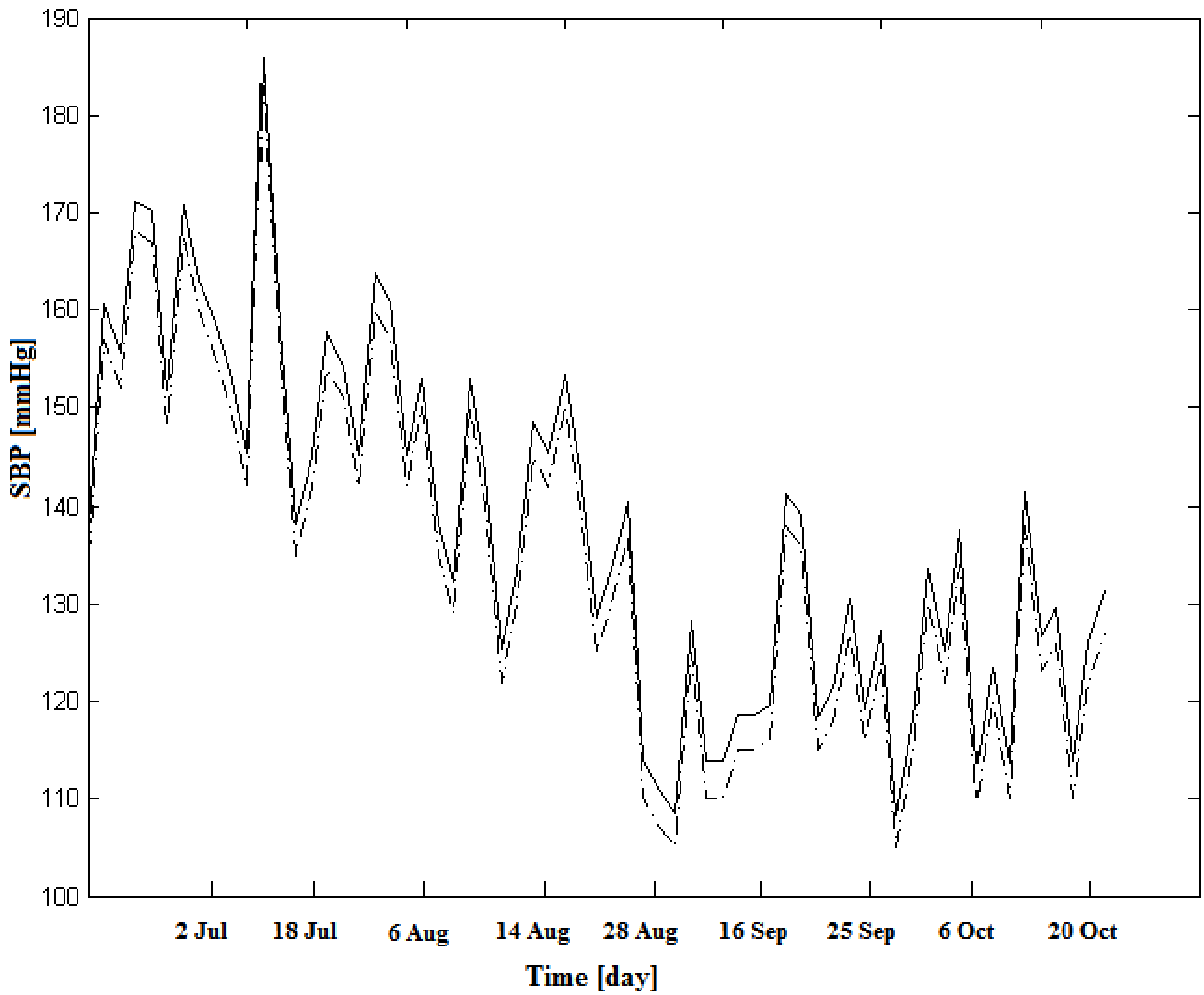

Figure 4.16: Case study to show the effect of temperature on the SBP profile over a period of four months. Dotted line: The original SBP profile. Solid line: Temperature effect on the same SBP profile.

`

The system compensation is based on a temperature reading which is done by the military standard temperature sensor LM35. This temperature sensor is considered a wide range (-55 – 150 ^{o}C) sensor with a linear relationship between the temperature and the output voltage. Furthermore, the sensor accuracy (shown in Figure 4.17) is in the range of ±0.5 ^{o}C. Note that the accuracy in other components under the effect of temperature can be neglected (Sachenko et al. 2000), as shown in the uncertainty calculations done earlier this chapter (Section 4.3).

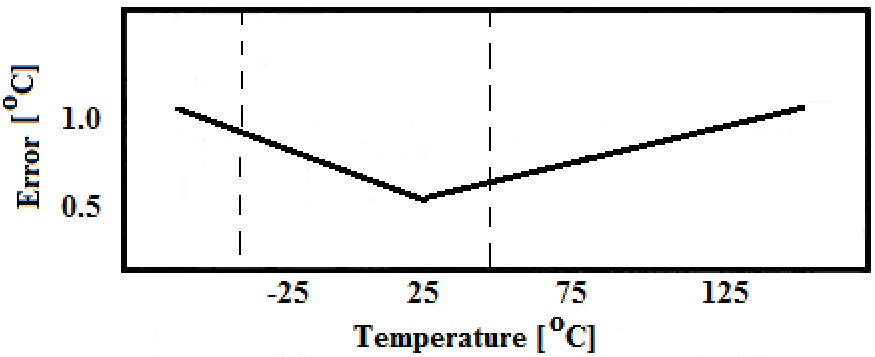

Figure 4.17: Temperature error as shown in the datasheet of the temperature sensor LM35. Between the two dashed lines is our region of interest.

Figure 4.18 shows a case study of the compensator where medium term drift due to temperature changes are taken over a period of four months. The measured SBP, and the result after compensating for the temperature related changes are shown in the figure. The simulated model took into account all the uncertainties in the electronics components to represent a practical study case. In the figure, three signals can be identified: The measured SBP including all the practical considerations and drifts, the practically compensated signal, which includes the uncertainty of the system components, and finally the theoretically compensated reference signal that is used as a gold standard to evaluate the algorithm. From the figure, the Root Mean Square Error (RMSE) between practically compensated SBP and the reference SBP was 0.1 mmHg, which implies that the similarity between them is high.

`

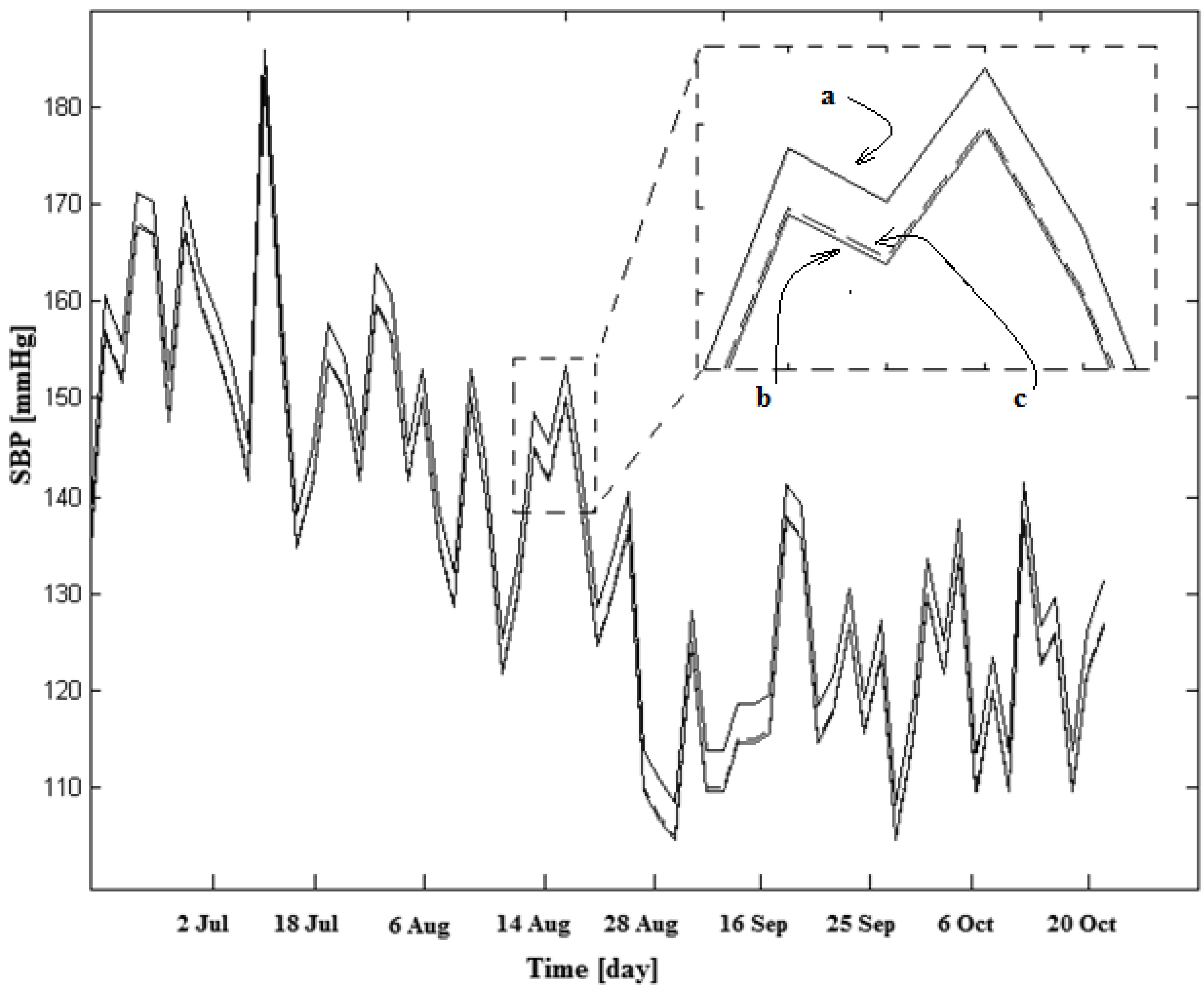

Figure 4.18: The proposed compensator performance over a period of four months. All three signals: (a) the measured SBP, (b) the practically compensated SBP, and (c) the reference SBP including compensation for temperature drift in other components.

`

4.5 Conclusions

The effect of temperature on non-invasive blood pressure monitors was studied based on analysis related to the drift in piezoresistive pressure sensors. The effect of humidity was ignored, as it is less critical in piezoresistive sensors (Zernike et al. 2013). The reason the study has focused on the sensor and not the other electronic components is that pressure sensors' drift is more critical and much higher than other measuring channel components (Sachenko et al. 2000). What is new in this study is that the focus is on the effect of temperature changes on the electronics itself, rather than on the human body. Most of the research in this area has been either concerned with temperature drift in invasive blood pressure systems or the effect of temperature on human physiology during blood pressure estimation (Van den Hurk et al. 2015; Kalia et al. 2014; Fujiwara et al. 1995). On the other hand, according to most pressure sensors' datasheets, the output is always going to be temperature dependent (Kim and Wise 1983).

The effect of temperature was studied through two different methods; a low level model based on semiconductor theory, where the temperature dependence model was derived. In that model, a clear relation between the gauge factor and the temperature was derived. Another important factor that was also discussed is the piezoresistive correction factor. This factor shows the effect of both temperature and doping concentration on the piezoresistive behaviour (Equation 4.10).

The second method to describe the temperature effect was based on user manuals, datasheets and some experimental data. The data obtained from the practical experiment shows clear evidence that the sensor is not compensated sufficiently as claimed in the datasheet. According to the datasheet (Equation 4.24), the sensor's output in the temperature range -5 ^{o}C to 85 ^{o}C and zero influencing pressure should not vary with temperature, which is not the case. Experimental data shows that the change in the sensor's output changes with temperature. For example, in the range of temperatures from 22 to -8^{o}C the change can reach up to 7.6%.

The results reported in this chapter show that there is drift in the pressure sensor due to temperature and that there is a need for a solution. The system was able to recover the SBP signal with a Root Mean Square Error (RMSE) of 0.1 mmHg measured between the compensated SBP and the reference SBP, which shows the high accuracy of the system.

`

The system proposed to monitor and compensate the drift using a microcontroller describes one solution to the problem that would boost the system accuracy and robustness under changing environmental conditions. The proposed automated compensator can be easily embedded in any blood pressure monitor. The user would not feel a difference in the operation of the device, and would not need to be concerned about any sort of manual calibration. The main stage in the proposed system is the microcontroller, whose main function is to control taking readings of both temperature and the sensor’s resistance, compare it with the data already stored in its LUT, and perform the compensation process according to that comparison.

`

CHAPTER 5: COMPENSATION FOR LONG TERM DRIFT DUE TO AGEING

5.1 Introduction

Another important factor to consider when dealing with sensors is the drift over time due to ageing. A study of the ageing of piezoresistive sensors was conducted by Scilingo et al. (2003), and took place over a period of one month. The results showed that the sensors' resistance per unit length increased by six times during that period. Although this increase may be exceptional, it demonstrates that ageing can have a strong effect on Piezoresistive sensors.

Ageing is considered critical, especially in mechanical based sensors (Schneider et al. 2008). Piezoresistive sensors generate an output (change in resistance) related to a specific input (pressure). This transduction is done through the sensor's diaphragm (Figure 5.1), which is the sensitive part of the sensor, and where changes in dimensions and resistance take place. The effect of ageing is in the form of degrading the elasticity of the diaphragm, which as a result causes changes in the system behaviour (Zernike et al 2013). Sinnadurai and Wilson (1982) defined ageing as a steady increase in the resistance at a specific rate influenced by various factors, including manufacturing origin and environment. According to their research, this increase in the resistance is proportional to the square-root of time (Sinnadurai and Wilson 1982).

Although ageing is considered a slow type of drift, home users of blood pressure monitors usually keep their monitors for years without calibrating them. Furthermore, from the literature review we performed, even clinical blood pressure monitors are not often calibrated, which necessitates having an automated compensator against drift due to ageing.

`

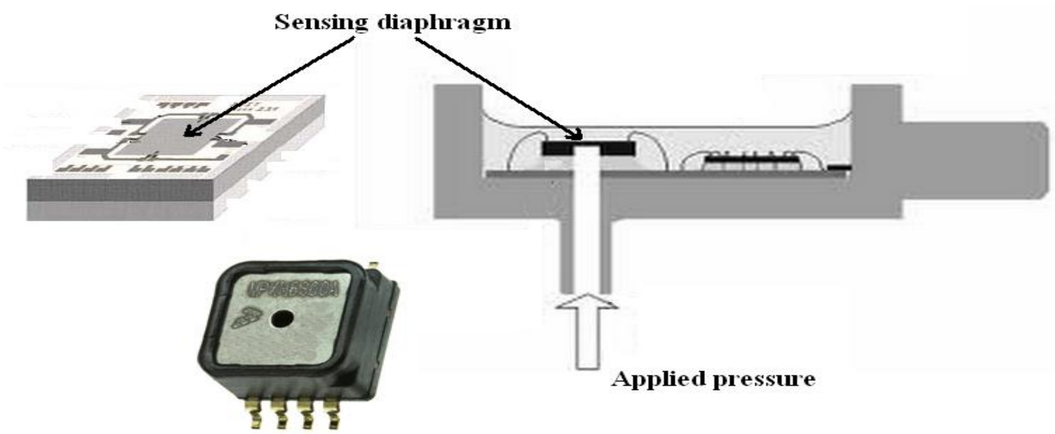

Figure 5.1: The diaphragm in a pressure sensor, which as a mechanical component, is particularly susceptible to ageing.

Semiconductor theory can explain how ageing affects piezoresistive sensors (Mladenovic et al. 1988; Suja et al. 2013). Starting with Equation 5.1, the resistivity can be expressed as:

$$\rho = \frac{1}{\sigma} \tag{5.1}$$

where, σ is the piezoresistor conductivity.

Now according to the definition of conductivity, it is possible also to rewrite Equation 5.1 as (Mladenovic et al. 1988):

$$\rho = \frac{1}{q\,\mu\,P} \tag{5.2}$$

where, $\mu$is the mobility, q is electron charge, and P is the carrier concentration of the piezoresistive material.

`

Furthermore, the resistance can be expressed as:

$$R = \frac{\rho L}{A} \tag{5.3}$$

where L is the length, A is the cross-section area and ρ is the resistivity.

From the above equation, it can be seen that the sensor's resistance depends on the structure dimensions A and L. Changing these dimensions results in changing the resistance. Looking back at Figure 5.1, the sensing mechanism in pizoresistive sensors is based on stretching and compressing the diaphragm, and with time, the sensor will start losing the flexibility to return to its original dimensions. Furthermore, the steady-state resistance will also change with ageing. Now, substituting Equation 5.3 into 5.2 leads to:

$$R = \frac{L}{q\ A\ \mu\ P} \tag{5.4}$$

Taking the partial derivative with respect to mobility and carrier concentration yields in

$$\Delta R = \frac{\partial R}{\partial \mu}\Delta\mu + \frac{\partial R}{\partial P}\Delta P \tag{5.5}$$

Now:

$$\Delta R = -\frac{1}{q\ A\ \mu\text{^}2\ P}\Delta\mu - \frac{1}{q\ A\ \mu\ P\text{^}2}\Delta P \tag{5.6}$$

`

Substituting Equation 5.4 into 5.6 yields:

$$\Delta R = -\frac{R}{\mu}\Delta\mu - \frac{R}{P}\Delta P \qquad (5.7)$$

Finally, we get the following relation:

$$\frac{\Delta R}{R} = -\frac{\Delta\mu}{\mu} - \frac{\Delta P}{P} \qquad (5.8)$$

According to this last equation (5.8), the change in a piezoresistive sensor's resistance can be defined in term of the changes in both the mobility and the carrier concentration.

Long term drift in sensor function due to ageing causes cracks to appear on the diaphragm (Zernike et al. 2013), which will affect the mobility, and so change its resistance due to a pressure. This would be seen as a 1/f noise, which will be responsible for changing the S/N ratio of the sensor (Santo et al. 2013; Dieme 2005), and/or changing the ΔR/R term according to Equation 5.8. According to Santo et al. (2013), such noise is mainly due to the fluctuations in the carrier-mobility. Kažukauska et al. (2010) also conducted a study to compare mobility between aged and non-aged semiconductor samples with respect to different temperatures, which showed that the mobility decreased with ageing.

In another study, Coleman (1984) described the behaviour of the sensor's resistance during its lifetime using accelerated ageing as a function of both time and temperature as:

$$\frac{\Delta R}{R_o} = \sum_{n=1}^{\infty}\left(a_i t^{n_i}\, e^{\frac{-E_i}{kBT}}\right) \qquad (5.9)$$

where a_i is the pre-exponential constant of the particular ageing mechanism, t is the time, T is the temperature in Kelvin, kB is Boltzmann's constant, E_i is the related activation energy (usually ranges from 0.1 – 0.5), and n_i is the time dependence constant (usually ranges from 0.3 – 0.5).

The importance of the previous equation (5.9) comes from the fact that it is now possible to investigate the amount of time required for a resistor to reach a certain change due to a specific temperature (using accelerated ageing process). Assuming that our $\Delta R/R_o$= C, where C is constant.

`

It is possible to derive the following formula (Coleman 1984):

$$t = \alpha e^{\frac{E}{KT}} \tag{5.10}$$

Drift in blood pressure devices is dominated by the drift of (piezoresistive) pressure sensors, while drift in other components, such as those making up the data acquisition systems (DAQ), is less significant compared to sensors (Sachenko et al. 2000). Even in invasive blood pressure measurements, where manufacturing standards are high, there is no device that can keep an accurate reading for more than a year (Saito et al. 2008). However, not much work has been done relating to the ageing of non-invasive blood pressure monitors, which makes it a fertile area of research.

5.2 Methods

The proposed system to compensate for the effects of ageing on the pressure sensor is based on the EMD method. One interesting feature of EMD is its ability to detect trends in time series. To illustrate this concept, a simulated signal is shown in Figure 5.2. This signal has two main frequency bands, a high frequency band representing the oscillation and a low frequency one representing the global increase in the time series. Applying the EMD sifting process, as shown in the figure, extracted the overall data trend.

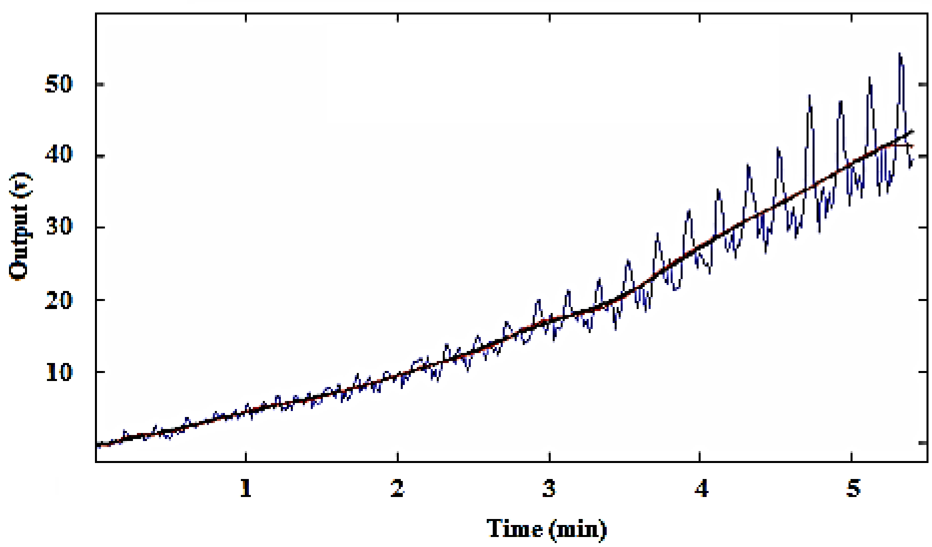

Figure 5.2: A simulated time series and its trend extracted using EMD. The trend is the monotone signal.

`

The definition of the "trend" as described by Alexandrov et al. (2012) is a form of smooth additive component, which holds information about the global changes in the signal under study. For a general time series x(t), the signal can be described in term of its main components; the trend, the short term cycles, and the error, as:

$$x(t) = T(t) + SD(t) + e(t) \tag{5.11}$$

where, T(t) is the trend, SD(t) is the short term drift and e(t) is the error.

Different approaches are used for trend detection. These include the model-based approach (MBA), Hodrick-Prescott filters, Wavelets, Singular spectrum analysis (SSA), and EMD (Alexandrov et al. 2012). In MBA, a stochastic time series model is built either as an autoregressive integrated moving average (ARIMA) model or as a state-space model. Hodrick-Prescott filters do not require any model specifications prior to applying them, which make them easier to implement than the MBA approach. Finally, SSA and wavelet-based methods require post-calibration in order to get good results.

The Hodrick-Prescott and MBA approaches have the disadvantage of sometimes generating sharp edges, as they tend to track dips in the signal. Wavelet trend detection approaches are also weak around sharp edges, and this will result in a distorted trend around sharp changes in the signal. Moreover, Wavelet approaches have the boundary effect, which requires additional adjustments at the end of the time series. SSA approaches are known for their need to be calibrated in advance in terms of specifying the window length (Alexandrov et al. 2012).

One of the advantages of using the EMD method over other approaches is that we are dealing with each signal at the level of its own components (or IMFs). This adds more flexibility to any approach based on it. (Huang et al. 1971). Decomposing the signal into its IMFs using the EMD approach can be summarized in the following equation:

$$f(x) = \sum_{n=1}^{m}(IMF_n) + T(t) \tag{5.12}$$

where T(t) is the signal trend, which also can be described as a monotone function free of oscillatory components (Alexandrov et al. 2012).

`

The trend finding algorithm using EMD is summarized in the following steps, where I_i is the signal under test.:

Loop1: Trend is not equal zero or not monotone

Loop2: I_i (t) has a non-negligible local mean

Local_maxima(t) = spline through local maxima of $I_i(t)$

Local_minima(t) = spline through local minima of $I_i(t)$

Avg(t) = (Local_maxima(t) + Local_minima(t)) /2

$I_i(t) = I_i(t) - Avg(t)$

end Loop2

$IMF_k(t) = I_i(t)$

Trend = Trend–IMF_k

end Loop1

5.2.1 Compensation system design

As shown in Figure 5.3 below, the compensation system for drift due to ageing starts with a pressure sensor resistance monitor. A data logger is used to save changes in the pressure sensor's resistance over time as a function of temperature, as our goal is to have all the information related to the sensor's behaviour over time, including short term, medium and long term drifts. As a result, the data logger will be used to compensate for the effects of temperature changes (Chapter 4) and changes due to ageing.

At a predefined time, when it is time for calibration, the system uses EMD to isolate the long-term trend due to ageing from other short term and medium term components at higher frequencies and saves the different components accordingly.

`

The generated compensation signal is with respect to the changes in the resistance over time, based on the following relation:

$$R_{measured} = R_o \pm \Delta R_{temp} \pm \Delta R_{ageing} \tag{5.13}$$

where R_o is the steady-state sensor`s resistance in the absence of applied pressure, $\Delta R_{temp}$ is change in the sensor`s resistance due to temperature and ΔR_{ageing} is the change in the sensor`s resistance due to ageing.

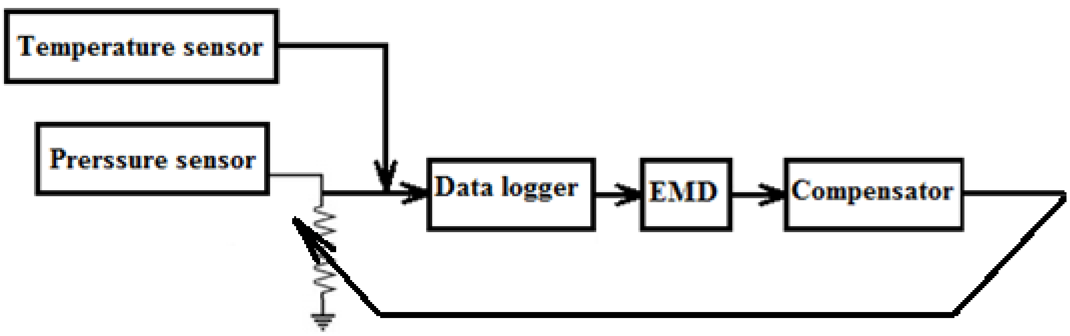

Figure 5.3: Overall proposed compensation system, where R_{sensor} is the piezoresistive resistance.

To design a resistance monitor system, a microcontroller (PIC 18f4550) was used with the signal conditioning circuit that is shown in Figure 5.4 below. From the figure, it can be seen that the proposed system is divided into five main blocks; A, B, C, D and E. Block A consists of the signal conditioning circuit, which was described in Chapter 4. Block B is the processing part of the system, where all signals are fed. This block will also have the ability to monitor the sensor’s resistance over time and save it on the attached SD (Secure Digital) card. The function of Block C is to measure the ambient temperature and send it to the microcontroller to be used as a reference. Block D is a stable voltage reference, described earlier in Chapter 4.

`

Finally, Block E represents the location where the LUT (lookup table) will be saved. The importance of this LUT comes from the fact that it will hold the sensor's resistance values over time. When it is time for calibration, the data collected will pass through an EMD stage that is responsible for extracting the trend. The EMD stage is implemented in Matlab, as shown in the figure, but can be embedded in the measurement device itself in the future.

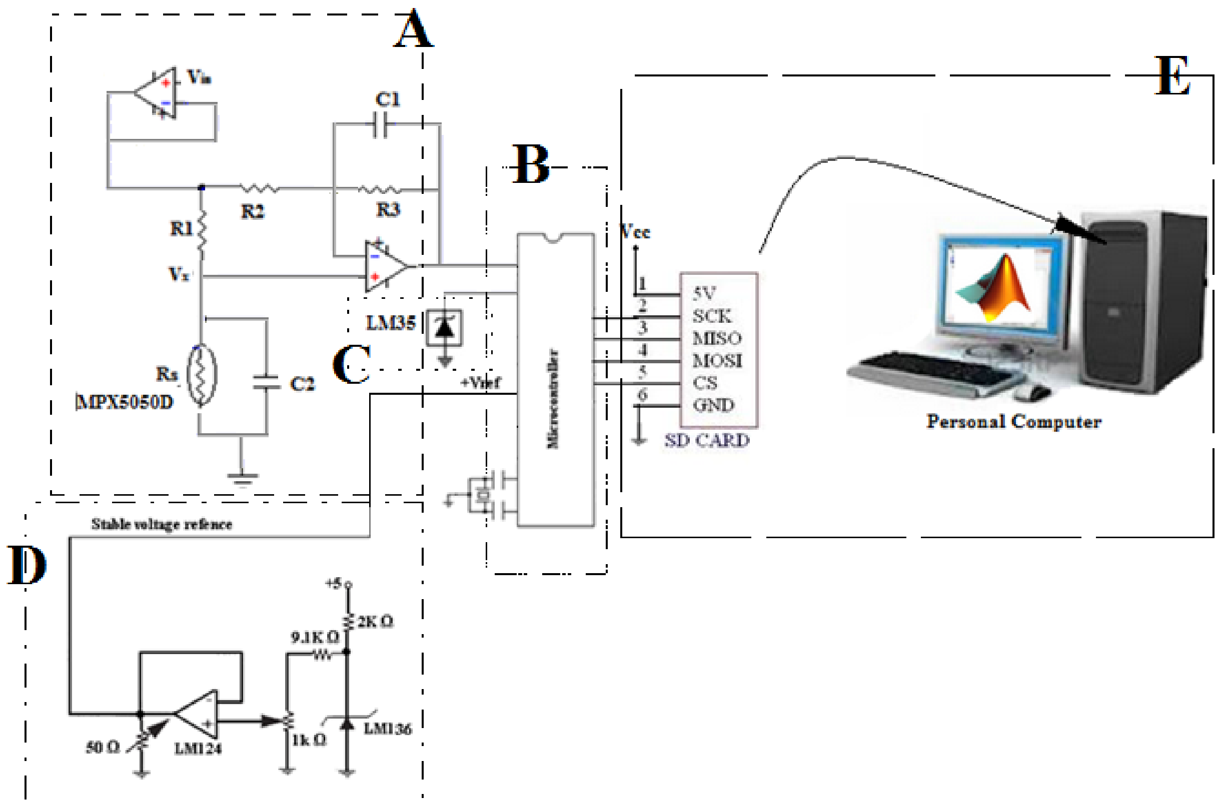

Figure 5.4: Piezoresistive pressure sensor resistance monitoring and signal conditioning circuit. The output is fed to the microcontroller ADC channel (analog to digital converter), saved into an LUT and then sent to the EMD algorithm in the PC. Note that, except for Block E, this is the same system used in Chapter 4 (shown in Figure 4.8).

`

5.2.2 System implementation

As described in the compensation system design section in Chapter 4 (Section 4.3), the compensation system is implemented in two simulation environments, one is the data logger system built using Proteus and the other is built using Matlab, where the extraction of the ageing trend is done. As shown in Figure 4.9 (Chapter 4), the first stage of the compensation system is implemented in Proteus Professional (Labcenter Electronics Ltd, North Yorkshire UK).A piezoresistive pressure sensor from the MPX family (Freescale Semiconductor, Texas, USA) is used as our pressure sensor.

The microcontroller used is PIC18f4550 (Microchip Technology Inc, Arizona USA). The ADC used to measure both the temperature and the piezoresistive sensor's resistance has an 8 bit resolution, with a voltage reference of 3V. A stable voltage reference circuit is designed based on the precision regulator, LM136-5.0, as suggested by Dawes (1998) and Jung (1994).

5.3 Experimental data

5.3.1 Piezoresistive sensor time drift

All papers published regarding ageing in piezoresistive sensors agree on the fact that the ageing process causes the resistance to increase with time. The amount of increase is considered linear but the slope of increase varies from one piezoresistive sensor to another (Santo et al. 2013; Andrei et al. 2004; Scilingo et al. 2003; Tankiewicz et al. 2001).

To simulate piezoresistive sensor drift due to ageing, data which represents a real case study from a paper published by Scilingo et al. (2003) was used. Figure 5.5 below shows the ageing trend of the piezoresistive sensor determined in that study and inset-graph shows the drift as a function of temperature for the same sensor.

`

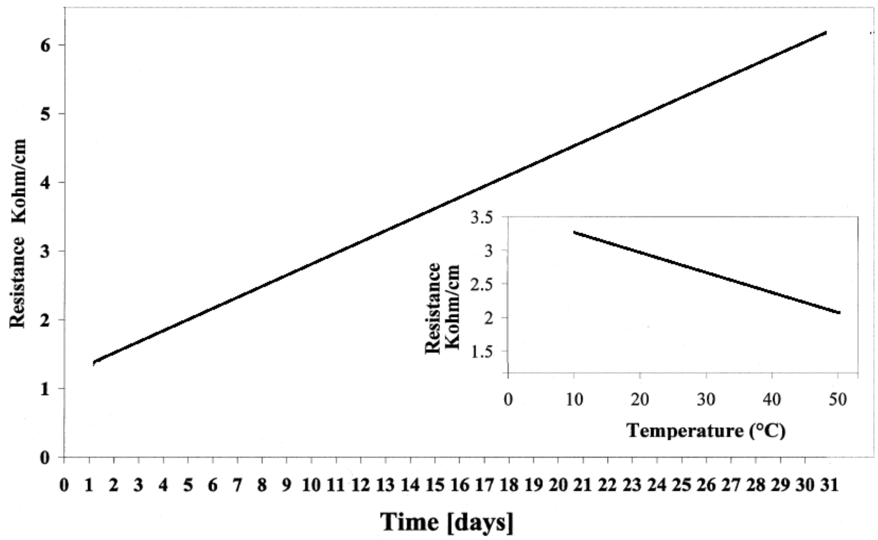

Figure 5.5: Drift due to piezoresistive sensor ageing. In the inset graph, the drift of the same sensoris shown, but as a function of temperature (Adapted from Scilingo et al. 2003).

According to figure above it can be seen that the changes in the resistance due to ageing can be written in the form of a ratio over the steady-state initial resistance as:

$$\Delta R/R_o = 3.36 \tag{5.14}$$

where ΔR is the difference in the measured resistance (R_{final} - R_o), and R_{final} is the final recorded resistance value due to ageing and R_o is the initial steady-state resistance of the piezoresistive sensor. The ageing behaviour s(Figure 5.5) can be described using the following equation:

$$R(t) = 0.159\, t + 1.26 \tag{5.15}$$

where the slope (0.159 kΩ/ cm. days) is a good indication of how fast the ageing process changes the sensor's resistance. After contacting the authors of Scilingo et al. (2003), it was clarified that this very large magnitude of ageing drift that they got was specific for the sensor that was used in their experiment. Nevertheless, the purpose in this part of the research is proving a concept related to compensation for drift and verifying the developed algorithm.

Achieving good results by applying the proposed algorithm on data similar to that obtained from Scilingo et al. (2003) would mean that it can work on any other set of ageing data. To illustrate how long term drift is compensated for, a simulated signal was generated based on ageing

`

information obtained from the literature (Scilingo et al. 2003). The signal under test, shown in Figure 5.6, has an increasing trend to represent the sensor's ageing. In addition, two types of disturbances were added, a medium frequency oscillatory signal, and white Gaussian noise which together represent possible short and medium term disturbances such as due to temperature changes.

The following steps were followed to generate the simulated signal shown in Figure 5.6:

- Ageing information from the journal paper published by Scilingo et al. (2003) was digitized.
- Temperature effect on the piezoresistive sensor used by Scilingo et al. (2003) was digitized.
- Periodic temperature changes were simulated.
- White noise was added.
- Between the fourth and the fifth month, the temperature effect was simulated to follow a different temperature/ageing schedule to help validate the proposed approach.

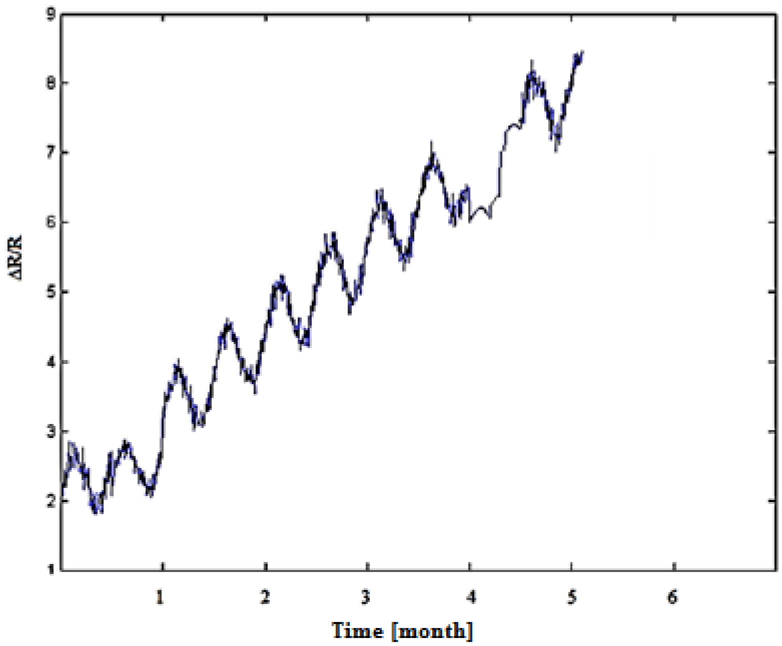

Figure 5.6: A simulated example representing data collected by the system described in Section 5.2 The signal contains long term (main trend), medium term drift, and short term disturbances.

`

To perform EMD, the signal undergoes the sifting process, where maxima and minima are used to generate the upper and lower envelopes (Huang et al. 1971). Figure 5.7 below shows a portion of the simulated signal with both the upper and lower envelopes.

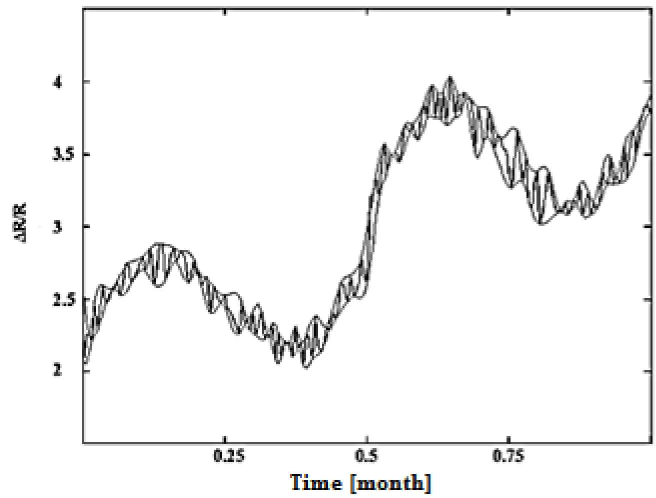

Figure 5.7: An example of the outcome of the sifting process in EMD, where both the upper and lower envelopes have been detected.

The final result from the applying the EMD trend detection approach is shown in Figure 5.8. From the graph, it can be seen how the trend signal was successfully extracted from the main signal. It is also important to notice how smooth the signal is, which agrees with the definition of a trend signal as described by Alexandrov et al. (2012).

`

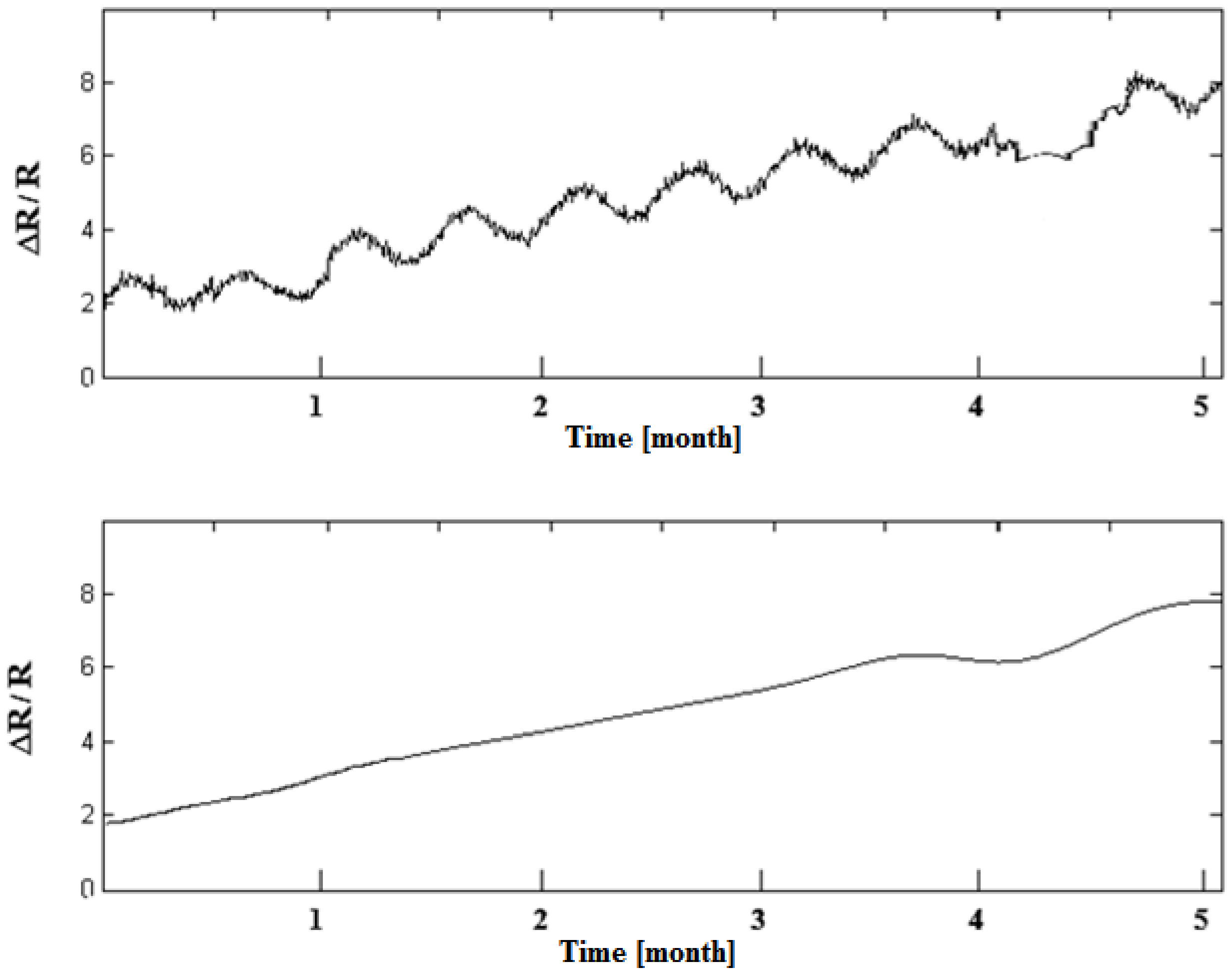

Figure 5.8: A simulated case showing the trend signal (bottom) obtained by applying the proposed approach on a simulated signal saved in the data logging system over a period of five months (top).

The compensation to ageing is conducted using the ability of EMD to extract trends. The process here is based on measuring the difference between the steady-state resistance value (start point) and the last one measured by the system. The second part in the compensation algorithm deals with the ageing drift, as shown in Figure 5.9. At any time when compensation is required, the system will automatically open the LUT and use interpolation to send an appropriate compensation signal to the MCU (Microcontroller unit). From the figure below, the difference in the sensor's resistance due to ageing is marked as ΔR/R, which can be easily transformed into a ΔR quantity, as will be shown later in this section using the fact that the quantity ΔR/R is the difference between the recorded value of the sensor's resistance when it is time for compensation and the initial value of the sensor's resistance R_o over R_o (Equation 5.15).

`

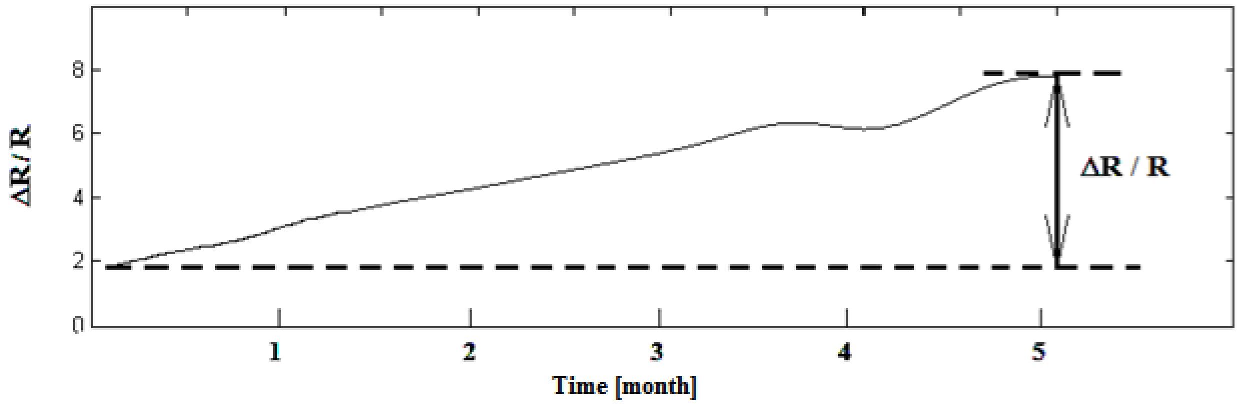

Figure 5.9: The amount of resistance, marked as ΔR/R, that the compensator should make up for is shown and marked on the trend signal, obtained by applying the EMD approach on a simulated signal as shown in Figure 5.8.

The proposed system is able to detect the changes in the sensor's resistance over time (ΔR), using the system shown in Figures 5.3 and 5.4.

Using Equation 5.14, it can be seen that the value of ΔR can be extracted when the value of R_o is known. Therefore, the system is fed a signal representing ΔR over time, as obtained from the paper (Scilingo et al. 2003), and the trend extraction algorithm will be applied. Finally, a compensation signal proportional to the drift is sent back to the microcontroller to adjust the reading accordingly.

5.3.2 Piezoresistive sensor time drift compensation

To simulate compensation for piezoresistive sensor drift due to ageing in non-invasive blood pressure measurement, data which represents the same trend of a real case study from a paper published by Scilingo et al. (2003) was used along with another set of data representing the SBP (systolic blood pressure) monitored over four months (Bersbach 2010). Figure 5.10 shows the SBP profile during the four months, and the obtained drift in the sensor's resistance due to ageing.

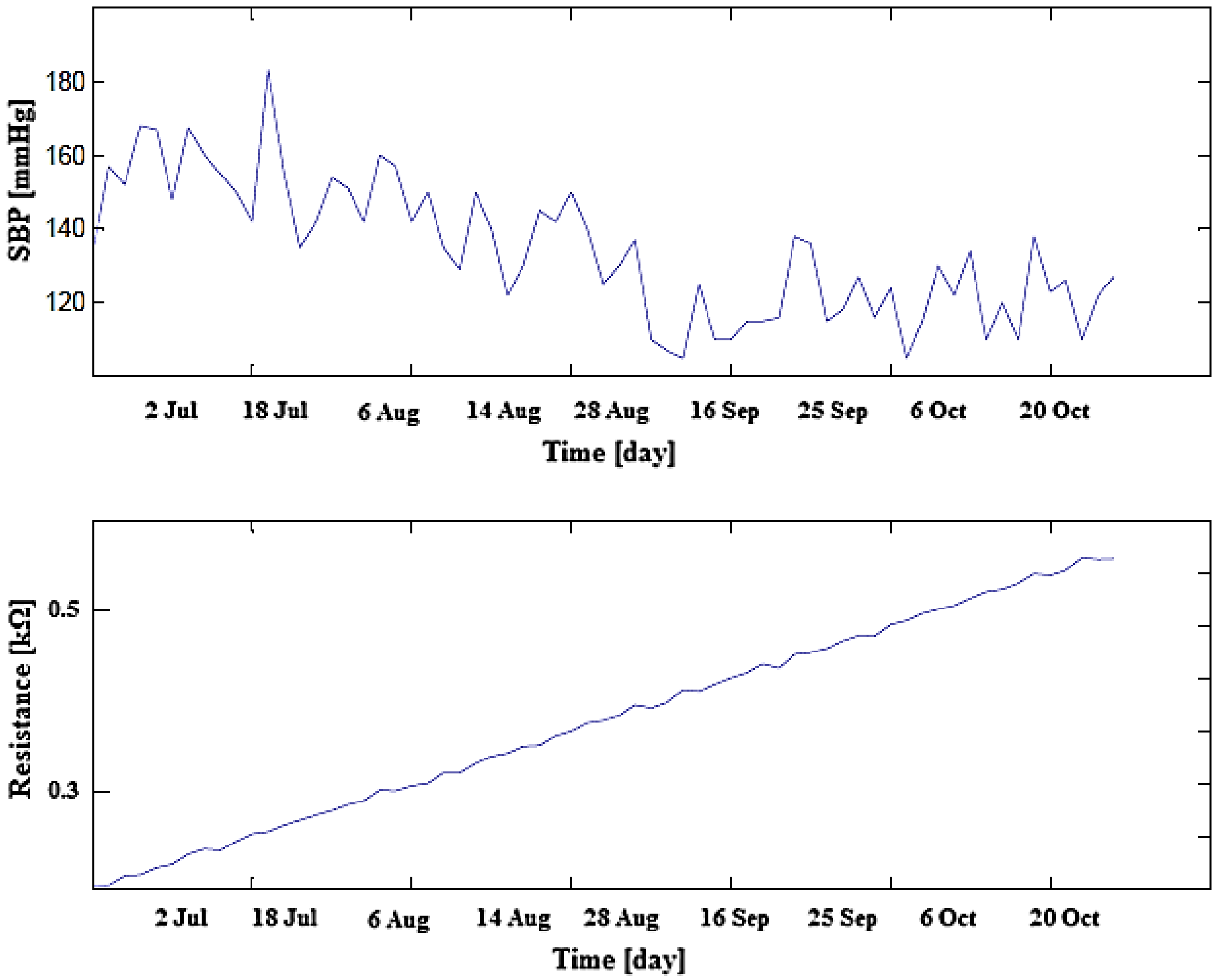

Figure 5.10: Case study to evaluate the effect of age-related drift on the SBP over four months. Top: SBP profile. Bottom: Resistance drift profile due to the sensor's ageing.

As explained in the Compensation system design (subsection 5.2.1), after the LUT has been generated and each time the device is used, a measurement of the sensor resistance is taken prior to cuff inflation. The measured resistance is stored in the device and incorporates the effect of ageing. The compensator will then extract the trend using EMD and so be able to adjust the output to compensate for effect of ageing during the on-line measurement.

`

At any time, the measured pressure will be a composition of resistance changes due to pressure, short/medium, and ageing drifts:

$$R_{measured} = R_o \pm \Delta\mathrm{R}_{pressure} \pm \Delta\mathrm{R}_{temp} \pm \Delta\mathrm{R}_{Ageing} \tag{5.16}$$

where R_o is the steady-state value for the sensor's resistance, $\Delta R_{pressure}$ is the change in the sensor's resistance due to the applied pressure, ΔR_{temp} is the change in the sensor's resistance due to temperature drifts, and ΔR_{ageing} is the changes in the sensor's resistance due to the long term drift.

In the same manner equation 5.16 can be expressed as voltage quantities:

$$V_{measured} = V_o \pm \Delta\mathrm{V}_{pressure} \pm \Delta\mathrm{V}_{temp} \pm \Delta\mathrm{V}_{Ageing} \tag{5.17}$$

where V_o is the steady-state value for the voltage across the sensor's resistance, $\Delta V_{pressure}$ is the voltage change as a result of the change in the sensor's resistance due to the applied pressure, ΔV_{temp} is the voltage change due to the change in the sensor's resistance because of the temperature effect, and ΔV_{ageing} is the voltage change due to the sensor ageing.

`

Applying the proposed drift form Figure 5.10 on the SBP profile results in the new shifted SBP profile shown in Figure 5.11.

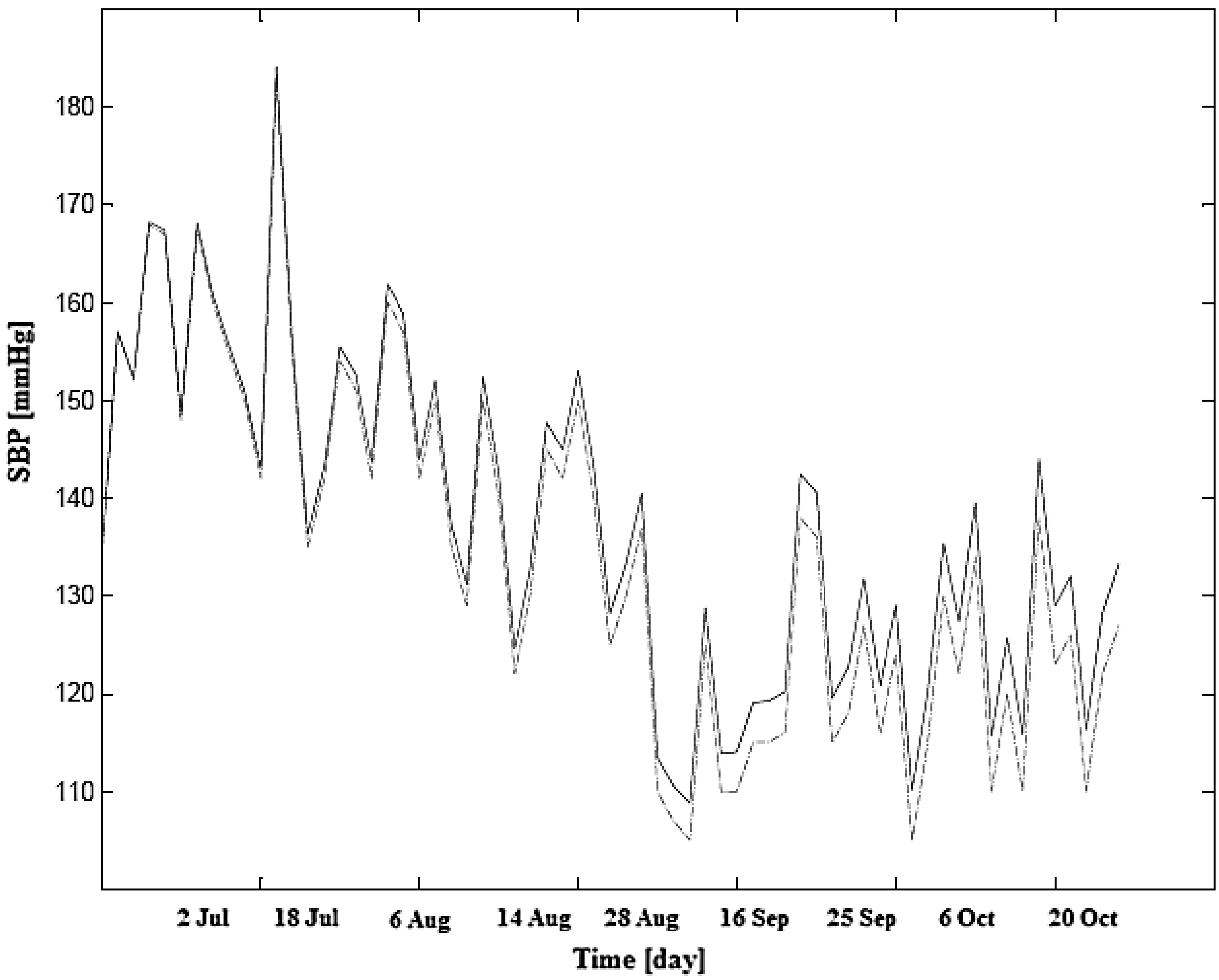

Figure 5.11: Case study showing the effect of long term drift on the proposed SBP profile over a period of four months. Dashed line: The original systolic blood pressure (SBP) profile. Solid line: The shifted SBP profile due to ageing.

Now for the ageing problem, the sensor will be monitored while the device is offThus, Equation 5.16 can be reduced to the following one (Equation 5.18):

$$R_{measured} = R_o \ \pm \Delta\mathrm{R}_{temp} \pm \Delta\mathrm{R}_{Ageing} \quad (5.18)$$

where R_o is the steady-state value for the sensor's resistance, and ΔR_{ageing} is the change in the sensor's resistance due to the long term drift.

`

The profile of the changes in the piezoresistive sensor's resistance will be stored in an LUT over time, until it is the time to compensate. The importance of this LUT comes from the fact that it will hold the sensor's resistance values over time. When it is time for calibration, the data collected passes through an EMD stage that is responsible for extracting the trend. The EMD stage is currently implemented in Matlab, but can be embedded in the measurement device itself in the future. Figure 5.12 shows the result of the trend extraction process.

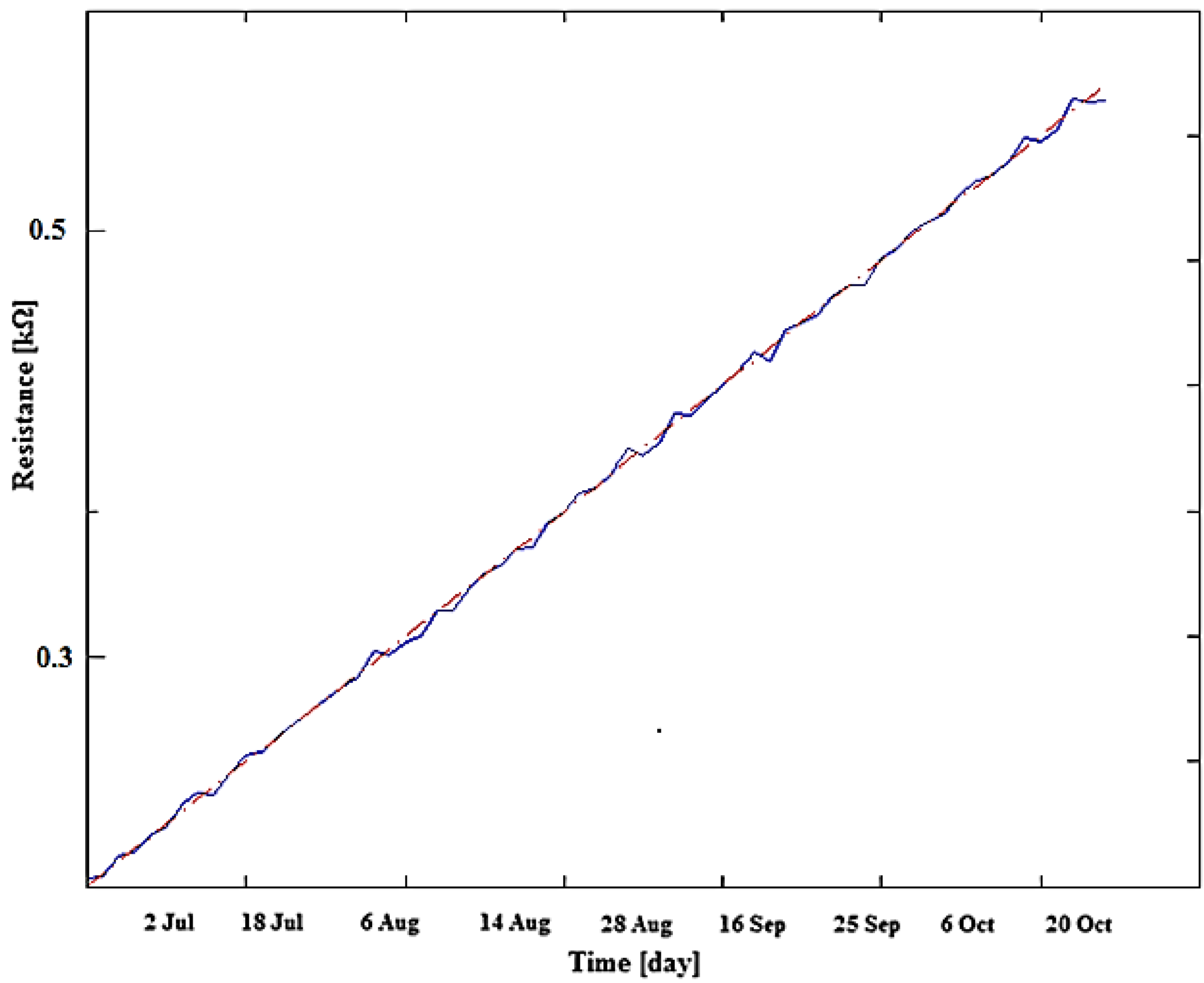

Figure 5.12: Case study showing the proposed EMD based trend extractor performance against long term drift over a period of four months. Solid line: The sensor's resistance as it is stored in the LUT. Dashed line: The extracted trend.

`

To evaluate the performance of the proposed stage, Figure 5.13 shows a comparison between the true drift in the sensor's resistance and the trend extracted by the compensator using the EMD algorithm. . As can be seen in the figure, the percentage difference between the trend extracted using the proposed algorithm and the reference trend is 0.1%, which indicates how reliable this approach is.

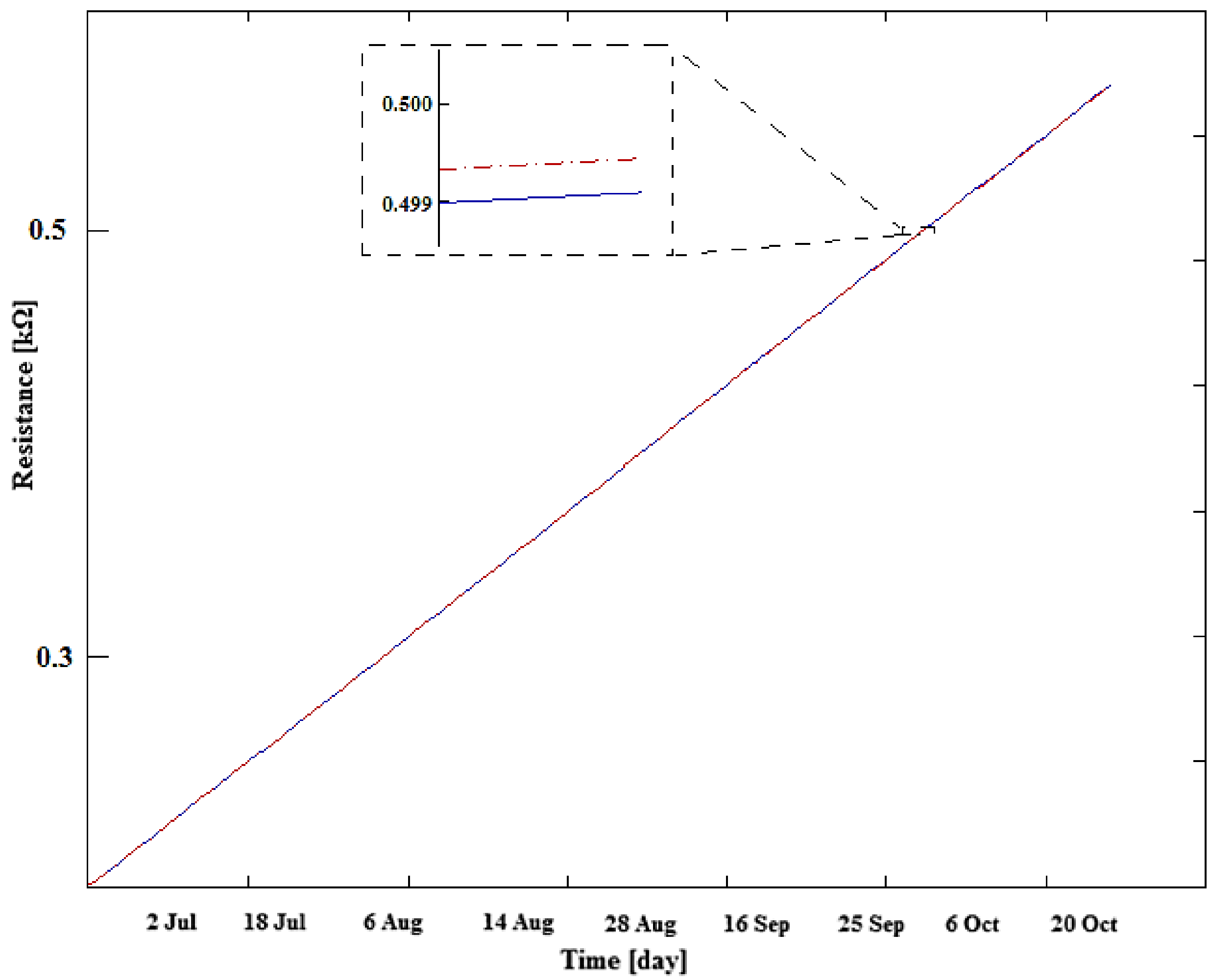

Figure 5.13: The performance of the proposed trend extractor in comparison with the true drift of the sensor's resistance over a period of four months. Solid line: The true trend of the sensor's resistance ageing profile. Dashed line: The trend extracted using EMD.

`

And finally Figure 5.14 below illustrates the compensation performance on the SBP profile over the testing time period. The high accuracy of EMD in extracting the trend according to the previous figure (Figure 5.13) resulted in almost identical compensated and reference SBP profile signals.

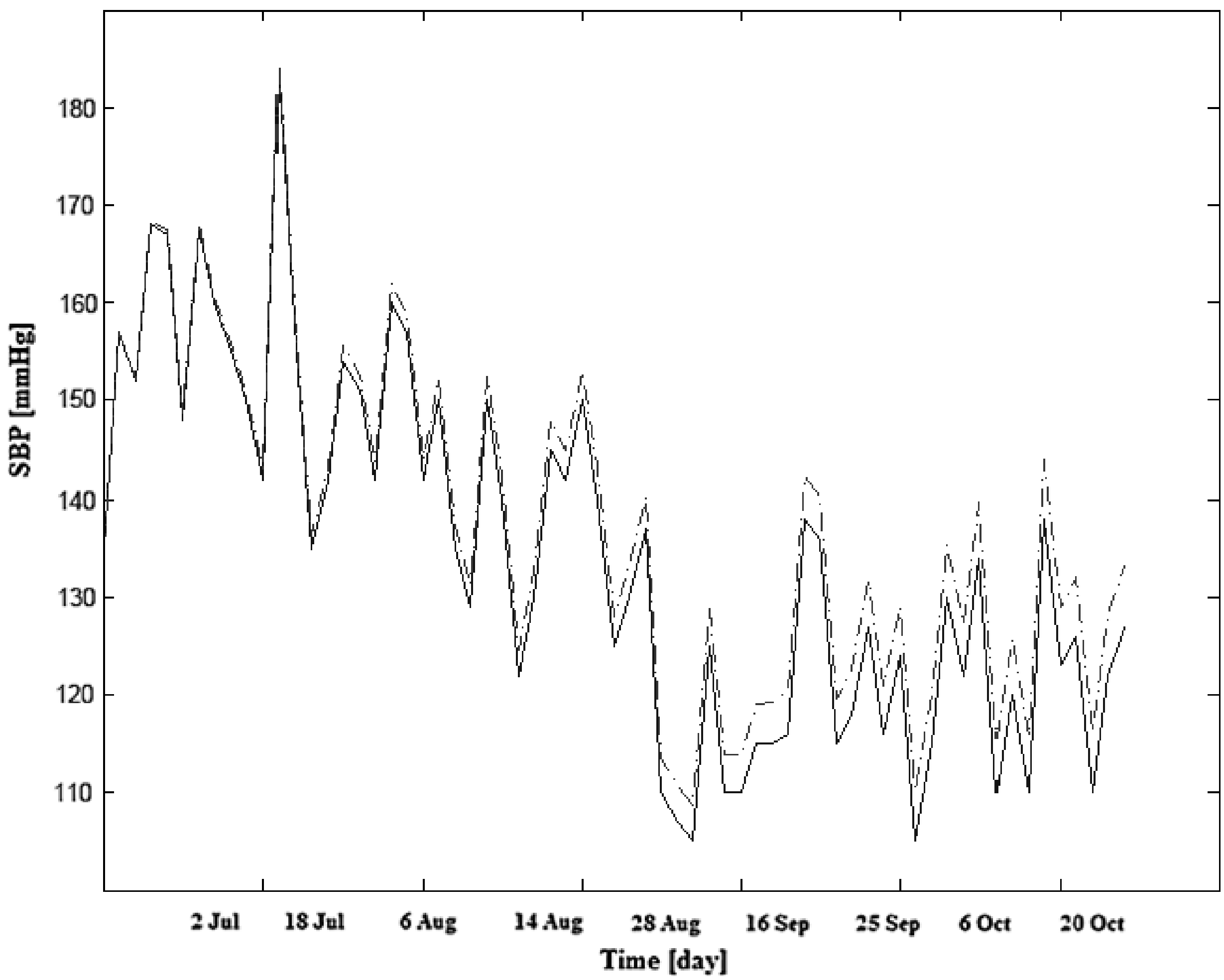

Figure 5.14: The performance of the proposed trend extractor in comparison with the SBP profile over the testing time period. Solid line: The compensated SBP profile. Dashed line: The drifted SBP profile under test. Note that the reference SBP profile is practically identical to the compensated SBP profile and is not shown in the figure.

`

5.4 Discussion and Conclusions

In this chapter, the effect of ageing on piezoresistive sensors was studied. The effect of this long term drift was demonstrated using semiconductor theory. From the theory, a model based on the sensor's mobility was derived (Equation 5.8). According to Zernike et al. (2013), ageing causes cracks to appear on the diaphragm, the sensing element, which affects the internal carrier mobility of the sensor. With time, this diaphragm will age, and the effect of this phenomenon on the sensor's behaviour cannot be ignored.

Studying the mobility is important because it is considered to be a factor that changes the sensor's resistance due to an applied pressure. Experimental data from several journal papers all supported the phenomenon and some provided measurements of the drift due to ageing under different operating conditions (Santo et al. 2013; Andrei et al. 2004; Scilingo et al. 2003; Tankiewicz et al. 2001).

The embedded system introduced in this chapter to monitor the sensor's resistance online and compensate for any changes was designed using both Proteus Professional and Matlab. In the environment provided by Proteus Professional, the microcontroller stage was implemented to act as a data-logger. The Matlab system performs the compensation, where an EMD trend extractor was implemented. EMD is used to analyze the sensor's resistance signal because it can lead to an IMF representing the signal trend.

With the help of other research works in the field, the sensor behaviour was simulated based on previously collected experimental data, as shown in Figure 5.10. Applying the EMD approach to the simulated sensor's ageing behaviour resulted in extracting the trend signal with an accuracy of about 99%, as illustrated in Figure 5.13. Having the trend data and using Equation 5.17, the system is able to isolate the real value of R_o from the drifted aged value. The system is then able to adjust the values for the changes in the sensor's resistance accordingly.

`

CHAPTER 6: CONCLUSIONS AND FUTURE WORK

Blood pressure (BP) is considered one of the most important indicators of cardiovascular health. The risk of having strokes and other cardiovascular diseases, heart failure, kidney disease, and eye pathologies increase significantly with high BP.

With the large number of automated BP monitors available on the market, more and more people have decided to own a home monitor, as it does not require advanced skills to operate. Consequently, the need of a reliable blood pressure monitor has also increased. When it comes to home users, this sector includes educated as well as uneducated patients. The term "educated" in this context does not necessarily indicate a university degree, but is related more towards a health education, an awareness and a sense of what should and what should not be done with home health devices.

From the literature, it was shown that with all the different sources of errors: motion artifact, environmental drift, and ageing drift, the risk of obtaining an inaccurate BP estimation is high. An error of 5 mmHg is so serious that it can be responsible for doubling or halving number of patients diagnosed with hypertension. Thus, there is a need to have a device that can monitor and handle these sources of error. Moreover, many of the current existing BP monitors do not even consider displaying an error message in case of an abnormal condition causing an inaccurate estimation.

This work is novel in that it shines a light on a very important problem that many patients might be dealing with without even noticing. Surprisingly, to date, there is no standard for validating the performance of a BP device under such operating conditions. Moreover, a technology to deal with the effects of even simple movements during a measurement, basic temperature changes, or ageing is not yet embedded in commonly used blood pressure monitors. From the literature review that was done, it is seen that the publications in this area have not satisfactorily tackled this problem. This work, therefore, fills a gap in this area and adds new ideas and solutions towards a more reliable BP monitor.

`

This thesis aimed to solve these problems by a proposed stage that is suitable to be integrated into the device. The main function of this stage is to both monitor and resolve the artifact or drift as soon as it appears.

In Chapters 3-5, methods to deal with disturbances that affect non-invasive blood pressure measurements were proposed in a way that has not been previously suggested. The methods involve introducing new hardware to monitor relevant signals, and new algorithms that can be incorporated into firmware.

6.1 Summary of results

The disturbances that were studied, transient motion artifacts and vibrations, temperature drift, and ageing, occur at different time scales. Starting with vibrations in Chapter 3, a new EMD-based approach, referred to as intrinsic Mode Functions Collector (IMFC), was compared with a conventional method using different types of vibration signals in the range of 5 – 25 Hz and an acceleration strength of 0.05 and 0.15 g. The range was determined based on two conditions; first, the limits set by the international standard ISO 2631-1:1997, which requires a vibration frequency of less than 80 Hz in any vibration experiment with humans. The second condition was to focus on the range of frequencies that is actually encountered in moving vehicles, which is in the range of 10 – 25 Hz and an acceleration of 0.1 g to 0.2 g. The time intervals of the motion were detected using an accelerometer fixed on the cuff.

The performance of the proposed IMFC method was assessed using the measures ME, MAE and SDE in reference to measurements from an Omron monitor. The ME, MAE, and SDE obtained with the proposed method were -0.6, 0.8 and 1 mmHg in the case of SBP, and -0.4, 1.1, and 1.5 mmHg in the case of DBP, while the same measures obtained by the conventional method were 1.7, 3.1, and 3.8 mmHg in the case of SBP and 1.9, 3.5, and 5.5 mmHg in the case of DBP. Bland-Altman analysis also showed narrower limits of agreement with the reference method, compared to the conventional method.

`

Another type of motion artifacts, due to transient motions of fingers and arm, was also studied. The effect of these artifacts was suppressed using another EMD-based approach, referred to as Intrinsic Mode Functions Selective Analyzer (IMFSA). Results from the proposed IMFSA method and the conventional method were compared to reference measurements obtained using the Omron monitor. The ME, MAE, and SDE obtained with the proposed method were 0.3, 2.4, and 3.1 mmHg in the case of SBP, and 0, 2.4, and 2.9 mmHg in the case of DBP, while the same measures obtained by the conventional method were -0.9, 9.4, and 11.6 mmHg in the case of SBP and 3.2, 5.3, and 8.7 mmHg in the case of DBP. Bland-Altman analysis also supported the improvement obtained with the new approach. As a result, the proposed method can be used to improve the reliability of blood pressure measurements in challenging environments that lead to motion artifacts.

In Chapter 4, a method developed to monitor and compensate for the temperature effect on piezoresistive sensors was discussed. Experimental results show that drift due to temperature occurs, and that the level of drift is beyond what is expressed in datasheets. A new hardware system to compensate for this drift based on a temperature sensor, and a microcontroller was introduced. The novelty in this chapter is that the focus is on the effect of temperature changes on the electronics itself, rather than on the human body. This focus is still a fertile area for research.

Furthermore, this chapter introduced the effect of temperature through two different models; a low level model, based on semiconductor theory and another high level model, based on user manuals, datasheets, and some experimental data. In the first model, the temperature dependence model was derived. In addition, a clear relation between the gauge factor and the temperature was generated (Equation 4.9).Another important factor that was also discussed in this model is the piezoresistive correction factor. This factor, according to Equation 4.10, describes the effect of both temperature and doping concentration on the piezoresistive behaviour.

`

The second model to describe the temperature effect, as explained above, was built using data from the literature, datasheets and user manuals. A pilot study to study the temperature effect on piezoresitors shows clear evidence that the sensor is not sufficiently robust against temperature changes as claimed in the datasheet (Equation 4.24). Experimental data that we obtained shows that the change in the sensor's output changes with temperature. For example, in the range of temperatures from 22 to -8^{o}C it can reach up to 7.6%.

To validate the model, a compensation system was implemented in a professional electronic simulation software environment called "Proteus Professional". An advantage of using this software is that it provides accurate simulations of a large variety of different sensors, actuators, displays, and microcontrollers used in the industry. Furthermore, it provides a professional environment for embedded system design and implementation, with the ability to load code to the microcontroller for testing purposes. (Figure 4.9).

The simulation took into account the temperature dependency of the components and the accuracy of the temperature sensor that was used (Figure 4.17). The results reported in this chapter support the existence of drift in the pressure sensor due to temperature and the need for a solution. The system proposed to monitor and compensate for this drift resulted in the very low Root Mean Square Error (RMSE) of 0.1 mmHg between the compensated SBP and the reference SBP (Figure 4.18). Therefore, the proposed system can be considered one solution that would substantially improve the system accuracy and robustness under changing environmental conditions.

Chapter 5 discussed another important factor that is often not considered in the field of non-invasive blood pressure measurements, and this is sensor ageing or time drift. Where ageing has been studied, the point of view has been to monitor the phenomenon rather than compensate for it. The first part in that chapter discussed the theory behind sensor ageing, which was the starting point towards a better system design. The model in the first part was studied through semiconductor theory, which gives us the ability to understand the drift based on the study of the internal structure of the sensor (Equations 5.8 and 5.9).

`

Long term drift causes cracks to appear in the diaphragm, the sensing element, which in turn affects the internal carrier mobility of the sensor. Thus, the effect of this phenomenon on the sensor's behaviour cannot be ignored. Studying the mobility is important because it is considered to be a factor that changes the sensor's resistance due to an applied pressure (Equations 5.8 and 5.13).Later in the chapter, a method based on the EMD algorithm was used to extract the slow change (trend) due to ageing. The EMD approach was chosen because of its ability to detect signals trends (Figure 5.8). A model based on real experimental data from the literature was implemented in Proteus Professional to validate the approach.

The proposed system in this chapter is designed to monitor the sensor's resistance online and compensate for any changes. In the environment provided by Proteus Professional, the microcontroller stage was implemented to act as a data-logger. In addition, the Matlab system performs the compensation, where an EMD based trend extractor is implemented (Section 5.2).

With the help of other research works in the field, the sensor behaviour was simulated, as illustrated in Figure 5.10. Applying the EMD approach to the simulated sensor's ageing behaviour resulted in accurately extracting the trend signal (Figure 5.13 and 5.14) with an agreement that reaches 99.9%. Furthermore, the simulated system is able compensate for changes in the sensor's resistance changes based on Equation 5.17, where the compensation amount is proportional to the final value of the drift.

It should be emphasized, however, that all the methods described in this thesis dealt with defined external sources of error and do not compensate for errors inherent in the oscillometric algorithm itself, which can reach several mmHg, nor do they compensate for uncertainty due to natural variation in blood pressure, which can reach 20 mmHg over short time intervals. Other methods are needed to reduce the measurement errors and uncertainty due to these factors.

`

6.2 Future work

The following describes several future lines of work that would be useful:

- The next steps will include embedding the proposed algorithms on an MCU, so that the system will be able to perform as an integrated self-contained embedded system that can achieve the required calibration steps without the utilization of Matlab.
- The selection of motion artifact test cases were limited to motions that will not affect vital signals. More severe cases of motion artifacts that affect vital signals can be tested. Future expansion of the research will also involve a larger sample of healthy participants and patients.The data granularity in the LUT of the medium term drift compensator was chosen to validate the algorithm. In the future, the necessary granularity of the LUT will be explored in more detail. In addition, the model for compensating both medium term and long term drift did not consider the interaction between the temperature and ageing. Future work could include a multidimensional table to deal with such cases.The model for temperature compensation considered a linear relation between sensor's resistance and the temperature for the purpose of validating the algorithm. In the future, more investigation will be done towards determining a more exact model of this behaviour.The work can be expanded to use machine learning algorithms, such as Artificial Neural Networks (ANNs), Simulated Annealing (SA), and Genetic Algorithm (GA) to work side by side with the EMD, so that the compensation process will be based on a learning process. Future experimental work can involve using invasive intra-arterial methods to obtain more accurate reference measurements for the purpose of validation, measurement with various patient populations, and expanding the study to include more extreme motion artifacts, such as those associated with physical activity.
- The reported results do not include other contributors to measurement errors such as Oscillometric method errors, cuff placement, cuff size, and cuff ageing. Future investigation could include those sources of error, to further improve robustness of the BP monitor.

`

REFERENCES

B. Abdelaziz, K. Fouad, and S. Kemouche, “The effect of temperature and doping level on the characteristics of piezoresistive pressure sensor”, Journal of Sensor Technology, vol. 4, no. 2, pp. 4-6, 2014.

H. N. Abderahman, H. R. Dajani, M. Bolic, V. Z. Groza “An integrated system to improve robustness of non-invasive blood pressure estimation with motion artifacts”, Proceedings of the IEEE Engineering in Medicine and Biology Conference, 2015.

J. Abdul Sukor, S. J. Redmond, G. S. Chan and N. H. Lovel, “Signal quality measures for unsupervised blood pressure measurement”, Physiological Measurement, vol. 33, no. 3, pp. 465–486 ,2012.

A&D Medical, “Owner’s Manual: Advanced Manual Inflate - Blood Pressure Monitor”, San Jose, CA, 2007, pp. 1-24.

Advanced Anesthesia Specialists, “The blood pressure can of worms – Part II”, AAS LLC white papers, 2013. Available from: https://advancedanesthesiaspecialists.wordpress.com [Sep 2015]

I. Ahmad, S. Qayyum, R. Qamar and M. Chagani, “Sphygmomanometers in clinical use: are they reliable?”, Pakistan heart journal, vol. 42, no. 1, pp. 27-30, 2009.

S. Ahmad, S. Chen, K. Soueidan, I. Batkin, M. Bolic, H. Dajani, V. Groza, “Electrocardiogram-assisted blood pressure estimation”, IEEE Transactions on Biomedical Engineering, vol. 59, no. 3, pp. 608-626, 2012.

`

L. Aleksandrov, M. Lanthier, A. Maheshwari, and J.R. Sack "Approximation algorithms for geometric shortest path problems", In 32nd ACM Symposium on Theory of Computing, pp. 286-295, 2000.

T. Alexandrov, S. Bianconcini, E. B. Dagum, P. Maass, and T. S. McElroy, "A review of some modern approaches to the problem of trend extraction", Econometric Reviews, vol. 31, no. 6, pp. 593-624, 2012.

D. G. Altman and J. M. Bland, "Measurement in medicine: the analysis of method comparison studies", Statistician, vol. 8, no. 2, pp. 307–319, 1983.

J. N. Amoore, "Extracting oscillometric pulses from the cuff pressure: Does it affect the pressures determined by oscillometric blood pressure monitors?", Blood Pressure Monitoring, vol. 11, no. 5, pp. 269-279, 2006.

J. N. Amoore, "Oscillometric sphygmomanometers: a critical appraisal of current technology", Blood Pressure Monitoring, vol. 17, no. 2, pp.80–88, 2012.

S. Ando, "What does a perfect blood pressure meter look like from a clinician point of view?" Instrumentation and Measurement, vol. 17, no. 3, pp.15 – 20, 2014.

A. Andrei, C. Malhaire, S. Brida, and D. Barbier, "Reliability study of AlTi/TiW, polysilicon and ohmic contacts for piezoresistive pressure sensors applications", Proceedings of IEEEon Sensors, 2004., vol. 3, pp. 1125-1128, 2004.

Automatic Blood Pressure Monitor With ComFitTM Cuff: Model HEM-790IT, Omron Healthcare Inc., Bannockburn, IL 60015, 2006, pp. 4-10.

E. Balestrieri and S. Rapuano, "Instruments and methods for calibration of oscillometric blood pressure measurement devices", IEEE Transactions on Instrumentation and Measurement, vol. 59, no. 9, pp. 2391, 2010.

`

E. Balestrieri, P. Daponte and S. Rapuano, “Towards accurate NIBP simulators: Manufacturers’ and researchers’ contributions”, IEEE International Symposiumon Medical Measurements and Applications Proceedings, pp. 91-96, 2013.

A. Ball-llovera, “An experience in implementing the Oscillometric algorithm for the non-invasive determination of human blood pressure”, Proceeding of the 25th Annual International Conference of the IEEE Engineering in Medicine and Biology Society, vol. 4, pp. 3173 – 3175, 2003.

P. MS. Bartlett, “Periodogram analysis and continuous spectra”, Biometrika, vol. 37, no. 1/2, pp. 1-16, 1950.

B. M. Battista, A. D. Addison, and C. Knapp, “Empirical mode decomposition operator for dewowing GPR data”, Journal of Environmental and Engineering Geophysics, vol. 14, no. 4, pp. 163-169, 2009.

S. Baykut, S. and T. Akgül, “Multiscale zero-crossing statistics of intrinsic mode functions for white Gaussian noise”, IEEE Conference in European Signal Processing, pp. 135 – 138, 2010.

S. Beclin, S. Brida, S. Metivet, P. Martins and O. Stojanovic, “High sensitivity piezoresistive silicon microphone for aerospace applications”, 5th ESA Micro and Nano Technologies round Table, Noordwijik, 2005.

D. Benitez, P. A. Gaydecki, A. Zaidi and A.P. Fitzpatrick, “The use of the Hilbert transform in ECG signal analysis”, Computers in Biology and Medicine, vol. 31, no. 5, pp.399-406, 2001.

R. G. Bennett and L. A. Taylor, “Arrhythmia compensation of a predictive non-invasive blood pressure algorithm”, Proceedings of Annual International Conference of the IEEE Engineering in Medicine and Biology Society, vol. 13, no. 5, pp. 2114-5, 1991.

P. Bersbach, “The Element of Time”, 2010 [Online]

Available from: www.sixsigmatrainingconsulting.com/tag/i-chart/. [Accessed: 14- Jan- 2015].

`

Biomedical Engineering Team, "ANSI/AAMI SP10 Report: Biosign White Papers", Biosign Technologies Inc, USA, 2011. Available from: www. alqaemhealthcare.com [Apr 11 2016].

A. Birch and S. L. Morris, “Do the Finapres and Colin radial artery tonometer measure the same blood pressure changes following deflation of thigh cuffs Physiology”, Physiological Measurement, vol. 24, no. 2, pp. 653-60, 2003.

J. M. Bland and D. G. Altman, “Statistical methods for assessing agreement between two methods of clinical measurement,” Lancet, vol. 1, no. 8476, pp. 307–310, 1986.

D. Boutana, M. Benidir, and B. Barkat, “Denoising and characterization of heart sound signals using optimal intrinsic mode functions”, In Proceedings of the 4th International Symposium on Applied Sciences in Biomedical and Communication Technologies, ACM, pp. 26-31, 2011.

BpTRU Operator’s Manual, BpTRUTM Medical Devices, BpTRU medical devices, Coquitlam, BC, Canada, 2007, pp.1-14.

M. Bruins, A. van Belkum and A. Bos, “The use of electronic nose devices in clinical microbiology” in The Role of New Technologies in Medical Microbiological Research and Diagnosis, J. P. Hays and W. B. Van Leeuwen, USA: Bentham Science Publishers, 2012, pp. 90-101.

CAS Medical Systems Inc, “Motion artifact testing and performance”, white papers, USA, 2010. Available from: http://www.casmed.com [Sep 22 2015]

V. Casey, P. Grace and M. Clarke-Moloney, “Pressure measurement at biomedical interfaces”, Applied Biomedical Engineering, INTECH Open Access Publisher, pp.244-264, 2011.

L-P. Chao, C-W. Lin, and Y-D. Lau, “A study on the effects of humidity, temperature, and pressure sensor on the piezoresistive film co-structure”, Proceedings of the 2005 International Conference on MEMS, NANO and Smart Systems, pp. 443 – 446, 2005.

`

S. Charbonnier, J. P. Siche and R. Vancura, “On line detection of movement artifacts to improve ambulatory blood pressure monitoring”, Instrumentation and Measurement Technology Conference,vol. 2, pp. 693-700, 2000.

M. Chavko, W. A. Koller, W. K. Prusaczyk and R. M. McCarron, “Measurement of blast wave by a miniature fiber optic pressure transducer in the rat brain”, Journal of Neuroscience Methods, vol. 159, no. 2, pp. 277–281, 2007.

Q. Chen, N. Huang, S. Riemenschneider, and Y. Xu, “A B-spline approach for empirical mode decompositions”, Advances in Computational Mathematics, vol. 24, no. 1, pp. 171-195, 2006.

S. Chen, M. Bolic, V. Z. Groza, H. R. Dajani, I. Batkin, and S. Rajan, “Extraction of breathing signal and suppression of its effects in oscillometric blood pressure measurement”, IEEE Transactions on Instrumentation and Measurement, vol. 60, no. 5, pp. 1741-1750, 2011.

F. Chia, A. T. Ang, T. W. Wong, K. P. Fung and J. Lee, “Reliability of the Dinamap non-invasive monitor in the measurement of blood pressure of ill Asian newborns”, Clinical Pediatrics, vol. 29, no. 5, pp. 262-267, 1990.

H. S. Choi, H. D. Park, and K. J. Lee, “Motion artifact reduction in blood pressure signals using adaptive digital filter with a capacitive sensor”, Proceedings of the 29th Annual International Conference of the IEEE Engineering in Medicine and Biology Society, pp. 3285-3287, 2007.

J. S. Choy, Z-D. Zhang, K. Pitsillides, M. Sosa and G. S. Kassab, “Longitudinal hemodynamic measurements in swine heart failure using a fully implantable telemetry system”, Plos One, vol. 9, no. 8, pp.1-12, 2014.

L. Chu, S. Oh, and W. Recker, “Adaptive Kalman filter based freeway travel time estimation”. In 84th Transportation Research Board Annual Meeting, Washington DC, paper no. 1118, 2005.

H. Chunbao and L. Lingjiao, “Technique research and system design of ambulatory blood pressure monitoring”, International Conference on Electronic Measurement Instruments, pp. 669-672, 2007.

`

G. Cicolini, C. Pizzi, E. Palma, M. Bucci, F. Schioppa, A. Mezzetti and L. Manzoli, “Differences in blood pressure by body position (supine, fowler’s, and sitting) in hypertensive subjects”, American Journal of Hypertension, vol. 24, no. 10, pp. 1073-1079, 2011.

J. A. Cutler, P. D. Sorlie, M. Wolz, T. Thorn, L. E. Fields and E. J. Roccella, “Trends in hypertension prevalence, awareness, treatment, and control rates in United States adults between 1988-1994 and 1999-2004”, Hypertension, vol. 52, no. 5, pp. 818-827, 2008.

S. D. Colan, A. Fujii, K. M. Borow, D. Macpherson and S. P. Sanders, “Non-invasive determination of systolic, diastolic and end-systolic blood pressure in neonates, infants and young children: comparison with central aortic pressure measurements”, American Journal of Cardiology, vol. 52, no. 7, pp. 867-870 1993.

M. Coleman, “Ageing mechanisms and stability in thick film resistors”, Microelectronics International, vol. 1, no. 4, pp. 36-41, 1984.

A. Coleman, S. Steel, P. Freeman, A. de Greeff, and A. Shennan, “Validation of the Omron M7 (HEM-780-E) oscillometric blood pressure monitoring device according to the British Hypertension Society protocol”, Blood Pressure Monitoring, vol. 13, no. 1, pp. 49–54, 2008.

P. M. Cullen, J. Dye and D. G. Hughes, “Clinical assessment of neonatal Dinamap 847 during anesthesia in neonates and infants”, Journal of Clinical Monitoring and Computing, vol. 3, no. 4, pp. 229-234, 1987.

W. H. Dawes, “The design of a family of high-current switches with over-current and over-temperature protection”, IEEE Transactions on Instrumentation and Measurement, vol. 47, no. 6, pp. 1492-1502, 1998.

A. de Greeff, I.Lorde, A. Wilton, P. Seed, A J. Coleman and AH. Shennan, “Calibration accuracy of hospital-based non-invasive blood pressure measuring devices”, Journal of Human Hypertension, vol. 24, no. 1, pp. 58–63, 2010.

`

G. K. Diaprose, D. H. Evans, L. N. Archer and M. I. and L. Dinamap “fails to detect hypertension in very low birth weight infants”, Archives of Disease in Childhood, vol. 61, no. 8, pp. 771-773, 1986.

R. H. Dieck, "Measurement uncertainty models", The International Society of Automation transactions, vol. 36, num. 1, pp. 29-35, 1997.

R. Dieme, “Characterization of noise in mems piezoresistive microphones”, Master thesis, University of Florida, pp.76-90, 2005.

E. W. Dijkstra, “A note on two problems in connection with graphs”, Numerische Mathematic, vol. 1, no. 1, pp. 269–271, 1959.

D. Donoho, “De-noising by soft-thresholding”, IEEE Transactions on Information Theory, vol. 41, no. 3, pp. 613-627, 1995.

T. J. Dorsett and C. L. Davis, “Method of artifact rejection for non-invasive blood-pressure measurement by prediction and adjustment of blood- pressure data”, US Patent No.4949710, 1990.

N. Eigler, J. Whiting and B. Mann, “Apparatus for minimally invasive calibration of implanted pressure transducers”, US Patent Application No. 7862513 B2, 2011.

Empress, “Non-invasive blood pressure and heart rate”, ESLIM_002_001, 2008. Available on: http://www.biopac.ca [April 11 2016].

P. Eswaran and S. Malarvizhi, “MEMS capacitive pressure sensors: A review on recent development and prospective”, International Journal of Engineering and Technology, vol. 5, no. 3, pp. 2734-2746, 2013.

`

R. N. Feghali, J. A. Topouchaian, B. M. Pannier, H. A. El Assaad, and R. G. Asmar, "Validation of the Omron M7 (HEM-780-E) blood pressure measuring device in a population requiring large cuff use according to the international protocol of the European society of hypertension", Blood Pressure Monitoring, vol. 12, no. 3, pp. 173–178, 2007.

J. Fiala, P. Bingger, D. Ruh, K. Foerster, C. Heilmann, F. Beyersdorf, H. Zappe and A. Seifert, "An implantable optical blood pressure sensor based on pulse transit time", Biomedical Microdevices, vol. 15, no. 1, pp. 73–81, 2013.

R. S. Figliola, and D. Beasley, "Temperature measurements" in Theory and Design for Mechanical Measurements, USA: John Wiley and Sons, 2015, pp. 333-340.

P. Flandrin, P. Goncalves, and G. Rilling, "Detrending and denoising with empirical mode decompositions", In IEEE 12th European Signal Processing Conference, pp. 1581-1584, 2004.

A. CM. Fong, B. Fong and G.Y. Hong, "Environmental impact on the reliability of mass produced consumer glucose meters", IEEE Conference on Industrial Electronics and Applications, pp. 6-10, 2011.

M. Forouzanfar, H. R. Dajani, V. Z. Groza, M. Bolic, and S. Rajan, "Comparison of feed-forward neural network training algorithms for oscillometric blood pressure estimation", IEEE 4th International Workshop on Soft Computing Applications, pp. 119–123, 2010.

M. Forouzanfar, B. Balasingam, H. R. Dajani, V. Groza, M. Bolic, S. Rajan, and E. M. Petriu, "Mathematical modeling and parameter estimation of blood pressure oscillometric waveform", in IEEE International Symposiumon Medical Measurement and Applications, pp. 208–213, 2012.

M. Forouzanfar, "A modeling approach for coefficient-free oscillometric blood pressure estimation", Doctoral dissertation, University of Ottawa, Canada, pp. 13-90, 2014.

M. Forouzanfar, H. Dajani, V. Groza, M. Bolic, and S. Rajan, "Oscillometric blood pressure estimation: past, present, and future", IEEE Reviews in Biomedical Engineering, vol. 8, pp. 44-62, 2015.

F. K. Forster and D. Turney, “Oscillometric determination of diastolic, mean, and systolic blood pressure – A numerical model”, Journal of Biomechanical Engineering, vol. 108, no. 4, pp. 359–364, 1986.

R. H. Friesen and J. L. Lichtor, “Indirect measurement of blood pressure in neonates and infants utilizing an automatic non-invasive oscillometric monitor”, Anesthesia and Analgesia, vol. 60, no. 10, pp. 742-745, 1981.

T. Fujiwara, M. Kawamura, J. Nakajima, T. Adachi, and K. Hiramori, “Seasonal differences in diurnal blood pressure of hypertensive patients living in a stable environmental temperature”, Journal of Hypertension, vol. 13, no. 12.2, pp. 1747-1752, 1995.

J. Gama and G. Castillo, “Learning with local drift detection”, Springer Berlin Heidelberg in Advanced Data Mining and Applications, vol. 4093, pp. 42-55, 2006.

J. Gao, H Sultan, J. Hu, and W. W. Tung. (2010). “Denoising nonlinear time series by adaptive filtering and wavelet shrinkage: a comparison”, IEEE Signal Processing Letters, vol. 17, no. 3, pp. 237-240, 2010.

L. A. Geddes, M. Voelz, C. Combs, D. Reiner and C.F. Babbs, “Characterization of the oscillometric method for measuring indirect blood pressure”, Annals of Biomedical Engineering, vol. 10, no. 6, pp. 271-280, 1982.

G. Gersak, V. Batagelj and J. Drnovsek, “Oscillometric virtual instrument for blood pressure measurement”, XVIII Imeko World Congress, pp. 17-22, 2006.

H. Gesche, D. Grosskurth, G. Kuchler, and A. Patzak, “Continuous blood pressure measurement by using the pulse transit time: Comparison to a cuff-based method”, European Journal of Applied Physiology, vol. 112, no. 1, pp. 309–315, 2012.

M. Gevers, H. R. van Genderingen, H. N. Labfeber, W. Hack, “Accuracy of oscillometric blood pressure measurements in critically ill neonates with reference to the arterial pressure wave shape”, Journal of Intensive Care Medicine, vol. 22, no. 3, pp. 242-248 1996.

`

P. Gibbs and H. Asada, “Reducing motion artifact in wearable bio-sensors using MEMS accelerometers for active noise cancellation”, American Control Conference, pp. 1581-1586, 2005.

G. S. Gibson, “Vital signs monitor”, US Patent No. US0281168, 2008.

J. Gunaselvam and J. L. van Niekerk, “Seat selection guidelines to reduce whole-body vibration exposure levels in the SA mining industry”, The Journal of the South African Institute of Mining and Metallurgy, vol. 105, pp. 657- 672, 2005.

J. Halonen, A. Zanobetti, D. Sparrow, P. S. Vokonasa and J. Schwartz, “Environment relationship between outdoor temperature and blood pressure”, Occupational and Environmental Medicine, vol. 68, no. 4, pp. 296-301, 2011.

T. Hasan and M. K. Hasan, “Suppression of residual noise from speech signals using empirical mode decomposition”, IEEE Signal Processing Letters, vol. 16, no. 1, pp. 2-5, 2009.

X. He, R. A. Goubran, and X. P. Liu, “Signal enhancement of wearable ECG monitoring sensors based on ensemble empirical mode decomposition”, IEEE International Symposium on Medical Measurements and Applications Proceedings, pp. 433-436, 2011.

X. He, R. A. Goubran, and X. P. Liu, “Ensemble empirical mode decomposition and adaptive filtering for ECG signal enhancement”, IEEE International Symposium on Medical Measurements and Applications Proceedings, pp. 1-5, 2012.

X. He, R. A. Goubran, and X. P. Liu, “Evaluation of the correlation between blood pressure and pulse transit time”, IEEE International Symposium on Medical Measurement and Applications, pp. 17–20, 2013.

X. He, R. A. Goubran, and X. P. Liu, “A novel sub-band adaptive filtering for acoustic echo cancellation based on empirical mode decomposition algorithm”, International Journal of Speech Technology, vol. 17, no. 1, pp. 37-42, 2014.

`

W.P. Holsinger, K.M. Kempner and M.H. Miller, “A QRS preprocessor based on digital differentiation”, IEEE Transactions on Bio-Medical, vol. 18, no. 3, pp. 212-217, 1971.

A. Hozawa, S. Kuriyama, T. Shimazu, K. Ohmori-Matsuda and I. Tsuji, “Seasonal variation in home blood pressure measurements and relation to outside temperature in Japan”, Clinical and Experimental Hypertension, vol. 33, no. 3, pp. 153-158, 2011.

N. E. Huang, Z. Shen, S. R. Long, M. C. Wu, H. Shih, Q. Zheng, and H. Liu, “The empirical mode decomposition and the Hilbert spectrum for nonlinear and non-stationary time series analysis”, Proceedings of the Royal Society of London. Series A: Mathematical, physical and Engineering Sciences, vol. 454, pp. 903-995, 1971.

C. Huo, J. Wang, J. Zhang and S. Liu, “Blood pressure measurement based on wavelet analysis and fuzzy inference method”, IEEE Proceedings of the 6th World Congress on Intelligent Control and Automation, vol. 1, pp.4382-4386, 2006.

E. S. Hwang, Y. J. Kim, and B. K. Ju, “Flexible polysilicon sensor array modules using “etch-release” packageing scheme”, Sensors and Actuators A: Physical, vol. 111, no. 1, pp. 135-141, 2004.

G. B. Iyalomhe and S. I. Iyalomhe, “related knowledge, attitudes and life-style practices among hypertensive patients in a sub-urban Nigerian community”, Journal of Public Health and Epidemiology, vol. 2, no. 4, pp. 71-77, 2010.

G. D. James, T. G. Pickering, L. S. Yee, G. A. Harshfield, S. Riva and J. H. Laragh, “The reproducibility of average ambulatory, home, and clinic pressures”, Hypertension, vol. 11, no. 6.1, pp. 545-549, 1988.

V. Jazbinsek, J. Luznik and Z. Trontelj, “Non-invasive blood pressure measurements: separation of the arterial pressure oscillometric waveform from the deflation using digital filtering” Proceedings of European Medical and Biological Engineering Conference, vol. 11, no. 1, 2005.

W. Jung, “Getting the most from IC voltage references”, in Analog Dialogue, vol. 28, no. 1, D. Sheingold, USA: Analog Devices, 1994, pp. 13-21.

`

R. Kalia, “Analysis of ambient temperature effect on blood viscosity and blood pressure drop”, Doctoral dissertation, Thapar University, India, 2014.

Y. Kanda, “A graphical representation of the piezoresistance coefficients in silicon”, IEEE Transactions on Electron Devices, vol. 29, no. 1, pp. 64-70, 1982.

D. N. Kaslovsky, and F. G. Meyer, “Noise corruption of empirical mode decomposition and its effect on instantaneous frequency”, Advances in Adaptive Data Analysis, vol. 2, no. 3, pp. 373-396, 2010.

K. Khaldi, A. O. Boudraa, A. Bouchikhi, M. T. H. Alouane, and E. H. S. Diop, “Speech signal noise reduction by EMD”, IEEE 3rd International Symposium on Communications, Control and Signal Processing, pp. 1155-1158, 2008.

S. C. Kim, and K. D. Wise, “Temperature sensitivity in silicon piezoresistive pressure transducers”, IEEE Transactionson Electron Devices, vol. 30, no. 7, pp. 802-810, 1983.

K J. Kimble, R. A. Darnall, M. Yelderman, R. Ariagno and A. K. Ream, “An automated oscillometric technique for estimating mean arterial pressure in critically ill new borns Anesthesiology”, Anesthesiology, vol. 54, no. 5, pp. 423-425, 1981.

R. Klinkenberg and I. Renz, “Adaptive information filtering: Learning in the presence of concept drifts”, AAAI Press, pp.33–40, 1998.

B. U. Kohler, C. Hennig and R. Orglmeister, “QRS detection using zero crossing counts”, Progress in Biomedical Research, vol. 8, pp. 138-145. 2003.

Y. Koo, J.Kang, I. H. Shin, M. Yang, G. J. Suh, and H. C. Kim, “Preliminary study of motion artifact rejection for NIBP measurement in an Ambulance”, Proceedings of the 29th Annual International Conference of the IEEE European Medical and Biological Engineering, pp.705-708, 2007.

`

H. J. Kress, F. Bantien, J. Marek and M. Willmann, “Silicon pressure sensor with integrated CMOS signal conditioning circuit and compensation of temperature coefficient”, Sensors and Actuators A, vol. 25, no. 1-3, pp.21-26, 1990.

D. Labate, F. L. Foresta, G. Occhiuto, F. C. Morabito, A. Lay-Ekuakille, and P. Vergallo, “Empirical mode decomposition vs. wavelet decomposition for the extraction of respiratory signal from single-channel ECG: A comparison”, IEEE SensorsJournal, vol. 30, no. 7, pp. 2666-2674, 2013.

F. Lamonaca, K. Barbe, Y. Kurylyak, D. Grimaldi, W. Van Moer, A. Furfaro, and V. Spagnuolo, “Application of the artificial neural network for blood pressure evaluation with smartphones”, IEEE International. Conference on Intelligent Data Acquisition and Advanced Computing Systems: Technology and Applications, pp. 408–412, 2013.

B. P. Lathi, and Z. Ding "Signals and Signal Space", in Modern Digital and Analog Communication Systems, A. S. Sedra, USA: Oxford University Press, 2009, pp. 20.

I. H. Leng, D. Lang, T. and Seng, “Clinical comparison of non-invasive blood pressure measurement at different sites: a systematic review protocol”, The JBI Database of Systematic Reviews and Implementation Reports, vol. 12, no. 4, pp.86-101, 2014.

J. K. Lenkkeri, “Nonlinear effects in the piezoresistivity of p-type silicon”, Physica Status Solidi (b)”, vol. 136, no. 1, pp. 373-385, 1986.

S. Li, Z Zhang, J. Tang, and D. Ding, “A novel signal conditioning circuit for piezoresistive pressure sensor”, In Unifying Electrical Engineering and Electronics Engineering, vol. 238, pp. 1707-1713, 2014.

CT. Lin, SH. Liu, JJ. Wang and ZC. Wen, “Reduction of interference in oscillometric arterial blood pressure measurement using fuzzy logic”, IEEE Transactions on Biomedical Engineering, vol. 50, no. 4, pp. 432-41, 2003.

D. Looney, L. Li, T. M. Rutkowski, D. P. Mandic, and A. Cichocki, “Ocular artifacts removal from EEG using EMD”, In Advances in Cognitive Neurodynamics ICCN 2007, pp. 831-835, 2008.

`

E. J. Marey, “Ecole Practique des Hautes Etudes”, Physiologie Experimentale, vol. 6, pp. 307-343, 1876.

Manual, Electronic, or Automated Sphygmomanometers, ANSI/AAMI SP10 Standard, Arlington, TX, 2002.

E. Martel, B. Egner, S. A. Brown, J. N. King, A. Laveissiere, P. Champeroux and S. Richard, “Comparison of high-definition oscillometry — a non-invasive technology for arterial blood pressure measurement — with a direct invasive method using radio-telemetry in awake healthy cats”, Journal Citation Reports, vol. 15, no. 12, pp.43-129, 2013.

G. S. Mattu, T. L. Perry, L. J. Thomas and J. M. Wright, “Comparison of the oscillometric blood pressure monitor (BPM-100 Beta) with the auscultatory mercury sphygmomanometer”, Blood Pressure Monitoring, vol. 6, no. 3, pp 153-159, 2001.

Mechanical vibration and shock—Evaluation of human exposure to whole-body vibration—Part 1: General requirements. International Standard, ISO 2631-1. 1997.

Medicines and Healthcare Products Regulatory Agency, “blood pressure measurement devices”, v2.1, pp.1-16, 2012.

A. Miersch, M. Vogel, R. Gausche, W. Siekmeyer, R. Pfäffle, K. Dittrich and W. Kiess, “Influence of seasonal variation on blood pressure measurements in children, adolescents and young adults”, Pediatric Nephrology, vol. 28, no. 12, pp. 2343-2349, 2013.

E. Mizutani, “The dynamic time warping algorithms”, Tokyo Metropolitan University Press, pp. 1-11, 2006.

D. Mladenovic, J. Hutchins, E. Tran, and S. Lu. “Element for modeling diffused piezoresistor temperature coefficient and sensitivity”,Technical Proceedings of the 1998 International Conference on Modeling and Simulation of Microsystems, pp. 145-150, 1988.

V. Montiel, E. Leon Gomez, C. Bouzin, H. Esfahani, M. Romero Perez, I. Lobysheva, O. Devuyst, C. Dessy and J. L. Balligand, “Genetic deletion of aquaporin-1 results in microcardia and low

`

blood pressure in mouse with intact nitricoxide-dependent relaxation, but enhanced prostanoids-dependent relaxation", Pflügers Archive European Journal of Physiology, vol. 466, no. 2, pp. 237–251, 2014.

S. Muecke, B. Hons, A. Bersten, and J. Plummer, "The mean machine; accurate non-invasive blood pressure measurement in the critically ill patient", Journal of Clinical Monitoring and Computing, vol. 23, no. 5, pp. 283–297, 2009.

M. G. Myers and M. Valdivieso, "Evaluation of an automated sphygmomanometer for use in the office setting", Blood Pressure Monitoring, vol. 17, no. 3, pp.116-119, 2012.

R. M. Nelson, A. D. Stebor, C. M. Groh, P. M. Timoney, K. S. Theobald and B. A. Friedman, "Determination of accuracy in neonates for non-invasive blood pressure devices using an improved algorithm", Blood Pressure Monitoring, vol. 7, no. 2, pp. 123-129, 2002.

J. Neumann, D. W. Greve and J. Irving, "Comparison of piezoresistive and capacitive ultrasonictransducers", The International Society for Optics and PhotonicsProceedings on Novel Sensors II, vol. 5391, pp. 230-238, 2004.

S. R. Newell, "Validity study of oscillometric blood pressure measurement devices using an oscillometric waveform simulator", Master thesis, Aalborg University, Denmark, pp. 30, 2013.

NHS Informing Procurement, "Hospital grade non-invasive blood pressure monitors", white paper CEP 08018, 2008. Available from: https://www.welchallyn.com [April 11 2016].

I. R. Nicolaas, "Ambulatory blood pressure monitoring", Doctoral dissertation, Erasmus University Rotterdam, Netherlands, pp.20-29, 1996.

Noharm.org, "Guidance on maintaining and calibrating non mercury clinical thermometers and sphygmomanometers", Available form:
https://noharm.org/sites/default/files/lib/downloads/mercury/Guidance_Hg_2013.pdf, 2013 [Feb. 13 2016].

`

Non-invasive sphygmomanometers – Part 2: Clinical validation of automated measurement type, ANSI/AAMI/ISO 81060-2 Standard, Arlington, TX, 2013.

P. Octavian, P. Girao, and G. Postolache, “Multi-channel architecture for evaluation of automated oscillometric blood pressure devices”, IEEE International Symposium on Medical Measurements and Applications Proceedings, pp. 207-212, 2013.

Omron: Patient Monitor Operator’s Manual - Model: HBP-2070, Omron Healthcare Inc., Bannockburn, IL 60015, 2012, pp.12-20.

Y. Ostchega, R. J. Prineas, T. Nwankwo and G. Zipf, “Assessing blood pressure accuracy of an Aneroid Sphygmomanometer in a national survey environment”, American Journal of Hypertension, vol. 24, no. 3, pp. 322-327, 2011.

G. Papadopoulos, S. Mieke and M. Elisat, “Assessment of the performance of three oscillometric blood pressure monitors for neonates using a simulator”, Blood Pressure Monitoring, vol. 4, no. 1, pp.27-33, 1999.

T. G. Papaioannou, A. Protogerou and C. Stefanadis, “Comparison between Mobil-O-Graph and the SphygmoCor device for central systolic blood pressure estimation: consensus is required for ‘validation protocols’”, Blood Pressure Monitoring, vol. 17, no. 6, pp. 259–260, 2012.

G. Parati, G. S. Stergiou, R. Asmar, G. Bilo, P. de Leeuw, Y. Imai, K. Kario, E. Lurbe, A. Manolis, T.Mengden, E. O'Brien, T. Ohkubo, P. Padfield, P. Palatini, T. G. Pickering, J. Redon, M. Revera, L. M. Ruilope, A. Shennan, J. A. Staessen, A. Tisler, B. Waeber, A. Zanchetti and G. Mancia, “European society of hypertension practice guidelines for home blood pressure monitoring”, Journal of Human Hypertension, vol. 24, no. 12, pp. 779–785, 2010.

M. K. Park and S. M. Menard, “Accuracy of blood pressure measurement by the dinamap monitor in infants and children”, Pediatrics, vol. 79, no. 6, pp. 907-914, 1987.

H. D. Park, H. S. Choi, S. P. Cho and J. Lee, “Minimization of artifact using adaptive digital filter during the Oscillometric blood pressure measurement”, IEEE International Conference on Control, Automation and Systems, pp. 2429-2432, 2007.

`

O. Picker, A. Schindler, T.W.L. Scheeren, "Accuracy and reproducibility of long-term implanted transit-time ultrasound flow probes in dogs", Springer Intensive Care Medicine, vol. 26, no. 5, pp.601-607, 2000.

T. G. Pickering, J. E. Hall, L. J. Appel, B. E. Falkner, J. Graves, M. N. Hill, D. W. Jones, T. Kurtz, S. G. Sheps and E. J. Roccella, "Recommendations for blood pressure measurement in humans and experimental animals: Part 1: Blood pressure measurement in humans: A statement for professionals from the subcommittee of professional and public education of the American heart association council on high blood pressure research", Hypertension. Vol. 111, no. 5, pp. 142-161, 2005.

É. Pinet, A. Pham and S. Rioux, "Miniature fiber optic pressure sensor for medical applications: an opportunity for intra-aortic balloon pumping (IABP) therapy", 17th International Conference on Optical Fibre Sensors, vol. 5855, pp. 234-237, 2005.

E. Pinheiro, O. Postolache, and P. Girao, "Empirical mode decomposition and principal component analysis implementation in processing non-invasive cardiovascular signals", Measurement, vol. 45, no. 2, pp. 175-181, 2012.

Prospective Studies Collaboration, "Age-specific relevance of usual blood pressure to vascular morality: a meta-analysis of individual data for one million adults in 61 prospective studies", The Luncet, vol. 360, pp. 1903-1913, 2002.

D. M. Rabi, and 63 other authors, "The 2011 Canadian hypertension education program recommendations for the management of hypertension: Blood pressure measurement, diagnosis, assessment of risk, and therapy", Canadian Journal of Cardiology, vol. 27, no. 4, pp. 415-433, 2011.

K. A. Reddy, B. George, and V. J. Kumar, "Use of fourier series analysis for motion artifact reduction and data compression of photoplethysmographic signals", IEEE Transactions on Instrumentation and Measurement, vol. 58, no.5, pp. 1706-1711, 2009.

Revision labs, "Non-invasive blood pressure measurement and motion artifact: A comparative study", white papers, 1998. Available from: http://intl.welchallyn.com [Oct 1st 2015].

`

W. Riedel, S. Mieke, R. Seemann and B. Ittermann, “A simulator for oscillometric blood-pressure signals to test automated non-invasive sphygmomanometers”, Review of Scientific Instruments. 024303, vol. 82, no. 2, 2011.

G Rilling, P Flandrin, and P Goncalves, “On empirical mode decomposition and its algorithms”, In IEEE-European Association for Signal ProcessingWorkshop on Nonlinear Signal and Image Processing, vol. 3, pp. 8-11, 2003.

A. Sachenko, V. Kochan and V. Turchenko, “Sensor drift prediction using neural networks”, International Workshop on Virtual and Intelligent Measurement Systems, pp.88-92, 2000.

I. Saito, T. Chinzei, T. Isoyama, H. Miura, A. Kouno, T. Ono, H. Nakagawa1, S. Yamaguchi-Sekine, W. Shi, Y. Inoue, A. Kishi and Y. Abe, “Implementation of the natural heartbeat synchronize control for the undulation pump ventricular assist device using the inflow pressure”, 7th Asian-Pacific Conference on Medical and Biological Engineering IFMBE Proceedings, vol. 19, pp. 62-65, 2008.

S. Salvador, and P. Chan, “Toward accurate dynamic time warping in linear time and space”, Intelligent Data Analysis, vol. 11, no. 5, pp. 561-580, 2007.

N. Samson, S. Dumont, M-L. Specq, and J-P. Praud, “Radio telemetry devices to monitor breathing in non-sedated animals”, Respiratory Physiology and Neurobiology, vol. 179, no. 2-3, pp.111-118, 2011.

Samsung, “Owner’s manual: Wrist blood pressure - Monitor with heart sense”, 2006, pp.1-5.

Z. M. Santo, D. Belavic, and S. Macek, “The warm-up and offset stability of a low-pressure piezoresistive ceramic pressure sensor”, Sensors and Actuators A: Physical, vol. 158, no. 2, pp. 198-206, 2010.

Z. M. Santo, V. Sedlakova, D. Belavic, J. Sikula, J. Majzner and Petr Sedlak, “Estimation of the long-term stability of piezoresistive LTCC pressure sensors by means of low-frequency noise measurements”, Sensors and Actuators A: Physical, vol. 199, no. 1, pp. 334-343, 2013.

`

S. Sarath and R. Komaragiri, “Feasibility study of AC bridges in MEMS pressure sensors”, IEEE Students' Conference on Electrical, Electronics and Computer Science, pp. 1-4, 2012.

F. Schneider, T. Fellner, J. Wilde, and U. Wallrabe, “Mechanical properties of silicones for MEMS”, Journal of Micromechanics and Microengineering, vol. 18, no. 6, pp. 18-24, 2008.

E. P. Scilingo, F. Lorussi, A. Mazzoldi, and D. De Rossi “Strain-sensing fabrics for wearable kinaesthetic-like systems”, IEEE on Sensors Journal, vol. 3, no. 4, pp. 460-467, 2003.

K. Seifedine, “Structure reliability and response prognostics under uncertainty using Bayesian analysis and analytical approximations”, in Diagnostics and Prognostics of Engineering Systems: Methods and Techniques, K. Seifedine, USA: IGI Global, 2012, pp. 379.

J-S. Seo, H-Y. Jin, J-S. Jang, T-H. Yang, D-K. Kim and D-S. Kim, “868 Ambulatory blood pressure variability and carotid intima-media thickness in treated hypertensive patient”, Journal of Hypertension, vol. 30, pp. e254, 2012.

J. Settels, “Time and volumetric capnography”, in Monitoring Technologies in Acute Care Environments”, J. M. Ehrenfeld,USA: Springer, 2014, pp.187-107.

N. Sinnadurai, and K. J. Wilson, “The ageingbehaviour of commercial thick-film resistors”,IEEE Transactions onComponents, Hybrids, and Manufacturing Technology, vol. 5, no. 3, pp. 308-317, 1982.

A. S. Shah, L. M. Dolan, R. B. D'Agostino, D. Standiford, C. Davis, L. Testaverde, C. Pihoker and S. R. Daniels, “Comparison of mercury and aneroid blood pressure measurements in youth”, Pediatrics, vol. 129, no. 5, pp. e1205 -e1210, 2012.

T. Sharma, S-S.Je, B Gill and J Zhang, “Patterning piezoelectric thin film PVDF–TrFE based pressure sensor for catheter application”, Sensors and Actuators, vol. 177, pp. 87–92, 2012.

`

W. Shi, I. Saito, T. Isoyama, H. Nakagawa, Y. Inoue, T. Ono, A. Kouno, K. Imachi and Y. Abe, “Automatic calibration of the inlet pressure sensor for the implantable continuous flow ventricular assist device”, Journal of Artificial Organs, vol. 14, no. 2, pp. 81–88, 2011.

H. S. Shin, C. Lee and M. Lee, “Adaptive threshold method for the peak detection of photoplethysmographic waveform”, Computers in Biology and Medicine, vol. 39, no. 12, pp. 1145-1152, 2009.

H. Skirton, W. Chamberlain, C. Lawson, H. Ryan and E. Young, “A systematic review of variability and reliability of manual and automated blood pressure readings”, Journal of Clinical Nursing, vol. 20, no. 5-6, pp. 602–614, 2011.

S. W. Smith, “Filter comparison”, in The Scientist and Engineer's Guide to Digital Signal Processing”, S. W. Smith, USA: California Technical Publishing, 1997, pp.169-174.

S. E. Sonesson and U. Broberger, “Arterial blood pressure in the very low birth weight neonate”, Acta Paediatrica Scandinavica, vol. 76, no. 2, pp. 338-341, 1987.

R. Sorvoja, R. Myllyla, P. Karja-Koskenkari, J. Koskenkari, M. Lilja and A. Kesaniemi, “Accuracy comparison of oscillometric and electronic palpation blood pressure measuring methods using intra-arterial method as a reference”, Molecular and Quantum Acoustics, vol. 26, pp. 235-260, 2005.

Specification for non-invasive sphygmomanometers. Part 1: General requirements, European Standard EN 1060-1:1996, Brussels, 1996.

A. D. Stebor, “Basic principles of non-invasive blood pressure measurement in infants”, Advances in Neonatal Care, vol. 5, no. 5, pp.252, 2005.

G. Stergiou, G. Parati, R. Asmar and E. O’Brien, “Blood pressure measurement requirements for professional office blood pressure monitors”, Journal of Hypertension, vol. 13, no. 5, pp. 537–542, 2012.

`

N. Stevenson, M. Mesbah, and B. Boashash, "A sampling limit for the empirical mode decomposition", the 8th International IEEE Symposium on Signal Processing and its Applications, vol. 459, no. 2037, pp. 647-650, 2005.

K. J. Suja, T. V. Vidya Gopal, K. R. Komaragiri, "Optimized design of double diaphragm based mems pressure sensor for wider range and better sensitivity", International Journal of Emerging Science and Engineering, vol. 72, no. 8, pp. 2319–6378, 2013.

H. R. Tamim, and H. V. Estrada. "Temperature dependence of In-doped silicon strain gages", IEEE Proceedings of Southeastcon, vol. 2, pp. 1101-1105, 1991.

S. Tankiewicz, B. Morten, M. Prudenziati, and L. J. Golonka, "New thick-film material for piezoresistive sensors", Sensors and Actuators A: Physical, vol. 95, no. 1, pp. 39-45, 2001.

L. A. Taylor, R. G. Bennett and T. J. Dorsett, "The application of signal averaging to the NIBP oscillometric waveform", IEEE Proceedings of Annual International Conference Engineering in Medicine and Biology Society, vol. 1, pp.691-2, 1995.

X. F. Teng and Y. T. Zhang, "Theoretical study on the effect of sensor contact force on pulse transit time", IEEE Transactions on Biomedical Engineering, vol. 54, no. 8, pp. 1490–1498, 2007.

S. Terry, J. Eckerle, R. Kornbluh, T. Low and C. Ablow, "Silicon pressure transducer arrays for blood-pressure measurement", Sensors and Actuators, vol. 23, no. 1-3, pp. 1070–1079, 1990.

P. P. Thakkar, "The removal of motion artifacts from non-invasive blood pressure measurements", Doctoral dissertation, University of Central Florida Orlando, USA, 2005.

M. Theodora, J. Fialaa, D. Ruha, K. Försterb, C. Heilmannb, F. Beyersdorfb, Y. Manolia,H. Zappea and A. Seiferta, "Implantable accelerometer system for the determination of blood pressure using reflected wave transit time", Sensors and Actuators A: Physical, vol. 206, no. 1, pp. 151–158, 2014.

K. Tian, Z. Wang, M. Zhang, and L. Liu. “Design, fabrication, and calibration of a piezoresistive stress sensor on SOI wafers for electronic packaging applications”, IEEE Transactions onComponents and Packaging Technologies, vol. 32, no. 2, pp. 513-520, 2009.

K. Totsu, Y. Haga and M. Esashi, “Ultra-miniature fiber-optic pressure sensor using white light interferometry”, Journal of Micromechanics and Microengineering, vol. 15, no. 1, pp. 71-75, 2005.

T. Usuda, N. Kobayashi, S. Takeda, and Y. Kotake, “A blood pressure monitor with robust noise reduction system under linear cuff inflation and deflation”, International Conference of the IEEE Engineering in Medicine and Biology Society, vol. 1226, no. 9, pp. 1226-1229, 2010.

K. van den Hurk, W. L. de Kort, J. Deinum, and F. Atsma, “Higher outdoor temperatures are progressively associated with lower blood pressure–a longitudinal study in 100,000 healthy individuals”, Journal of the American Society of Hypertension, vol. 9, no. 7, pp. 536-579, 2015.

R. A. Walloch, “Apparatus for identifying artefact in automatic blood pressure measurements”, US Patent Application, no. 254371, 1990.

Q. Wang, J. Zhang, R. Hu and G. Sun, “Transistor compensation technology of pressure sensorsensitivity temperature coefficient”, Applied Mechanics and Materials, vol. 43, pp. 371-375, 2011.

J. A. Wareham, L. D. Haugh, S. B. Yeager and J. D. Horbar, “Prediction of atrial blood pressure in the premature neonte using oscillometric method”, The American Journal of Diseases of Children, vol. 141, no. 10, pp. 1108-1110, 1987.

M. Weisz and J. Francis, “Basic measurement concepts”, Anaesthesia and Intensive Care Medicine, vol. 15, no. 7, pp. 412-414, 2011.

E. A. Whitsel, J. Tabor, J. Groner, and C. Schuft, “Blood pressure monitor calibration form and protocol”, Add Health, Carolina Population Center, pp. 1-8, 2015.

Z. Wu and N. E. Huang, “Ensemble empirical mode decomposition: a noise-assisted data analysis method”, Advances in Adaptive Data Analysis, vol. 1, no. 1, pp. 1-41, 2009.

`

D. Xu and Y. Liu, “A temperature compensation algorithm of piezoresistive pressure sensor and software implementation”, IEEE Conference on Mechatronics and Automation, pp. 1738 - 1742, 2013.

B. Yang, K. H. Chon, “A novel approach to monitor nonstationary dynamics in physiological signals: application to blood pressure, pulse oximeter, and respiratory data”, Annals of Biomedical Engineering, vol. 38, no. 11, pp. 38-49, 2010.

P. G. Yong and L. A. Geddes, “The effect of cuff pressure deflation rate on accuracy in indirect measurement of blood pressure with the Auscultatory method”, Journal of Clinical Monitoring, vol. 3, no. 3, pp. 155-159, 1987.

A. Zaknich, “Optimum wiener filter”, in Principles of Adaptive Filters and Self-learning Systems, M. J. Grimble, Germany: Springer Science and Business Media, 2005, pp.173-194.

M. S. Zernike and D. Belavic, “The effect of humidity on the stability of LTCC pressure sensors”, Metrology and Measurement Systems, vol. 19, no. 1, pp. 133-140, 2012.

M. S. Zernike, V. Sedlakovad, D. Belavic, J. Sikula, J. Majzner and P. Sedlak, “Estimation of the long-term stability of piezoresistive LTCC pressure sensors by means of low-frequency noise measurements”, Physical sensors and actuators, vol. 199, pp.334-343, 2013.

R. J. Zwijnenberg, C. L. Del Rio, R. M. Cobb and Y. Ueyama, “Evaluation of oscillometric and vascular access port arterial blood pressure measurement techniques versus implanted telemetry in anesthetized cats”, American Journal of Veterinary Research, vol. 72, no. 8, pp. 1015-1021, 2011.

`

APPENDIX A

Transient motion artifacts performed by the participants including the type of motion and the number of times (triggers) the motion artifacts was performed at random times during each blood pressure measurement.

Motion artifact source	**# of triggers**	**Absolute error [mmHg]**			
		SBP		**DBP**	
		IMFSA	*Conv**	*IMFSA*	*Conv**
Elbow up	2	6.0	10.5	3.0	5.4
Elbow up	2	5.0	21.0	3.6	1.2
Elbow up	2	0.0	27.1	0.5	5.0
Elbow up	2	2.0	15.2	1.6	1.0
Elbow up	2	2.5	12.0	3.0	3.0
Elbow up	2	2.5	20.0	2.0	39.5
Elbow up	3	2.1	11.5	2.0	4.3
Elbow up	2	0.6	10.4	1.3	3.0
Elbow up	2	2.0	15.2	1.6	1.0
Elbow up	2	2.1	12.5	2.4	2.9
Hand up	1	6.0	8.0	0.5	10.9
Hand up	1	3.0	9.0	3.6	2.0
Hand up	1	1.5	9.1	4.6	5.14
Hand up	1	1.0	12	3.0	8.1
Hand up	1	0.0	7.0	0.0	2.0
Fingers tapping	3	8.0	6.4	4.0	5.0
Fingers tapping	3	2.0	3.2	3.0	10
Fingers tapping	3	1.8	0.9	7.0	4.9
Fingers tapping	3	3.7	5	4.0	3.5
Fingers tapping	3	2.0	4.8	0.0	0.5
Fingers tapping	3	1.2	1.5	1.0	1.8

`

Fingers tapping	3	1.3	0.6	1.0	2.5
Fingers tapping	3	0.8	1.1	4.0	7.0
Fingers tapping	3	2.0	5.0	3.0	0.5
Fingers tapping	3	1.0	5.5	1.0	1.0
Total	56				

*Conv: Conventional blood pressure estimation algorithm that does not include artifact suppression.

Freescale Semiconductor
Technical Data

Document Number: MMA7361L
Rev 0, 04/2008

RoHS

±1.5g, ±6g Three Axis Low-g Micromachined Accelerometer

MMA7361L

The MMA7361L is a low power, low profile capacitive micromachined accelerometer featuring signal conditioning, a 1-pole low pass filter, temperature compensation, self test, 0g-Detect which detects linear freefall, and g-Select which allows for the selection between 2 sensitivities. Zero-g offset and sensitivity are factory set and require no external devices. The MMA7361L includes a Sleep Mode that makes it ideal for handheld battery powered electronics.

MMA7361L: XYZ AXIS ACCELEROMETER
±1.5g, ±6g

Features

- 3mm x 5mm x 1.0mm LGA-14 Package
- Low Current Consumption: 400 μA
- Sleep Mode: 3 μA
- Low Voltage Operation: 2.2 V – 3.6 V
- High Sensitivity (800 mV/g @ 1.5g)
- Selectable Sensitivity (±1.5g, ±6g)
- Fast Turn On Time (0.5 ms Enable Response Time)
- Self Test for Freefall Detect Diagnosis
- 0g-Detect for Freefall Protection
- Signal Conditioning with Low Pass Filter
- Robust Design, High Shocks Survivability
- RoHS Compliant
- Environmentally Preferred Product
- Low Cost

Bottom View

14 LEAD
LGA
CASE 1977-01

Typical Applications

- 3D Gaming: Tilt and Motion Sensing, Event Recorder
- HDD MP3 Player: Freefall Detection
- Laptop PC: Freefall Detection, Anti-Theft
- Cell Phone: Image Stability, Text Scroll, Motion Dialing, E-Compass
- Pedometer: Motion Sensing
- PDA: Text Scroll
- Navigation and Dead Reckoning: E-Compass Tilt Compensation
- Robotics: Motion Sensing

Top View

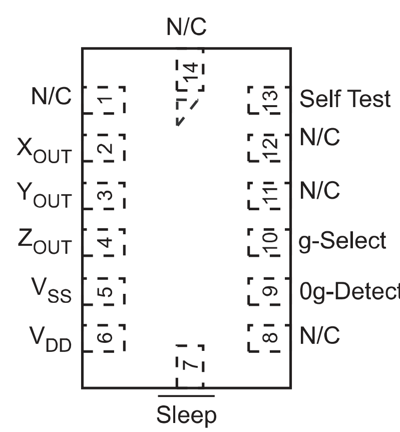

Figure 1. Pin Connections

ORDERING INFORMATION				
Part Number	**Temperature Range**	**Package Drawing**	**Package**	**Shipping**
MMA7361LT	–40 to +85°C	1977-01	LGA-14	Tray
MMA7361LR1	–40 to +85°C	1977-01	LGA-14	7" Tape & Reel
MMA7361LR2	–40 to +85°C	1977-01	LGA-14	13" Tape & Reel

freescale semiconductor

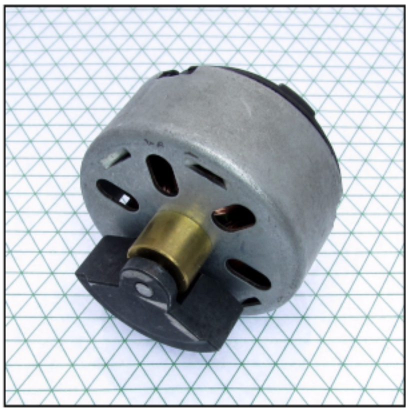

45mm Vibration Motor - 28mm Type
Shown on 6mm Isometric Grid

PRECISION MICRODRIVES™

Product Data Sheet
Uni Vibe™
45mm Vibration Motor - 28mm Type

Model: 345-400

Ordering Information

The model number 345-400 fully defines the model, variant and additional features of the product. Please quote this number when ordering.
For stocked types, testing and evaluation samples can be ordered directly through our online store.

Datasheet Versions

It is our intention to provide our customers with the best information available to ensure the successful integration between our products and your application. Therefore, our publications will be updated and enhanced as improvements to the data and product updates are introduced.
To obtain the most up-to-date version of this datasheet, please visit our website at:
www.precisionmicrodrives.com
The version number of this datasheet can be found on the bottom left hand corner of any page of the datasheet and is referenced with an ascending R-number (e.g. R002 is newer than R001). Please contact us if you require a copy of the engineering change notice between revisions.

If you have any questions, suggestions or comments regarding this publication or need technical assistance, please contact us via email at:
enquiries@precisionmicrodrives.com or call us on +44 (0) 1932 252 482

Key Features

Body Diameter:	45 mm [+/- 0.2]
Body Length:	27.6 mm [+/- 0.2]
Counterweight Radius:	17.5 mm [+/- 0.2]
Counterweight Length:	11.5 mm [+/- 0.2]
Shaft Orientation:	Inline
Rated Operating Voltage:	12 V
Rated Vibration Speed:	4,400 rpm [+/- 500]
Typical Rated Operating Current:	230 mA
Typical Normalised Amplitude:	148 G

Typical Vibration Motor Performance Characteristics

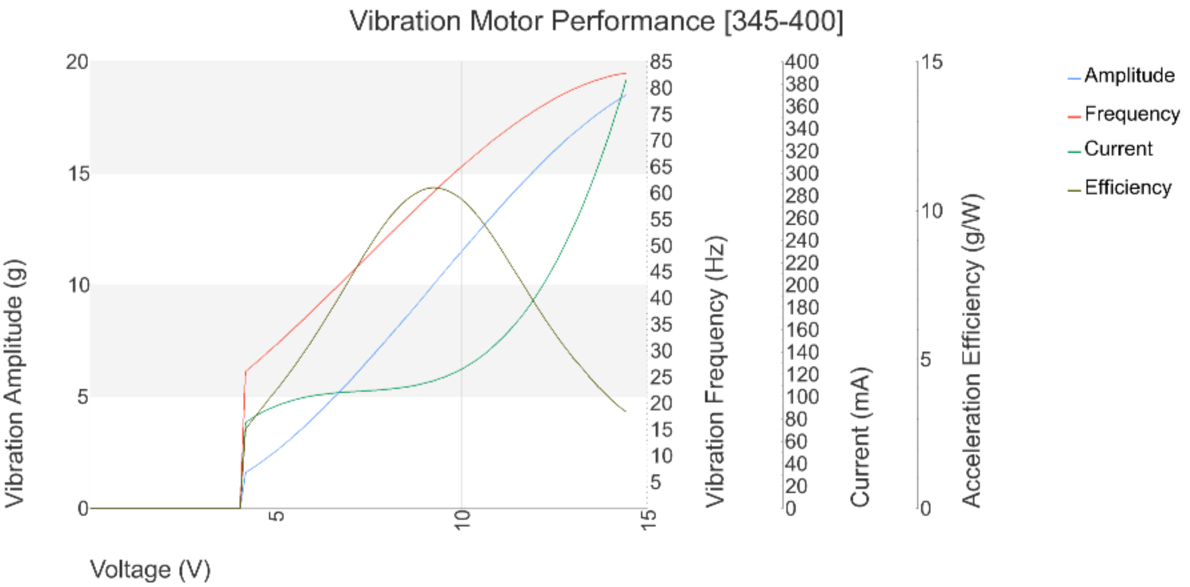

APPENDIX D

Freescale Semiconductor

MPX4250
Rev 7, 1/2009

Integrated Silicon Pressure Sensor On-Chip Signal Conditioned, Temperature Compensated and Calibrated

MPX4250 Series

0 to 250 kPa (0 to 36.3 psi)
0.2 to 4.9 V Output

The MPX4250 series piezoresistive transducer is a state-of-the-art monolithic silicon pressure sensor designed for a wide range of applications, particularly those employing a microcontroller or microprocessor with A/D inputs. This transducer combines advanced micromachining techniques, thin-film metallization, and bipolar processing to provide an accurate, high-level analog output signal that is proportional to the applied pressure. The small form factor and high reliability of on-chip integration make the Freescale sensor a logical and economical choice for the automotive system engineer.

Features

- Differential and Gauge Applications Available
- 1.4% Maximum Error Over 0° to 85°C
- Patented Silicon Shear Stress Strain Gauge
- Temperature Compensated Over –40° to +125°C
- Offers Reduction in Weight and Volume Compared to Existing Hybrid Modules
- Durable Epoxy Unibody Element

Application Examples

- Ideally Suited for Microprocessor or Microcontroller-Based Systems

ORDERING INFORMATION

Device Name	Package Options	Case No.	# of Ports			Pressure Type			Device Marking
			None	Single	Dual	Gauge	Differential	Absolute	
Unibody Package (MPX4250 Series)									
MPX4250D	Tray	867	•				•		MPX4250D
MPX4250GP	Tray	867B		•		•			MPX4250GP
MPX4250DP	Tray	867C			•		•		MPX4250DP

UNIBODY PACKAGES

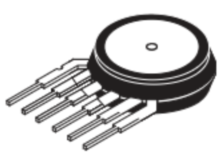

MPX4250D
CASE 867

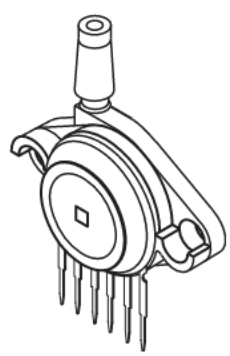

MPX4250GP
CASE 867B

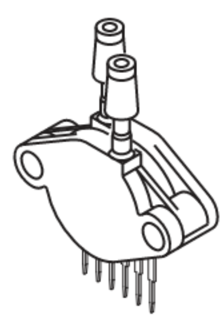

MPX4250DP
CASE 867C

Transfer Function (MPX4250)

Nominal Transfer Value: $V_{out} = V_S \times (0.00369 \times P + 0.04)$
$\pm$ (Pressure Error x Temp. Factor x $0.00369 \times V_S$)
$V_S = 5.1 \pm 0.25$ Vdc

Temperature Error Band

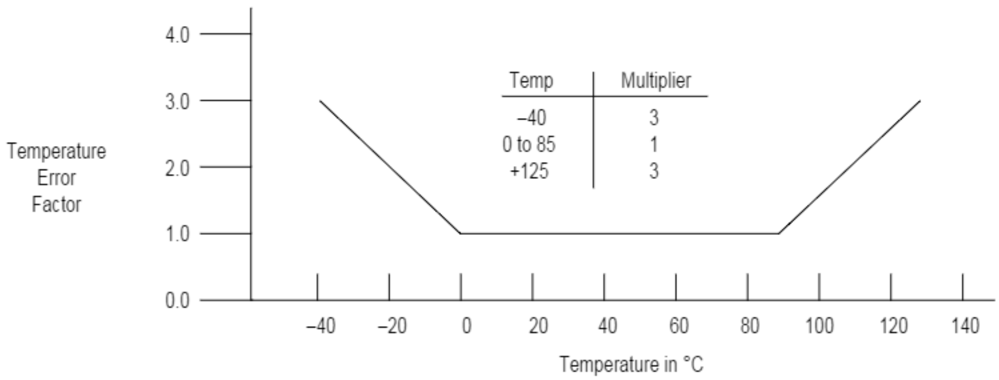

NOTE: The Temperature Multiplier is a linear response from 0°C to –40°C and from 85°C to 125°C.

Pressure Error Band

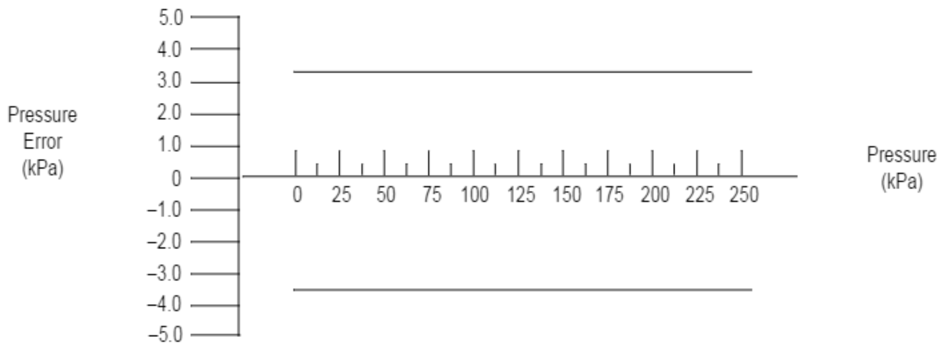

Pressure	Error (Max)
0 to 250 kPa	±3.45 kPa